

In Situ and Orbital Stratigraphic Characterization of the InSight Landing Site—A Type Example of a Regolith-Covered Lava Plain on Mars

N. H. Warner¹ , M. P. Golombek² , V. Ansan³, E. Marteau² , N. Williams² , J. A. Grant⁴ , E. Hauber⁵, C. Weitz⁶ , S. Wilson⁴, S. Piqueux² , N. Mueller⁵ , M. Grott⁵ , T. Spohn^{5,7} , L. Pan⁸ , C. Schmelzbach⁹ , I. J. Daubar¹⁰, J. Garvin¹¹ , C. Charalambous¹² , M. Baker⁴, and M. Banks¹¹ 

¹Department of Geological Sciences, SUNY Geneseo, Geneseo, NY, USA, ²Jet Propulsion Laboratory, California Institute of Technology, Pasadena, CA, USA, ³LPG, Nantes Université, Nantes, France, ⁴Center for Earth and Planetary Studies, Smithsonian National Air and Space Museum, Washington, DC, USA, ⁵German Aerospace Center (DLR), Institute of Planetary Research, Berlin, Germany, ⁶Planetary Science Institute, Tucson, AZ, USA, ⁷International Space Science Institute, Bern, Switzerland, ⁸Center for Star and Planet Formation, GLOBE Institute, University of Copenhagen, Copenhagen, Denmark, ⁹Institute of Geophysics, ETH Zurich, Zurich, Switzerland, ¹⁰Department of Earth, Environmental, and Planetary Sciences, Brown University, Providence, RI, USA, ¹¹NASA Goddard Space Flight Center, Greenbelt, MD, USA, ¹²Department of Electrical and Electronic Engineering, Imperial College London, London, UK

Key Points:

- InSight rests on Early Amazonian basaltic lava with an up to 10–30 m thick regolith. The upper 3 m of the regolith is sand dominated
- The regolith contains a 10–20 cm thick cohesive horizon or duricrust. This horizon rests 1–2 cm beneath the lander
- The upper 1–2 cm of the regolith comprises loosely-consolidated sand to pebbles. Sand is rarely mobilized under current wind conditions

Correspondence to:

N. H. Warner,
warner@geneseo.edu

Citation:

Warner, N. H., Golombek, M. P., Ansan, V., Marteau, E., Williams, N., Grant, J. A., et al. (2022). In situ and orbital stratigraphic characterization of the InSight landing site—A type example of a regolith-covered lava plain on Mars. *Journal of Geophysical Research: Planets*, 127, e2022JE007232. <https://doi.org/10.1029/2022JE007232>

Received 7 FEB 2022
Accepted 8 APR 2022

Author Contributions:

Conceptualization: N. H. Warner, M. P. Golombek, V. Ansan

Formal analysis: N. H. Warner, M. P. Golombek, V. Ansan, E. Marteau, N. Williams, J. A. Grant, E. Hauber, C. Weitz, S. Wilson, S. Piqueux, N. Mueller, M. Grott, T. Spohn, L. Pan, C. Schmelzbach, I. J. Daubar, J. Garvin, C. Charalambous, M. Baker, M. Banks

Investigation: N. H. Warner, M. P. Golombek, V. Ansan, E. Marteau, N. Williams, J. A. Grant, E. Hauber, C. Weitz, S. Wilson, S. Piqueux, N. Mueller, M. Grott, T. Spohn, L. Pan, C. Schmelzbach, I. J. Daubar, J. Garvin, C. Charalambous, M. Baker, M. Banks

Abstract The InSight lander rests on a regolith-covered, Hesperian to Early Amazonian lava plain in Elysium Planitia within a ~27-m-diameter, degraded impact crater called *Homestead hollow*. The km to cm-scale stratigraphy beneath the lander is relevant to the mission's geophysical investigations. Geologic mapping and crater statistics indicate that ~170 m of mostly Hesperian to Early Amazonian basaltic lavas are underlain by Noachian to Early Hesperian (~3.6 Ga) materials of possible sedimentary origin. Up to ~140 m of this volcanic resurfacing occurred in the Early Amazonian at 1.7 Ga, accounting for removal of craters ≤700 m in diameter. Seismic data however, suggest a clastic horizon that interrupts the volcanic sequence between depths of ~30 and ~75 m. Meter-scale stratigraphy beneath the lander is constrained by local and regional regolith thickness estimates that indicate up to 10–30 m of coarse-grained, brecciated regolith that fines upwards to a ~3 m thick loosely-consolidated, sand-dominated unit. The maximum depth of *Homestead hollow*, at ~3 m, indicates that the crater is entirely embedded in regolith. The hollow is filled by sand-size eolian sediments, with contributions from sand to cobble-size slope debris, and sand to cobble-size ejecta. Lander-based observations indicate that the fill at *Homestead hollow* contains a cohesive layer down to ~10–20 cm depth that is visible in lander rocket-excavated pits and the HP³ mole hole. The surface of the landing site is capped by a ~1 to 2 cm-thick loosely granular, sand-sized layer with a microns-thick surficial dust horizon.

Plain Language Summary The InSight lander has geophysical instruments that are designed to determine the interior structure of Mars. Understanding the results from these instruments requires a geological analysis of materials beneath the landing site at Elysium Planitia. This study presents data that describe the vertical sequence of rocks and soils beneath the lander, as well as the geologic history. The results indicate that InSight rests on a 1.7-billion-year-old lava plain that is covered in a 10–30 m thick regolith that was produced by impact cratering and modified by wind. The uppermost portion of the regolith is a ~3 m thick horizon of sand. InSight rests on sand within a degraded impact crater. The sandy material contains a slightly cohesive horizon that is only ~1–2 cm beneath the lander and is up to 10–20 cm thick. The sandy horizon overlies rock fragments that get progressively larger with depth. Bedrock of basaltic lava exists beneath the regolith down to a depth of ~170 m. The bedrock is interrupted by weaker materials between depths of ~30 and 75 m. Beneath ~170 m, the sequence is dominated by ancient (3.7–4.1 billion years old), possibly sedimentary materials.

1. Introduction

The Interior Exploration using Seismic Investigations, Geodesy and Heat Transport (InSight) mission to Mars landed on a Hesperian to Early Amazonian age, regolith-covered, basaltic lava plain in western Elysium Planitia on 26 November 2018 (Golombek, Warner, et al., 2020). The lander rests within a ~27-m-diameter, degraded impact crater informally dubbed *Homestead hollow*. The primary objective of this mission is to gain further

© 2022 The Authors.

This is an open access article under the terms of the [Creative Commons Attribution-NonCommercial License](https://creativecommons.org/licenses/by-nc/4.0/), which permits use, distribution and reproduction in any medium, provided the original work is properly cited and is not used for commercial purposes.

Methodology: N. H. Warner, M. P. Golombek, V. Ansan, E. Marteau, N. Williams

Resources: N. H. Warner, M. P. Golombek

Supervision: N. H. Warner, M. P. Golombek

Validation: N. H. Warner, M. P. Golombek, V. Ansan, E. Marteau, N. Williams, J. A. Grant, E. Hauber, C. Weitz, S. Wilson, S. Piqueux, N. Mueller, M. Grott, T. Spohn, L. Pan, C. Schmelzbach, I. J. Daubar, J. Garvin, C. Charalambous, M. Baker, M. Banks

Visualization: N. H. Warner, M. P. Golombek, V. Ansan, E. Marteau, N. Williams, J. A. Grant, E. Hauber, J. Garvin

Writing – original draft: N. H. Warner, M. P. Golombek, V. Ansan, E. Marteau, N. Williams

Writing – review & editing: N. H. Warner, M. P. Golombek, V. Ansan, E. Marteau, N. Williams, J. A. Grant, E. Hauber, C. Weitz, S. Wilson, S. Piqueux, N. Mueller, M. Grott, T. Spohn, L. Pan, C. Schmelzbach, I. J. Daubar, J. Garvin, C. Charalambous, M. Baker, M. Banks

understanding of the interior evolution of terrestrial planets by investigating seismic signals from a single station seismometer (the Seismic Experiment for Interior Structure or SEIS instrument) (Banerdt et al., 2020; Lognonné et al., 2020) and by radio tracking of the lander (Folkner et al., 2018). A secondary objective is to determine the interior thermal conditions of Mars via the Heat Flow and Physical Properties Package (HP³), a percussive mole that was designed to penetrate regolith to depths up to 5 m (Spohn et al., 2018). While the HP³ instrument failed to reach its 5 m objective, the mole is currently buried and functional, acquiring temperature readings and thermal conductivity estimates from the upper ~37 cm of regolith (Grott et al., 2021).

InSight is primarily a geophysical-themed mission. However, the local geology provides critical context for interpreting the results from the instruments. Understanding the local stratigraphy has implications for shallow seismic velocity measurements from SEIS (Kedar et al., 2017; Lognonné et al., 2020; Murdoch et al., 2021), models and observations of seismic signals from nearby crater impacts (Daubar et al., 2020), thermal conductivity and soil porosity estimates from HP³ (Grott et al., 2021), and thermal inertia and conductivity measurements from the onboard Radiometer (RAD) (Mueller et al., 2021; Piqueux et al., 2021). Multiple pre-landing and post-landing geological investigations characterized the landing site by providing geomorphologic observations of local landforms (Golombek et al., 2017, 2018; Golombek, Warner, et al., 2020; Grant et al., 2020; Sweeney et al., 2018; Warner, Golombek, et al., 2017; Warner, Grant, et al., 2020), stratigraphic and sedimentological characteristics of the regolith and lava plains (Grant et al., 2020, 2022; Pan et al., 2020; Warner, Golombek, et al., 2017; Weitz et al., 2020), measurements of the local and regional rock size distributions (Golombek et al., 2017, 2021), observations of active surface processes (e.g., eolian processes) (Baker et al., 2021; Charalambous et al., 2021), and comparisons to other landing sites (Golombek, Kass, et al., 2020; Warner, Schuyler, et al., 2020; Weitz et al., 2020).

Here, we investigate the local stratigraphy beneath the lander by first providing a brief review of all relevant pre-landing and post-landing observations published prior to Sol 1100 of the mission (Sections 2–3). We then describe new stratigraphic observations that utilize both orbital and lander-based data products (Sections 4–5). The goal is to provide a compendium of stratigraphic observations that will be useful for current and future geophysical investigations of InSight data. Our results also provide insights into the stratigraphy and evolution of lava plains and regolith development in general and is more broadly relevant to future landings and investigations of the geological history of Mars.

2. Review of Pre-Landing Orbital Constraints

2.1. Evidence of a Basaltic Lava Plain

InSight landed at 4.502°N, 135.623°E in western Elysium Planitia (Figure 1) (Golombek, Warner, et al., 2020; Golombek, Williams, et al., 2020). The terrain at the landing site was previously mapped by Tanaka et al. (2014) as part of the Early Hesperian Transition Unit (eHt) and is located due west of a large remnant of the Medusa Fossae Formation and Late Amazonian-age lava flows that are sourced from Elysium Mons to the north and Cerberus Fossae to the east. The unit is described as low relief, plains-forming material amidst scattered knobs and mesas of older protruding Noachian-age highlands. The Early Hesperian age was derived from the size-frequency distribution of kilometer-size craters. Like other northern plains units on Mars, Tanaka et al. (2014) interpreted a sedimentary or volcanic origin for eHt.

A broad region of eHt across western Elysium Planitia was scrutinized (Figure 1b) as part of InSight's landing site assessment (Golombek et al., 2017, 2018; Golombek, Kass, et al., 2020). Regional and local terrain mapping was conducted using Mars Reconnaissance Orbiter (MRO) Context Camera (CTX) images at ~6 m/pixel (Malin et al., 2007) and MRO High Resolution Imaging Science Experiment (HiRISE) images at ~25–30 cm/pixel (McEwen et al., 2007) in 20 candidate landing ellipses (Golombek et al., 2017). The terrain analysis identified a broad, smooth unit dubbed Smooth Terrain that covers the majority of the region, including most of the selected landing ellipse (Figure 1b). Smooth Terrain is noted for its moderately cratered surface, low abundance of ≥meter-size rocks covering 1%–2% cumulative fractional area (CFA), smooth inter-crater plains, moderate albedo, and a relatively low thermal inertia (160–230 J m⁻² K⁻¹ s^{-1/2}) that is consistent with loose, fine sand with a thermally thin (order of microns) dust coating (Golombek et al., 2017; Golombek, Warner, et al., 2020). Regions of higher thermal inertia across the Smooth Terrain correspond with fresh, rocky ejecta craters (RECs). RECs (up

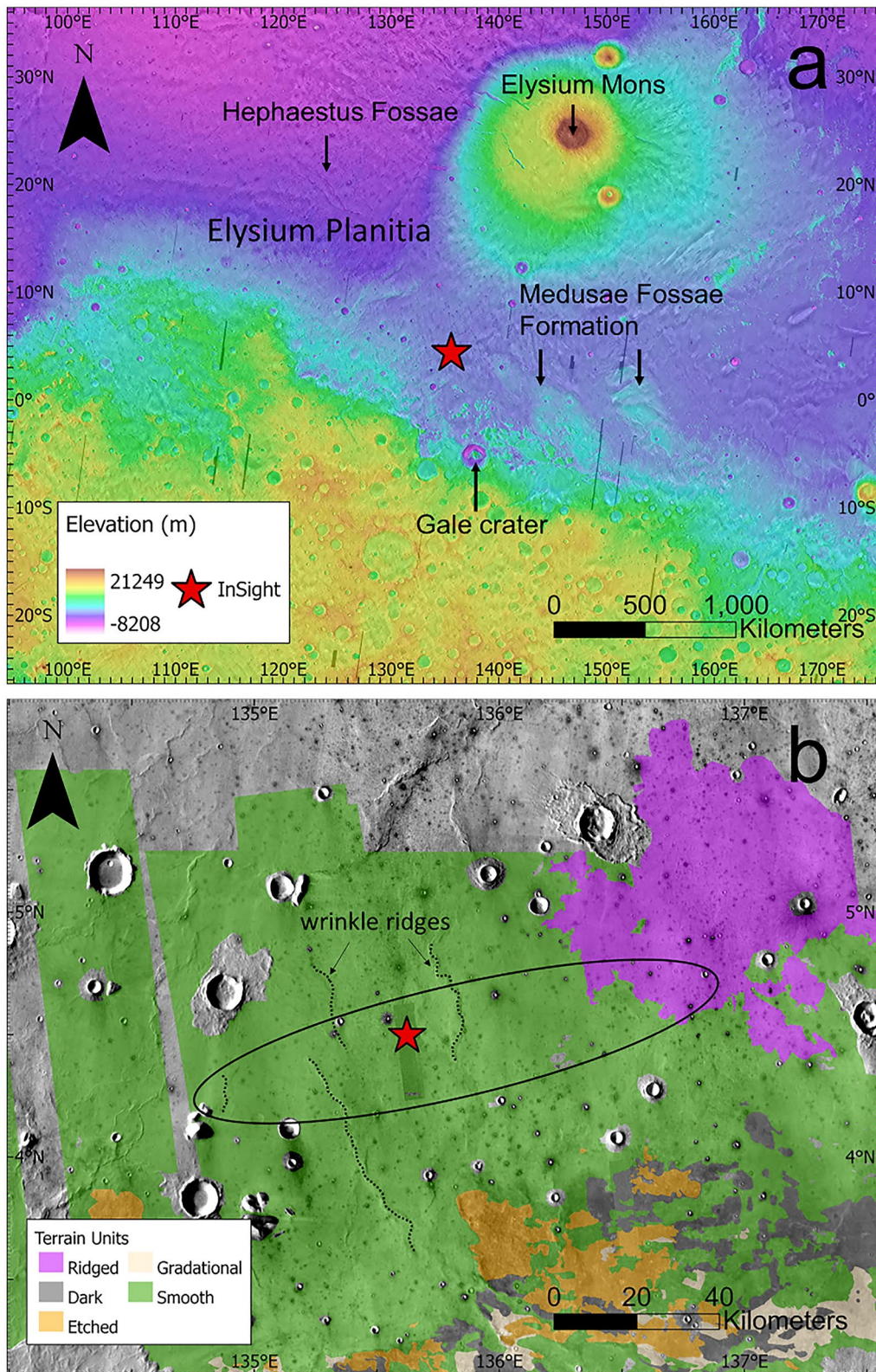


Figure 1.

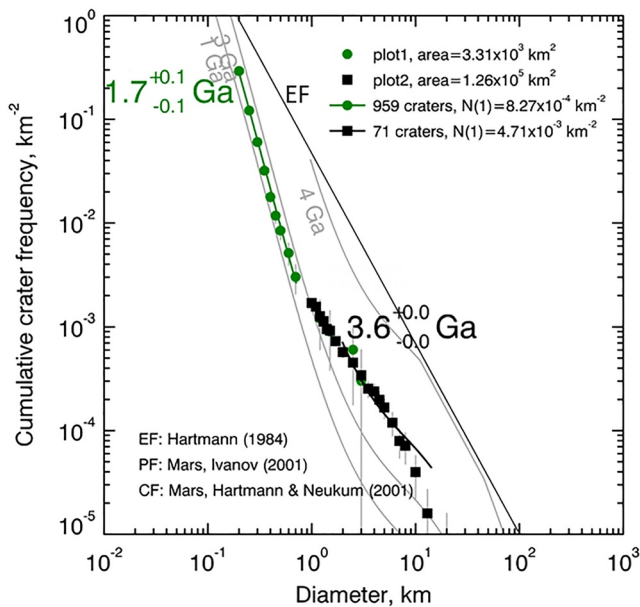


Figure 2. Cumulative size frequency distribution of impact craters on the Smooth Terrain (modified from Warner, Golombek, et al., 2017). The plot includes a smaller area ($\sim 3,310 \text{ km}^2$) count of craters with diameters $\geq 200 \text{ m}$ within and surrounding the final InSight landing ellipse (green circles) and a larger area count ($\sim 126,000 \text{ km}^2$) that includes craters with diameters $\geq 1 \text{ km}$. The data suggest that an Early Hesperian-age crater population (model age of 1.7 Ga) was partially resurfaced during the Early Amazonian (model age of 3.6 Ga). All craters with diameters $\leq 700 \text{ m}$ follow the Early Amazonian production function. Assuming a pristine depth to diameter ratio of 0.2, this suggests a maximum of 140 m of total resurfacing. The kink in the crater distribution from 2 km to 700 m likely reflects Early Hesperian to Early Amazonian crater resurfacing that preceded the 1.7 Ga event and is possibly related to Hesperian-age volcanism and/or landscape denudation by surface processes (e.g., fluvial activity). Crater production functions (PF, solid gray lines) from Ivanov (2001). Chronology functions (CF, derived model ages) from Hartmann and Neukum (2001). Crater equilibrium function (EF, darker solid black line) from Hartmann (1984).

to 35% CFA of rocks) only occur at diameters larger than $\sim 30\text{--}60 \text{ m}$ (average $\sim 40 \text{ m}$) but smaller than 2 km (Warner, Golombek, et al., 2017), and are interpreted to have excavated competent bedrock.

Regional geologic mapping, extending beyond the landing region, supported an effusive, basaltic origin for the Smooth Terrain (Golombek et al., 2018). The smooth plains in western Elysium Planitia are cross-cut by generally north-south trending wrinkle ridges. Wrinkle ridges have been interpreted as fault-propagation folds, in which slip on thrust faults at depth is accommodated by asymmetric folding in strong, but weakly bonded layered material (such as basalt flows or other competent rocks) near the surface (e.g., Golombek & Phillips, 2010; Mueller & Golombek, 2004). A particularly well-defined wrinkle ridge is located just $\sim 14\text{-km}$ east of the final landing site and is noted for its higher rock abundance and well-defined surface crenulations (Golombek et al., 2018) (Figure 1).

Mapping along the northeastern margin of the selected ellipse also revealed a lobate, Ridged Terrain that onlaps or inter-fingers the Smooth Terrain (Figure 1b) (Golombek et al., 2017, 2018). Ridged Terrain is noted for a series of semi-parallel, highly-degraded arcuate ridges that align with lobate unit margins. In some cases, the ridged texture transitions into a smooth surface on a single lobe, suggesting that the Smooth Terrain is a more degraded example of the Ridged Terrain. The albedo, thermal inertia, and presence of RECs is similar across both units. The lobate form, ridged surfaces (e.g., flow margins and pressure ridges), and possible vent structures, were interpreted to be the result of effusive-style basaltic volcanism sourced from the Elysium Mons volcanic region (Golombek et al., 2018; Pan et al., 2020).

Finally, impact crater statistics acquired across the Smooth Terrain revealed two distinct crater populations that supports crater resurfacing, likely by regional, effusive volcanism (Golombek et al., 2018; Warner, Golombek, et al., 2017) (Figure 2). At diameters $\geq 2 \text{ km}$, the cumulative crater size-frequency distribution follows an Early Hesperian isochron ($\sim 3.6 \text{ Ga}$) that is consistent with Tanaka et al. (2014) (Figure 2). However, an inflection in the crater distribution occurs over the diameter (D) range of $\sim 0.7\text{--}2 \text{ km}$ suggesting obliteration of craters after or during the Early Hesperian. At $D \leq 0.7 \text{ km}$, the distribution follows an Early Amazonian isochron with a model age of

$\sim 1.7 \text{ Ga}$ (Warner, Golombek, et al., 2017; Wilson et al., 2019) (Figure 2). The lack of evidence for broad-scale erosive processes in the surficial morphology of the Smooth Terrain (e.g., large pedestal craters, eroded remnants), as well as the basaltic volcanic morphologies described above, favor a volcanic resurfacing mechanism to explain this crater distribution. Assuming a pristine depth to diameter ratio of ~ 0.2 for km-size simple craters (Garvin et al., 2003; Pike, 1974), the data require complete resurfacing of the landscape by $\sim 140 \text{ m}$ in the Early Amazonian. However, it is likely that the pre-existing crater population was not pristine. Therefore, several tens of meters of Early Amazonian resurfacing may only be required if the Hesperian surface were eroded and km size craters were filled in prior to flooding by Amazonian basalts. Additionally, RECs, which suggest a competent bedrock unit beneath the lander, only occur up to a crater diameter of $\sim 2 \text{ km}$ on the Smooth Terrain (Golombek et al., 2017, 2018; Warner, Golombek, et al., 2017). Craters larger than $\sim 2 \text{ km}$ that exhibit an obvious continuous ejecta blanket (post-date volcanic resurfacing) lack boulder-size rocks in their ejecta in HiRISE images, suggesting weaker materials (possibly sedimentary) beneath the volcanic units (Golombek et al., 2017, 2018). Using

Figure 1. (a) Mars Orbiter Laser Altimeter color-shaded digital elevation model overlain on the 100 m/pixel Thermal Emission Imaging System (THEMIS) daytime infrared mosaic showing the geographic context of the InSight landing site in western Elysium Planitia (red star). (b) Terrain map modified from Golombek et al. (2017, 2018) showing the final landing location within the 130 km by 27 km landing ellipse. InSight landed within the Smooth Terrain unit, a regolith-covered lava plain noted for its low rock abundance, relief, and slopes. The Smooth Terrain is marked by multiple rocky ejecta craters (RECs) and cross-cut by wrinkle ridges. Adjacent terrain units include the rougher and rockier Etched Terrain to the south and a lobate, likely volcanic unit known as Ridged Terrain to the east and northeast.

the Melosh (1989) maximum depth of excavation relationship of 0.084 times the diameter of the final crater, an impact that formed a 2 km diameter crater excavated material into the continuous ejecta from a depth of ~170 m. The stratigraphic column beneath InSight therefore likely includes Early Amazonian lavas that are up to 140 m thick. But, these lavas are likely underlain by a few tens of meters of Hesperian lavas.

Independent results from an evaluation of the geomorphology and mineralogy of km-size craters in Elysium Planitia by Pan et al. (2020) further support volcanic resurfacing and the thickness estimates above. Multiple km-size ghost craters were identified on the Smooth Terrain outside of the final landing ellipse consistent with ~200 m of landscape resurfacing. Furthermore, deep excavation by large impacts revealed mineralogic evidence for mafic volcanics that overly hydrated, more-weakly lithified, clastic rocks (Pan et al., 2020). Fe/Mg phyllosilicates were identified in Compact Reconnaissance Imaging Spectrometer (CRISM) data, corresponding with lighter-toned, layered terrains in the central peaks of nearby large impact craters, including the 51-km-diameter Kalpin crater that is northeast of the landing site by ~430 km. Smaller impact structures, ranging from 1.5 to 7 km in diameter, revealed only mafic mineral signatures (e.g., pyroxene and olivine) in their rims, floors, and walls. From these observations, Pan et al. (2020) estimated a thickness of ~200–500 m for Hesperian to Amazonian effusive basaltic volcanics across the entirety of the western Elysium lava plain, including regions more proximal to Elysium Mons. The lower range of these thickness values is more consistent with the estimates from impact crater statistics within the landing ellipse (Warner, Golombek, et al., 2017).

2.2. Regolith Origins and Thickness

The orbital thermal data, the terrain morphology, and the age of the landing site were used before landing to infer the presence of an impacted-comminuted regolith that is dominated by loose, fine sand (Golombek et al., 2017). Furthermore, comparisons to other landing sites of similar terrain type and age such as the Gusev cratered plains where the Spirit rover landed (e.g., Golombek et al., 2006; Grant et al., 2006), indicated a plausible regolith thickness on the order of ~10 m. Additional orbital analyses were designed to estimate the regolith thickness of the final landing ellipse in preparation for HP³ operations (Golombek et al., 2018; Golombek, Kass, et al., 2020; Warner, Golombek, et al., 2017). Four independent lines of evidence were used to constrain regolith thickness including (Figure 3) (a) the presence of terrains (e.g., Etched Terrain) that suggest local eolian deflation of granular material from the Smooth Terrain, (b) the abundance and distribution of small, fresh, non-rocky ejecta impact craters (NRECs) that did not excavate deep enough to reach the more competent rocky unit beneath the Smooth Terrain, (c) observation of concentric/nested craters, and (d) an analysis of exposed stratigraphy at Hephaestus Fossae, a fracture ~900 km northwest of the InSight landing site that cuts through a potentially analogous (Golombek et al., 2017), Late Hesperian-age lava plain (Tanaka et al., 2014). A summary of each of these observations is presented below.

2.2.1. Etched Terrain

The Smooth Terrain in the selected landing ellipse grades to the south and southeast into a rougher surface with a higher thermal inertia called Etched Terrain (Figures 1b and 3a) (Golombek et al., 2017, 2018; Warner, Golombek, et al., 2017). The transition from Smooth to Etched can be gradational (e.g., Gradational and Dark Terrains) or abrupt, and is always associated with an order of magnitude increase in rock abundance and an increase in bedforms. In all cases, the Etched Terrain is revealed through local, topographically lower windows in the smooth surface. These observations led to the preliminary hypothesis that eolian processes were capable of deflating (or etching) a meters-thick granular, sandy regolith from the Smooth Terrain to expose rockier materials and generate the Etched Terrain (Warner, Golombek, et al., 2017).

2.2.2. Rocky Ejecta, Non-Rocky Ejecta, and Nested Craters

Warner, Golombek, et al., 2017, Golombek et al. (2018), and Golombek, Kass, et al. (2020) reported transitional diameters between fresh NRECs and fresh RECs on the Smooth Terrain (Figure 3b). All impact craters with diameters between 100 m and 2 km exhibit continuous rocky ejecta, with abundant meter-size rocks that are visible in HiRISE imagery. Rocks in the continuous ejecta of craters in this size range are excavated from depths between ~8 and ~170 m (Melosh, 1989). For craters with diameters between 40 and 100 m, meter-size rocks

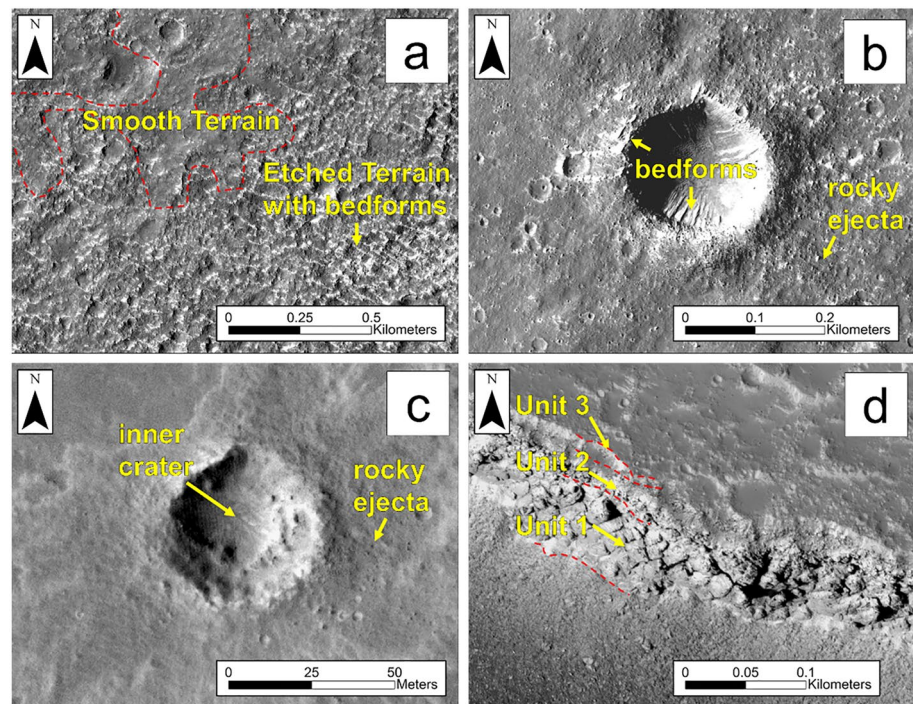


Figure 3. Montage of HiRISE images showing four example observations from the pre-landing analysis of the meter-scale stratigraphy on the Smooth and Etched Terrains. (a) HiRISE image ESP_035073_1840 showing a sample of the Etched Terrain that is immediately adjacent to Smooth Terrain. Etched Terrain is located south of the final landing ellipse (Figure 1) and has a higher rock and bedform abundance. Bedforms here are dust covered and have a higher albedo. This terrain unit was suggested to represent a wind-sculpted landscape (Golombek et al., 2017; Warner, Golombek, et al., 2017) and may reveal the shallow, meter-scale stratigraphic characteristics of the Smooth Terrain. (b) HiRISE image ESP_036761_1845 showing a ~200-m-size rocky ejecta crater (REC). RECs range in size from ~40 m to 2 km. Fresh craters between 30 and 60 m commonly lack rocks in their ejecta blanket, suggesting that the Smooth Terrain is capped by a meters-thick loosely-consolidated, granular regolith. (c) HiRISE image ESP_037196_1840 of a concentric or nested crater on the Smooth Terrain. Concentric craters were first identified in the landing ellipse by Warner, Golombek, et al. (2017) and suggest a strength transition at a depth of ~2–5 m below the surface of the Smooth Terrain. This example, at 40 m in diameter, excavated some rocks from a depth of ~2–3 m. (d) HiRISE image PSP_002359_2020 of an outcrop of rock along a steep scarp within Hephaestus Fossae. Hephaestus Fossae crosscuts a proposed analog lava plain to the Smooth Terrain (Golombek et al., 2017, 2018; Warner, Golombek, et al., 2017). The outcrop reveals fractured bedrock (Unit 1) overlain by a boulder-dominated unit (Unit 2) that is capped by a unit that lacks boulder-size rocks at HiRISE resolution (Unit 3). This sequence may represent an impact fractured lava plain that fines upwards to a loosely-consolidated, sand-dominated regolith.

either appear discontinuously in the continuous ejecta or are entirely absent. This suggests an overall “fining upwards” of the regolith column, grading from a rock-producing unit to a more granular unit that lacks meter-size rocks.

The 40–100 m crater diameter range also corresponds with the first appearance of concentric/nested craters (Warner, Golombek, et al., 2017) that indicate crater excavation into material with two distinct target strengths or weak over strong stratigraphy (Bart et al., 2011; Quaide & Oberbeck, 1968; Senft & Stewart, 2007) (Figure 3c). The smaller inner craters in the InSight landing region are noted for their rockier interiors and first appear at depths ranging from 2 to 6 m below the surrounding plains.

Craters with $D \leq 30$ –60 m (average of ~40 m) completely lack evidence for ejected rocks across the Smooth Terrain. The REC onset diameters and nested craters collectively suggest that a fines-dominated, granular regolith is everywhere \leq (order of) 10 m thick on the Smooth Terrain and is more commonly between 2 and 5 m thick. Below 2–5 m, the regolith likely transitions into coarser, fragmented basalt, possibly down to depths exceeding 10 m. Golombek, Kass, et al. (2020b) more specifically mapped all RECs and NRECs at the transitional diameters of 30–60 m across the selected landing ellipse. The map identified a range in the thickness of the upper,

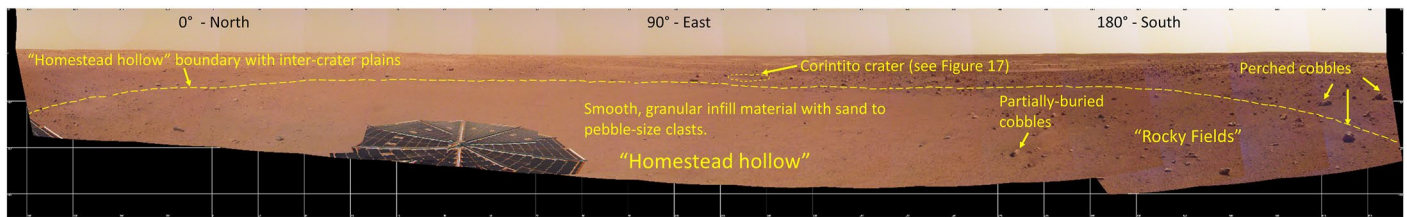


Figure 4. Instrument Deployment Camera (IDC) mosaic of the InSight landing site showing the lander's context within *Homestead hollow*, a highly degraded ~27 m diameter impact crater (Golombek, Warner, et al., 2020; Grant et al., 2020; Warner, Grant, et al., 2020). The hollow interior (looking south and east) is dominated by loosely-consolidated, sand to granule-size clasts with scattered pebbles and cobbles. Partially buried cobble-size clasts are evident within the hollow interior and reflect infilling of the crater, largely by windblown sand. Interior slope deposits also likely filled the crater but occur below the surficial materials. The *Corintito* impact crater, a secondary crater from the Corinto impact, is southeast of the lander and excavates into the granular surface regolith. The solar panel is 2.2 m in diameter for reference. *Corintito* is ~20 m from the lander.

fine-grained regolith of 2.5–5 m across the landing ellipse, with >2.6 m but <3.9 m as the most likely thickness proximal to the lander.

2.2.3. Hephaestus Fossae

The Hephaestus Fossae fracture system is located ~900 km northwest of the InSight landing site (Figure 1). It provides a unique, laterally continuous, and potentially analogous, stratigraphic exposure in HiRISE imagery of regolith over a reported Late Hesperian-age plains unit (Tanaka et al., 2014) (Figure 3d). The exposure yields three distinct stratigraphic “units” described in Warner, Golombek, et al. (2017), from bottom to top: (a) A thick fractured bedrock unit, (b) a coarse, boulder-rich, brecciated unit, and (c) a boulder-free, fines-dominated surface unit (Figure 3b). No HiRISE DEMs were available as of publication of the initial Hephaestus analysis to quantify the depths of the stratigraphic transitions in the exposure. The observation of a relatively finer-grained unit that coarsens with depth in Hephaestus Fossae is consistent with expectations from models of regolith production on Mars (Hartmann et al., 2001) and from impact fragmentation theory, which was also used to predict a sand-dominated surficial regolith at InSight (Charalambous, 2014, 2019; Golombek et al., 2018; Morgan et al., 2018). The downward coarsening seen in the exposure is expected from the power law decrease in the number of larger craters that excavate to greater depths. Using the constant cratering rate of the Hesperian and Amazonian, Hartmann et al. (2001) estimated that Early Amazonian to Hesperian age surfaces should have regolith thicknesses on the order of 1–10 m.

3. Review of Post-Landing In-Situ Constraints

The successful landing and operations of the InSight lander provided a unique opportunity to test the stratigraphic hypotheses presented above and to expand our understanding of stratigraphy and sedimentology of the regolith at the cm-scale. We present a review of published in-situ geological and geophysical constraints on the near-surface stratigraphy beneath the lander in this section before exploring new supporting observations from orbital and lander data in the following sections.

3.1. Surface Morphology and Sedimentology

The InSight lander touched down on the surface with a low tilt of 3.975° toward the SE (oriented 133.408° clockwise from the North) (Golombek, Williams, et al., 2020). Ground-based images were acquired from two color cameras (red, green, blue); the Instrument Deployment Camera (IDC) and the Instrument Context Camera (ICC) (Maki et al., 2018). The IDC's location on the Instrument Deployment Arm (IDA) (Trebi-Ollennu et al., 2018) allows for the construction of stereo panoramas of the surrounding landscape (Figure 4). The pixel scale of the IDC images used in this analysis ranges from 0.12 cm/pixel within the instrument deployment workspace up to a few cm at the southern edge of *Homestead hollow*, ~15–20 m south and east of the lander. The Instrument Context Camera (ICC) has a fisheye lens and is fixed to the lander body, pointing south in the direction of the instrument deployment workspace.

IDC and ICC images revealed a smooth surface in the instrument deployment workspace and immediately south and southeast of the lander, that is composed of loose, granule to pebble-size clasts (Wentworth, 1933 granulometry classification) within a cohesionless matrix of finer materials (Golombek, Warner, et al., 2020; Weitz et al., 2020) (Figure 4). Lander-radial streaks in the granular materials, ~10-cm-deep pits beneath the lander, imprints from hopping and rolling pebble-size rocks (e.g., *Rolling Stone* rock), and clasts with surficial dust coatings partially removed, suggest significant surface alteration and sediment transport by the lander's retrorockets (Golombek, Warner, et al., 2020). Large, cobble to boulder size rocks are rare on the surface. When present, they are angular and are more commonly partially buried by fines (Grant et al., 2020, 2022). Where dust coatings were removed, the clasts are medium gray with a presumed fine-grained texture (grains below the resolution limit of the IDC and ICC). Several of the rocks show faceted surfaces and are possibly ventifacts (Golombek, Warner, et al., 2020). The color, angularity, lack of vesicles, and grain size of the larger exposed clasts are most consistent with aphanitic basalts that experienced limited transport, likely by ejection from impacts. Pits beneath the lander expose buried clasts, a possible duricrust, and cm-scale stratigraphic architecture that will be described in detail in the following sections.

The smooth, granular surface grades sharply laterally into rockier terrain up to ~15–20 m from the lander in a south-southeast direction (Golombek, Warner, et al., 2020) (Figure 4). Here, multiple angular cobbles (and the occasional boulder) are distributed across a sand to gravel-dominated plain. A similar rocky terrain is present within only a few meters from the lander to the north and west. The overall rock abundance around the lander varies from <0.6% CFA within the smooth region to 3%–5% CFA in this rockier region (Golombek et al., 2021). A small scattering of larger pebbles extends from the west across the smooth surface. This scattering, known as *Rocky Field*, superposes the smooth material and shows limited evidence for post emplacement burial (Grant et al., 2020, 2022) (Figure 4).

The transition between the smooth region and the rockier materials marks the boundary of *Homestead hollow*, a ~27-m-diameter quasi-circular depression in the landscape (Warner, Grant, et al., 2020). The InSight lander rests entirely within the hollow, only a few meters from the northwestern margin (Golombek, Warner, et al., 2020). A morphometric analysis of similar hollows in the region indicated that *Homestead hollow* is a highly degraded impact crater with a maximum retention age on the landscape of ~400–700 Myr (Warner, Grant, et al., 2020). Crater degradational processes that are responsible for the present appearance of the hollow include infill by eolian sand, rim degradation from sand abrasion and ongoing impacts, and diffusional slope processes (e.g., hillslope creep) that reduced the height of the crater rim, decreased interior wall slopes, widened the crater by up to 20%, and partially filled the crater with slope debris (Grant et al., 2020; Sweeney et al., 2018; Warner, Grant, et al., 2020). Comparisons to fresh craters of similar small size to *Homestead hollow* suggest that it impacted into a fine-grained, unconsolidated regolith and did not excavate meter-size rocks. The interior walls of the hollow are therefore likely constructed of loose regolith consisting of sand to cobble-size clasts, similar to the overall sedimentology/clast distribution of the surrounding, regolith-covered rockier plains.

Sweeney et al. (2018) demonstrated that although slope modification played a major role in filling degraded craters here, infill by eolian-derived sandy materials accounts for up to ~40% of the total change in crater depth through time. Fresh impact craters in the region exhibit eolian bedforms in their continuous ejecta that are trapped against rocks and the exterior of the crater rim. There are few to no bedforms on the inter-crater plains. Within the ejecta, the sand is out of equilibrium with the surrounding landscape. Over time, the sand organizes against topographic obstacles (e.g., rocks and the rim) and eventually either migrates away or into the crater (Warner, Grant, et al., 2020; Grant et al., 2020, 2022). Similar to slope processes, eolian infilling is not a steady state process. The sand supply is limited in the ejecta, and as the crater rim and wall degrades and the cavity fills, it becomes less of a topographic sink. The morphometric data, combined with crater statistics, indicate that the bulk of the infilling at *Homestead hollow* occurred within the first ~50 Myr after crater formation (Warner, Grant, et al., 2020).

Assuming a pristine depth to diameter ratio of 0.15, determined from an analysis of hundreds of 10-m-scale craters (data set likely includes both primary and randomly-distributed secondary craters) across the InSight landing ellipse (Sweeney et al., 2018), the hollow's maximum initial depth was ~3 m (Warner, Grant, et al., 2020). The pristine rim was ~0.7 m high. Accounting for complete rim erosion, and given early crater filling, the maximum depth of loose fill within the center of *Homestead hollow* is between ~2 and 3 m. The thickness of the fill may vary beneath the InSight lander. The northern footpads rest only a few meters from the mapped northwestern crater rim (Golombek, Warner, et al., 2020) where the fill could be shallower than maximum estimates. The

instrument deployment workspace, where both the SEIS and HP³ instruments are located, is ~6 m by 4 m in size and extends south of the lander, closer to the crater interior.

3.2. Constraints From Thermal Data

The Radiometer instrument (RAD), part of the HP³ onboard InSight, acquires temperature data from the surface at two locations north-northwest of the lander from which thermophysical characteristics of the regolith are derived (Mueller et al., 2020). The near and far RAD spots are ~0.5 and ~3.5 m from the closest edge of the lander deck, respectively, and are fully within the mapped extent of *Homestead hollow* (Piqueux et al., 2021). While the near RAD spot is closer to the lander and instrument deployment workspace, complex shadows and the radiative and reflective properties of the lander deck may influence surface temperature readings and complicate the interpretation. For this reason, temperature data from the far RAD spot without lander shadow influence are preferred for soil analysis. The far RAD spot slopes toward the east-southeast by ~4° (at the length scale of the RAD footprint) and is located on the northwest edge of *Homestead hollow* (Golombek, Warner, et al., 2020; Golombek et al., 2021). Like all hollow-interior materials, the far RAD spot is dominated by a homogenized mixture of granules, pebbles, and a matrix of finer materials. Only ~2% of the surface in the far RAD (and 0% in the near) spot are covered by rocks >3 cm (Golombek et al., 2021), which contribute too little area and are too small to have any measurable effect on the derived thermal inertia (Golombek et al., 2003a; Piqueux et al., 2021).

Thermal inertia and thermometric albedo solutions for the far RAD spot were determined from a best fit to morning and night temperature observations up to Sol 50 (Piqueux et al., 2021), accounting for atmospheric opacity, soil porosity, and specific heat values for soils of basaltic composition (see Morgan et al., 2018). The analysis of the RAD diurnal temperature variations characterizes 1–2 diurnal skin depths within the soil, corresponding at this location to 4 and 8 cm from the surface (Piqueux et al., 2021). The solution for thermometric albedo of the far RAD spot, at 0.16, is slightly lower than orbital values derived from measurements from the Mars Global Surveyor Thermal Emission Spectrometer (TES) at 0.24 (Christensen et al., 2001; Putzig & Mellon, 2007), consistent with removal of an optically-thick layer of dust during landing (Golombek, Kass, et al., 2020). An average thermal inertia of $185 \pm 25 \text{ J m}^{-2} \text{ K}^{-1} \text{ s}^{-1/2}$ was determined and is also similar to orbital observations from the Thermal Emission Imaging System (THEMIS) onboard Mars Odyssey (Christensen et al., 2004) ($166 \text{ J m}^{-2} \text{ K}^{-1} \text{ s}^{-1/2}$) (Golombek et al., 2017; Golombek, Kass, et al., 2020). Thermal conductivity, derived from the apparent thermal inertia value, is $0.041 \pm 0.013 \text{ W m}^{-1} \text{ K}^{-1}$ when assuming a porous basaltic soil density of $1,300 \text{ kg m}^{-3}$ (Piqueux et al., 2021).

Similar estimates for soil thermal conductivity were acquired via RAD observations during Phobos transits across the sun (Mueller et al., 2021) and through near-surface active heating experiments performed by the HP³ mole's TEM-A sensors (Grott et al., 2021; Spohn et al., 2018). Thermal conductivity measurements from HP³, from depths $\leq 37 \text{ cm}$, indicate a low soil thermal conductivity of $0.039 \pm 0.001 \text{ W m}^{-1} \text{ K}^{-1}$ and a low soil density of $1,095 \text{ kg m}^{-3}$. These values suggest high porosity (~60%) in loosely-consolidated fine sand (125–160 μm) with very little, to no cement.

The results from the RAD and HP³ observations suggest that the upper several cm of soil beneath the lander is dominated by cohesionless fine sand with an optically-thin dust cover and no indication of mm to cm-scale layering (Piqueux et al., 2021). Yet, preliminary textural and morphologic observations of the retrorocket pits and HP³ mole hole provided evidence for mm to cm-scale variations in texture and argue for the possibility of a cohesive layer or duricrust in the shallow subsurface (Golombek, Warner, et al., 2020). These geologic/stratigraphic observations are central to the new results of this paper and will be discussed in the context of the thermal observations in Section 5.

3.3. Constraints From Shallow Seismic Data

Prior to landing it was recognized that information about the mechanical properties of the subsurface could be derived from three SEIS measurement sources (Golombek et al., 2018); (a) measurement of P- and S-wave velocities by SEIS from HP³ mole hammering (Kedar et al., 2017), (b) ground compliance from noise and wind vortices, and analysis of surface (Rayleigh) waves (Hobiger et al., 2021; Kenda et al., 2017; Knappmeyer-Endrun et al., 2017, 2018), and (c) resonances in the SEIS ground leveling system (Fayon et al., 2018). All these methods have yielded information about the mechanical properties of the subsurface that are consistent with the stratigraphy discussed herein.

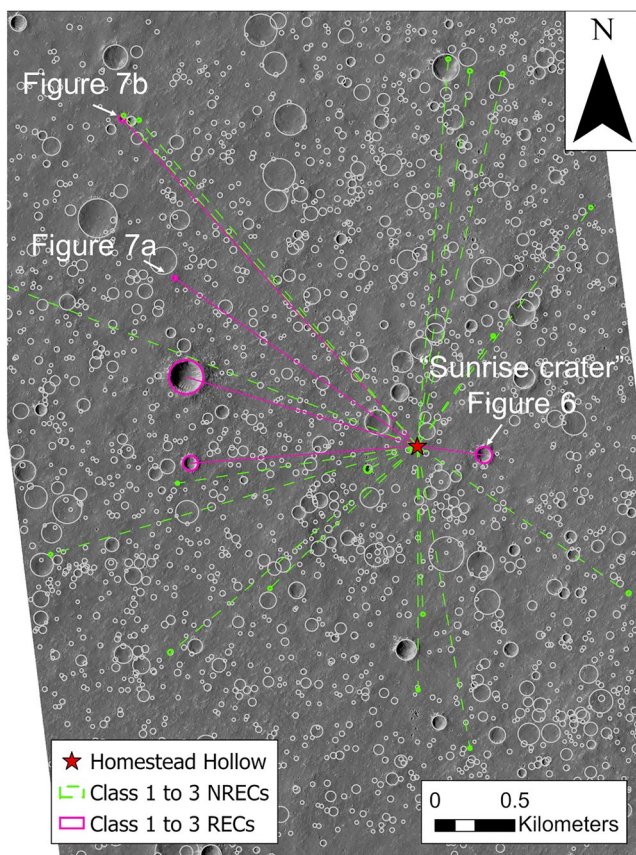


Figure 5. HiRISE image ESP_036761_1845 showing the location of *Homestead hollow* (red star) and the most proximal fresh (Class 1–3; Warner, Grant, et al., 2020) rocky and non-rocky ejecta craters (REC and NRECs). *Sunrise crater* (Figure 6), at 100-m-diameter, is the closest REC to the lander. The smallest RECs proximal to InSight are shown in Figures 7a and 7b.

At the 5 cm scale, the spikes below the SEIS feet appear to have penetrated beneath a ~ 1 cm-thick unconsolidated sandy layer, into a possible cohesive duricrust layer. At this depth, modeling of resonant frequencies of the SEIS leveling system indicates cohesive material that is 35% stiffer than unconsolidated material (Lognonné et al., 2020). At the 1 m scale, the P and S wave velocities of the material between the ~ 30 cm deep hammering mole and SEIS is ~ 114 and ~ 60 m/s (Brinkman et al., 2019; Lognonné et al., 2020), which corresponds to weak unconsolidated soils (Delage et al., 2017; Morgan et al., 2018). The P and S wave data indicated that if a cohesive layer exists, it is thin enough to not affect the bulk properties of the soil at the meter scale.

Ground deformation caused by convective wind vortices (and dust devils) distinguishes a meters-thick surface layer with very low seismic velocities that transitions with depth to material with higher seismic velocities (Kenda et al., 2020; Lognonné et al., 2020; Onodera, 2022). A formal inversion of the elastic properties of the subsurface down to ~ 20 m indicates a discontinuity at a 1–7 m depth between weak overlying surface material and much stronger material below. The Young's modulus increase is 10–100 times across the discontinuity, consistent with a transition of unconsolidated, sandy regolith above to layered basalts below. The most likely depth of transition of ~ 3 m is consistent with our best estimate of the depth of this transition described herein and in Golombek, Kass, et al. (2020).

Finally, inversion of high-frequency ambient noise Rayleigh wave ellipticity was used to probe to around 200 m beneath the surface. Hobiger et al. (2021) confirmed a significant increase in seismic velocity at a few meters depth beneath the lander, but also found a low velocity layer between 30 and 75 m depth. This ~ 45 m thick low velocity zone represents a weaker, Hesperian to Early Amazonian-age layer(s) that Hobiger et al. (2021) suggested may be sedimentary in origin.

4. New Observations From Orbital Data

Localization of InSight on HiRISE and CTX imagery (Golombek, Williams, et al., 2020) has enabled ongoing orbital analyses and refinement of the stratigraphic model. In this section we present new data regarding the meter-scale stratigraphic architecture beneath the lander from an analysis of: (a) the morphometry and excavation relationships of RECs that are proximal to the lander's location, (b) the thickness and erodibility of the Smooth Terrain unit, and (c) quantitative data from recently available HiRISE DEMs along the analog stratigraphic exposure at Hephaestus Fossae.

4.1. Excavation Relationships From Nearby RECs and NRECs

Previous results from a pre-landing orbital map of the onset diameter of rocky ejecta crater morphology in small (~ 30 – 60 m diameter) RECs across the InSight landing ellipse indicated that the relatively fine-grained regolith in the vicinity of the lander must be >2.6 m but <3.9 m thick (Golombek, Kass, et al., 2020). This estimate is generally consistent with the proposed initial depth of *Homestead hollow* (Golombek, Warner, et al., 2020; Warner, Grant, et al., 2020). Warner, Grant, et al. (2020) expanded this mapping effort to the exact location of the lander, including an inventory of smaller craters ($D \geq 20$ m) that range in morphology from pristine primary and secondary craters to highly degraded hollows. This inventory includes 2,260 craters within a ~ 21 km² area surrounding *Homestead hollow* (Figure 5).

Evaluation of this crater data set here confirms five youthful RECs that range in diameter from 28 to 215 m (Figure 5). Using the Sweeney et al. (2018) and Warner, Grant, et al. (2020) morphometric classification scheme

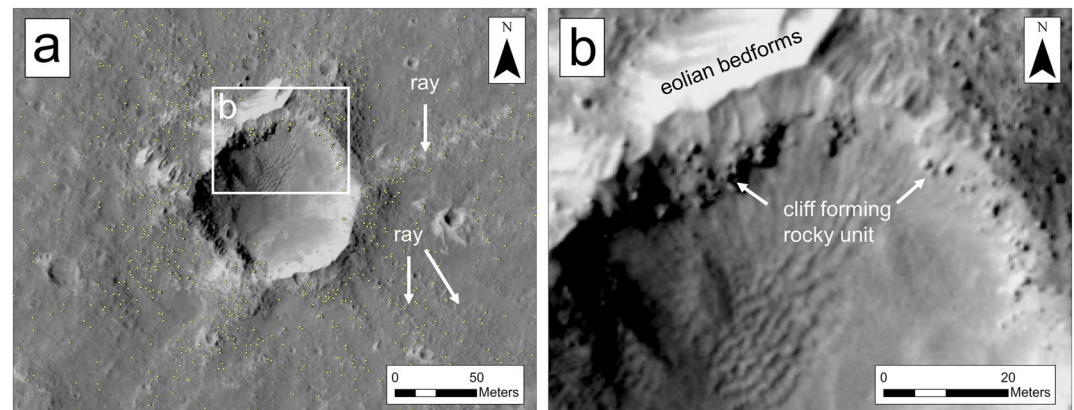


Figure 6. (a) HiRISE image ESP_036761_1845 of *Sunrise* crater, located ~ 420 m east-southeast of *Homestead hollow* (Figure 5). *Sunrise* contains obvious rays of boulder-size material (yellow dots). (b) The crater rim shown is superposed by boulder-size rocks on steep slopes and extend down to depths of ~ 2 – 3 m. The boulder-rich material is capped, in places, by relatively bright, dust-covered eolian bedforms. Using crater excavation relationships, the boulders in the crater rim and continuous ejecta were likely derived from a depth ranging between 6 and 9 m.

for the InSight landing region, the five fresh RECs fall within Class 1–3, which are the morphologically most fresh classes in the eight-class scheme. The nearest fresh REC to the lander is located 420 m to the east-southeast. This crater, informally known as *Sunrise crater* (Golombek, Warner, et al., 2020; Golombek, Kass, et al., 2020), is 100 m in diameter, has distinct rocky rays, and meter-size eolian bedforms trapped against the crater rim (Figure 6). For *Sunrise* crater, the rock abundance in the ejecta ranges from 0% to 17% CFA (Golombek, Kass, et al., 2020). Boulder-rich materials also superpose the rim of *Sunrise* and appear to transition into rays. The rim capping boulder unit is observed in HiRISE images and the available HiRISE DEM (1 m postings) of the landing site (Ferguson et al., 2017; Warner, Grant, et al., 2020) within the wall of the crater down to depths of 2–3 m, where it is covered by talus and windblown sediment (Figure 6b). No bedrock is observed inside *Sunrise* crater.

The boulder-rich rays in the continuous ejecta and rim-capping boulder-rich unit of *Sunrise* crater represent material excavated from a maximum depth that is ~ 0.084 times the final crater diameter (Melosh, 1989). Vertical gun experiments and observations of lunar and terrestrial craters also indicate a range of plausible excavation depths of 0.06–0.09 times the final crater diameter for variable impact angles and targets (Bart & Melosh, 2010; Grieve et al., 1981; Hermalyn & Schultz, 2011; Schultz & Anderson, 1996; Stoffler et al., 1975; Thompson et al., 1979). Given this range, the maximum depth of excavation of the rock producing unit beneath *Sunrise* crater is between 6 and 9 m, or ~ 8 m using the Melosh (1989) model. This provides a minimum constraint on the depth of rocky materials and maximum depth for the thickness of a capping, boulder-free regolith unit within the immediate vicinity of the lander.

The smallest REC within the ~ 21 km² study region is 28 m in diameter and is located 1.9 km northwest of the lander (Figures 5 and 7a). This unnamed crater is classified as an REC due to the higher rock abundance on the east side of the crater. The depth to excavation of these rocks, using the constraints above, is ~ 1.7 – 2.5 m. Most small, 10-m-scale craters in the InSight landing site lack observable rocks (Warner, Golombek, et al., 2017). For example, while there are five fresh, Class 1 to 3 RECs within the ~ 21 km² study region, there are 17 Class 1 to 3 NRECs in that same region. NRECs are generally smaller, ranging from 20 to 52 m in diameter, and have a rock abundance in the ejecta that is similar to the surrounding Smooth Terrain. Furthermore, even though small craters, like the 28-m-size example, can exhibit ejected rocks, the rock abundance is always lower when compared to 100-m-scale craters and the distribution is usually asymmetrical or discontinuous, forming small clusters or rays. The rock abundance pattern and low number of small RECs suggests either (a) a rock-producing layer is rarely shallow across the landing region or (b) that the upper regolith column sometimes includes clusters of boulder-size clasts in float. In the first case, 10-m-scale fresh craters can sometimes, but not always, exhibit a concentric or nested morphology that is associated with rocky ejecta (Warner, Golombek, et al., 2017). The second smallest REC in the study area is 43 m in diameter, and at a distance of 2.8 km, is the closest possible nested crater to the lander (Figures 5 and 7b). From the HiRISE DEM, the inner crater here is ~ 17 m in diameter and ~ 1.5 m deep. The rim of the inner crater occurs ~ 1.5 m below the elevation of the surrounding plains. Small

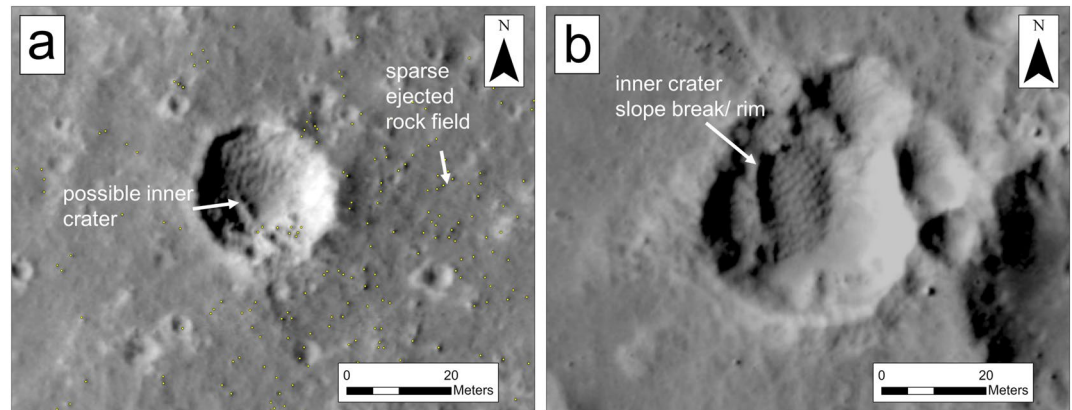


Figure 7. Example small RECs near the InSight lander (HiRISE image ESP_036761_1845) (see Figure 5). At diameters of 28 m (a) and 43 m (b), these craters show evidence for relatively shallow ($\sim 2\text{--}3$ m) excavation of boulder-size rocks. Figure 7a illustrates a relatively higher abundance of rocks east of the crater (yellow dots) that likely represent ejected boulders. Both craters show possible evidence for a smaller inner crater, produced by a stronger, blocky layer at depth. Most fresh craters of this size proximal to InSight lack rocks in their ejecta, suggesting that the boulder-free, loosely-consolidated regolith is almost everywhere ≥ 3 m thick.

rays of boulder-size rocks extend from the northwestern and northeastern edge of the crater rim are therefore sourced from a relatively shallow depth of $\sim 1.5\text{--}3$ m.

Despite the observation of small RECs, the overwhelmingly larger number of small, fresh NRECs in the study region (Figure 5) implies that small impacts into the upper stratigraphic column do not typically produce meter-size rocks. The closest NREC to InSight is the largest in the area (Figure 5). This 52 m diameter crater excavates material into its continuous ejecta from depths of 3.1–4.7 m (Bart & Melosh, 2010; Grieve et al., 1981; Hermalyn & Schultz, 2011; Schultz & Anderson, 1996; Stoffler et al., 1975; Thompson et al., 1979). Using the two most proximal RECs and NRECs to the lander, the granular, fines-dominated regolith is at least ~ 3 m thick and the upper stratigraphic contact of the boulder producing unit occurs at a depth between ~ 3 and 8 m, both of which are consistent with previous contoured maps of minimum and maximum regolith thicknesses across the broader landing ellipse (Golombek, Kass, et al., 2020).

4.2. Modification and Morphometry of the Smooth and Etched Terrains

InSight's final landing location rests entirely within the Smooth Terrain geomorphic unit (Golombek, Warner, et al., 2020). The nearest terrain boundary is ~ 40 km south of the landing site where the smooth planar surface transitions into the rougher Etched Terrain (Figure 1b). The eolian deflation hypothesis for the Etched Terrain (Warner, Golombek, et al., 2017) has implications for the sedimentology, thickness, and origin of the Smooth Terrain, and therefore the regolith beneath the lander. Here, we test the eolian-stripping hypothesis by quantifying the surficial morphometry of the Smooth and Etched units using HiRISE DEMs. Impact crater statistics are also used to track relative differences in crater retention.

HiRISE DEMs were used to quantify the relative surface roughness, relief, and slope characteristics of the Smooth and Etched Terrains. The DEMs over both the Smooth Terrain and Etched Terrain samples were produced during InSight's landing site selection process and have 1 m postings and a vertical precision of $\sim 0.1\text{--}0.2$ m (Ferguson et al., 2017). The morphometric characteristics were determined for the Smooth Terrain previously at InSight's landing location by Warner, Grant, et al. (2020), corresponding to HiRISE image ESP_036761_1845 and its associated stereopair and DEM. We use the same methods here to analyze a new sample of Etched Terrain and compare the results to the Warner, Grant, et al. (2020) data set.

The Etched terrain sample analyzed here is ~ 60 km southeast of the landing site and is covered by HiRISE image ESP_035073_1840 and associated DEM (Figure 8). At this location, the Etched Terrain rests within a ~ 23 km² “window” in the Smooth Terrain that is defined by a relatively sharp contact to the north and a more gradational contact to the west and south. Surface roughness was calculated in ArcGIS Pro as the standard deviation of elevation in a 3 pixel by 3 pixel moving window. Slope was similarly calculated as the change in elevation with

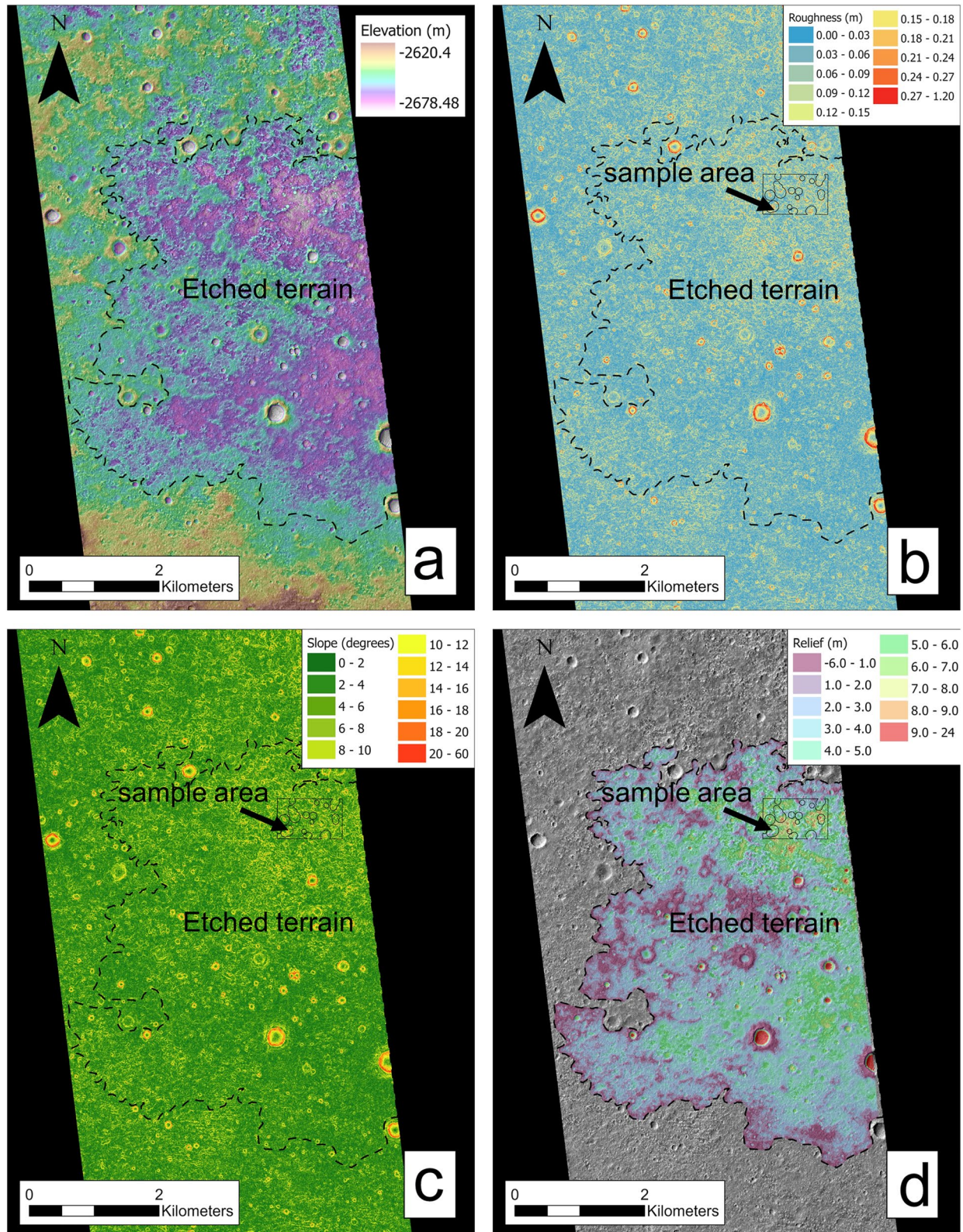


Figure 8.

distance from a 3 pixel by 3 pixel window (in degrees). The relief between the Smooth and Etched units in ESP_035073_1840 was determined first by digitizing the contact between the two units. The contact was mapped along the upper, elevated surface of the Smooth Terrain and was converted to 3D points that record elevation at each point. A Natural Neighbor interpolation was applied to fit a rasterized surface across the Etched exposure, mimicking the regional elevation of Smooth Terrain. The DEM was subtracted from the interpolated raster to reveal the relief between the two units.

The average surface roughness for the Smooth and Etched terrain units are ~ 0.03 m (one standard deviation (σ) = 0.02) (Warner, Grant, et al., 2020) and 0.06 m (σ = 0.04), respectively (Figure 8b). For slope, the averages are $\sim 2.0^\circ$ (σ = 1.0°) for the Smooth Terrain (Warner, Grant, et al., 2020) and 4.1° (σ = 2.9°) for the Etched Terrain (Figure 8c). The slope and roughness differences are consistent with HiRISE observations of higher abundances of both meter-size bedforms and rocks on the Etched surface. The highest abundance of rocks and bedforms occurs in the northern region of the Etched Terrain. Here, average surface roughness and slopes are higher than the bulk average at 0.08 m (σ = 0.05) and 5.2° (σ = 3.3°). This area also corresponds with the highest maximum and average relief between the Smooth and Etched surfaces (excluding impact craters) at ~ 9 m (Figure 8d). The average relief between Smooth and Etched Terrain is 2.9 m (σ = 1.9 m).

The elevation differences between the two surfaces and the correspondingly higher abundance of bedforms indicate that topographically lower windows of Etched Terrain trap windblown sand (Figure 9). The topographically lowest region of the Etched Terrain in the north for example, correlates with the highest abundance of ripples (Figures 9a and 9b). The lack of bedforms on the Smooth Terrain suggest a lower sand supply, a lower wind activity, or a surface rich in sand that is in aerodynamic equilibrium. Furthermore, the low roughness might preclude sediment trapping, outside of the occasional rock or impact crater. While the bedforms explain some of the roughness differences between the Smooth and Etched surfaces, the HiRISE images also reveal elevated ridges, buttes, or mesas in the Etched Terrain that exhibit a relatively high rock abundance (Figures 9a and 9b). These remnants also trap sand. Topographic profiles across the elevated features indicate that they are typically one to 5 m in height and are most prominent in the northern, deepest section of the window. They have no preferred orientation but can be arcuate where they surround impact craters, forming pedestal-like impact structures. Golombek et al. (2017) previously noted an elevated rock abundance throughout the Etched Terrain that in places exceeds 20% CFA. Upon closer inspection here, the highest rock abundance corresponds with the topographically-lowest margins of the elevated topographic features. Few rocks are observed on the summits or uppermost flanks of the remnants.

The topographic differences between the Etched and Smooth Terrain samples, including the presence of elevated remnants and pedestal craters, are consistent with an erosional origin for the Etched Terrain, most likely by a wind environment that at one point was capable of stripping fines from the surrounding Smooth Terrain. Furthermore, impact crater statistics reveal important differences between the two surfaces in the size-frequency distribution of small, 10-m-scale impact structures that confirm erosion of surficial materials. Figure 10 presents a crater count from the ~ 23 km² size window of Etched Terrain. All impact craters larger than 20 m are included. A density map of the craters in the Etched sample indicates a relatively lower crater density in the northern region, corresponding to the topographically lowest and roughest segment of Etched Terrain. This implies, along with the presence of pedestal impact structures, that small craters have been preferentially eroded from the deepest region of the Etched Terrain. A comparison to the cumulative size frequency distribution of craters on the Smooth Terrain in a ~ 21 km² region surrounding InSight from Warner, Grant, et al. (2020) also supports the erosion hypothesis. The cumulative frequency of craters is lower at all diameter bins ≤ 100 m on the Etched Terrain, consistent with up to 15 m of erosion, assuming all craters were at their pristine depth that is 0.15 times the diameter (Sweeney et al., 2018). However, through a comparison to the Smooth Terrain surface, the bulk of the missing craters from the Etched Terrain correspond to highly degraded craters and hollows that were, at most, only a few meters deep. Warner,

Figure 8. (a) 1 m HiRISE DEM overlain on orthophoto ESP_035073_1840. The DEM reveals the topographic characteristics of the Etched Terrain. (b, c) Surface roughness and slope maps, respectively, of the Etched Terrain and surrounding Smooth Terrain. The Etched Terrain is notably rougher, exhibiting a higher abundance of meter-size rocks, bedforms, pedestal craters, and remnant ridges and buttes that form slopes at or near the angle of repose of loosely-consolidated materials. (d) Relief map of the Etched Terrain. The maximum relief between the Etched and Smooth terrains, excluding deep impact craters, is ~ 9 m. The deepest and roughest portion of the Etched Terrain occurs within the small sample area in the north of the outlined region. The gradational to sharp contact between the Smooth and Etched surfaces, coupled with the observations of remnant ridges, boulder-size rocks, and abundant bedforms, suggests that the Etched Terrain is a wind-sculpted surface that was produced by the preferential removal of fines within the upper, sand-dominated regolith that typically caps the Smooth Terrain. The maximum depth of the Etched Terrain therefore provides a constraint on the thickness of the mobile regolith.

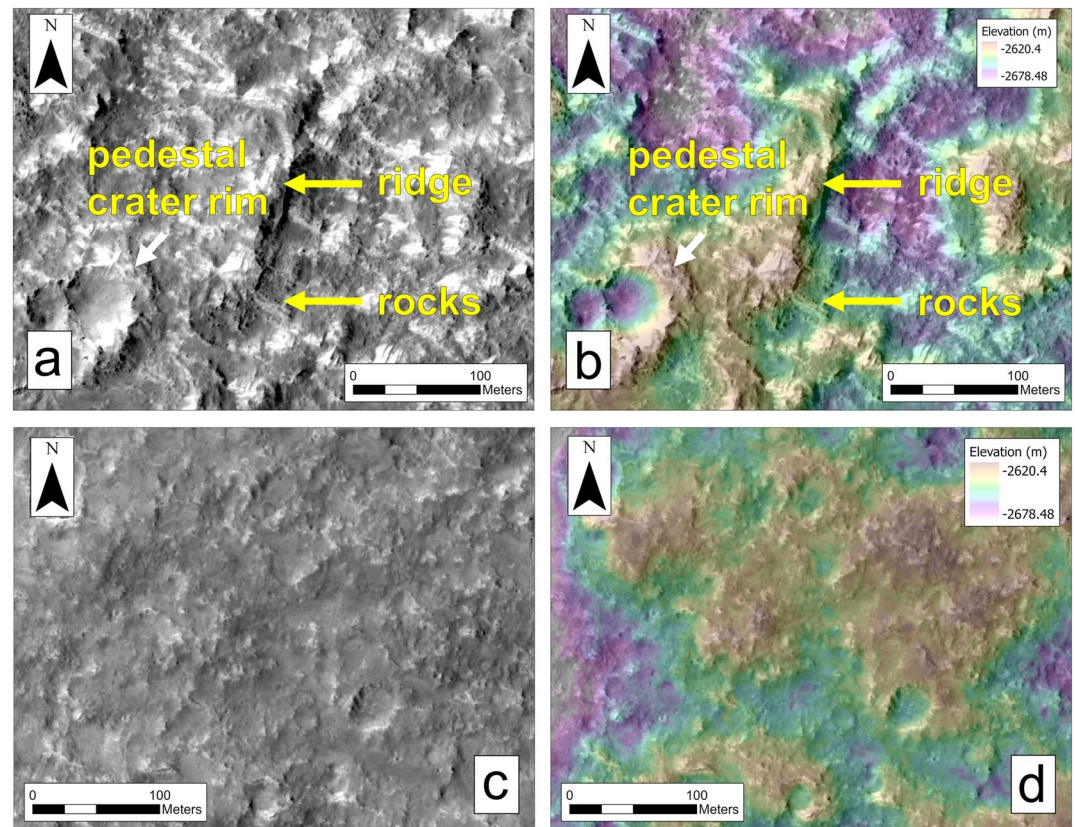


Figure 9. HiRISE image ESP_035073_1840 and associated 1 m DEM comparing the surface morphology of the Etched Terrain relative to the Smooth Terrain (at the same scale). (a, b) Etched Terrain is noted for a higher rock abundance, relatively bright bedforms, remnant ridges, buttes, and pedestal craters. Boulder-size rocks occur along the lower flanks of the ridges, pedestals, and buttes. Ridges and buttes have relief of 2–5 m, but in places approach a height of ~10 m above the surrounding lower terrain. (c, d) In contrast, the nearby Smooth Terrain has longer wavelength relief and lacks rocks, bedforms, or elevated landforms.

Grant, et al. (2020) identified thousands of hollows and highly-degraded crater structures on the Smooth Terrain at the InSight landing site, including *Homestead hollow*. Hollows are difficult to detect in HiRISE images, but are most obvious on smooth, flat lava plains like the Smooth Terrain at InSight and the Gusev cratered plains where they were best observed by the Spirit rover (Golombek et al., 2006; Weitz et al., 2020). Similar hollows are missing from the Etched surface, implying near-complete erosion of the craters, likely by wind.

The relatively higher rock abundance on the Etched Terrain suggests that the erosional process exposed coarser materials. The coarser clasts concentrate along the flanks and near the base of the remnant ridges, mesas, and buttes. This may indicate (a) that boulder-size rocks are concentrated by weathering out of the entire stratigraphic column, forming talus at the base of slopes or (b) that boulder-size clasts become more concentrated in the stratigraphy of the regolith with depth. In the latter case, the exposure of boulders may provide a constraint on the depth to rockier materials beneath the Smooth Terrain. From the terrain samples in Figure 9, rocks begin to appear ~2–3 m below the summit of the remnants, which is consistent with the constraint on the minimum depth of excavation in the REC analysis.

4.3. Stratigraphic Architecture at Hephaestus Fossae, Analog for the InSight Landing Site

The REC and Etched Terrain analyses, although consistent with each other, are indirect methods for characterizing the meter-scale stratigraphy beneath the lander. Unfortunately, there are no exposures in the Smooth Terrain that reveal the full three-dimensional, stratigraphic architecture. The unique exposure at Hephaestus Fossae (Golombek et al., 2017; Warner, Golombek, et al., 2017) provides a window into a potentially analogous surface.

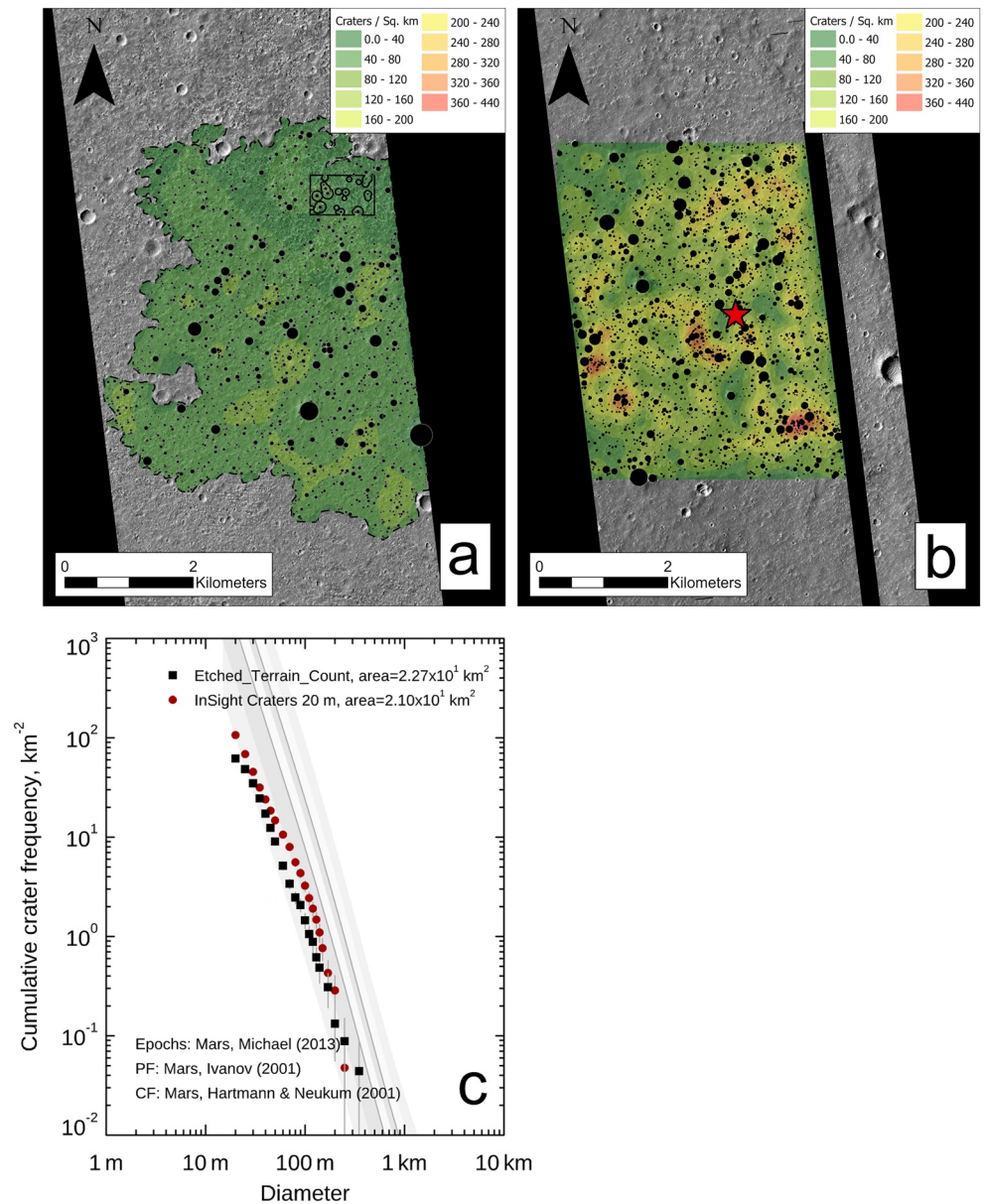


Figure 10. (a, b) Impact crater density maps comparing the size frequency distribution of all impact craters with diameters ≥ 20 m on (a) the Etched Terrain in HiRISE image ESP_035073_1840 (also see Figure 8) and (b) the Smooth Terrain at the InSight landing site (red star marks the lander location) in HiRISE image ESP_036761_1845. The map was produced using the Kernel Density function in ArcGIS Pro. The Smooth Terrain is notable for the abundance of 10 to 100-m-scale, degraded, quasi-circular impact structures known as hollows (Warner, Grant, et al., 2020; Weitz et al., 2020). Similar hollows are lacking on the Etched Terrain, suggesting higher rates of landscape erosion and stripping of shallow hollow landforms from the regolith. (c) Cumulative size-frequency distribution of all craters with $D \geq 20$ m in the 21–23 km² square sample regions on the Etched Terrain (a) and at InSight (b). The cumulative frequency of craters converges to similar values at $D > 100$ m. Below this diameter, there is a factor of 2–3 higher crater frequency on the Smooth Terrain compared to the Etched Terrain. This is consistent with the preferential removal of < 100 m size craters to form the Etched morphology. Craters of this size had initial pristine depths of up to 20 m. Crater production functions (PF, solid gray lines) from Ivanov (2001). Chronology functions (CF, derived model ages) from Hartmann and Neukum (2001). Martian epoch boundaries (Late Amazonian to Mid Noachian gray fill between production lines) from Michael (2013).

Here, we provide new stratigraphic data for the Hephaestus Fossae exposure using newly available 1 m HiRISE DEMs that include this fracture system. We also utilize impact crater statistics to constrain the age of the smooth, cratered plains that surround the fracture system and compare that age to the Smooth Terrain at InSight. The

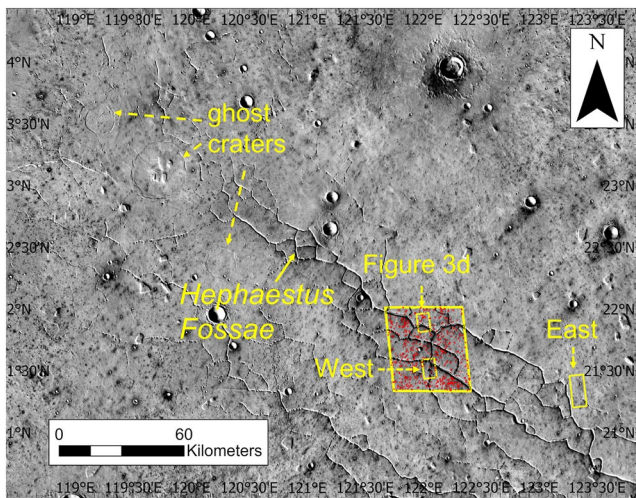


Figure 11. Context map of Hephaestus Fossae fracture system in the 100 m/pixel Thermal Emission Imaging System Daytime IR mosaic (THEMIS). Footprints of the HiRISE DEMs for Locality West and East are shown. The outline of the crater count area is also shown. Craters are in red. The Hephaestus Fossae fracture system exposes tens of meters of volcanic plains. Multiple large ghost craters in the region suggest regional resurfacing, likely by Early Amazonian volcanic materials.

age of the surface has implications for regolith production rates and thickness. Figure 11 identifies two locations along the fracture system that correspond with two available HiRISE DEMs. The associated HiRISE images are ESP_052638_2020 and PSP_001462_2015, which will be referred to here as Locality West and East, respectively. The orthorectified images, at 25 cm/pixel, were used to map stratigraphic boundaries in the south-facing wall of each exposure.

Locality West straddles a ~1-km-wide, ~400-m-deep segment of a single fracture in the Hephaestus system. Approximately ~250 m of the lower vertical exposure is talus comprised of boulder-size rocks that have weathered from the higher outcrop. The upper ~150 m exposes the stratigraphy beneath the overlying smooth, cratered plains. Three distinct units are visible in the outcrop and include from bottom to top: (a) the fractured, cliff-forming unit, (b) the boulder-dominated, cliff forming unit, and (c) the fines-dominated slope-forming unit (Figures 12a and 12b). In this instance, the phrase “fines-dominated” refers to the lack of visible rocks at the resolution of the HiRISE image. The stratigraphic boundary between each unit is gradational but can be defined not only by changes to the sedimentology/structures in the outcrop but changes in slope. Each contact was mapped as a polyline in ArcGIS Pro. The line was then converted to points and the points were used to query elevation values. Figure 12 displays the mapped contacts and slope map along the outcrop at Locality West. Contacts were mapped along the 1.5-km-long extent of the south-facing exposure. The units are generally horizontal. However, variability exists in the mapped elevations of each

contact. For example, the standard deviation in measured elevation along the length of the measurement is 32 m for the contact between the boulder-dominated unit and the fractured unit, 6.0 m between the fines-dominated and boulder-dominated units, and 3.8 m at the slope break with the plains. While this variability may be real, significant uncertainty exists, especially considering the more gradational nature of the contacts. Subtracting the average elevation values for each contact yields a thickness of ~126 m for the fractured unit (measured down to the top of the talus), ~21 m for the boulder-dominated unit, and ~7 m for the upper fines-dominated unit. Individual topographic profiles were also drawn where the orientation of the exposure relative to the camera allows for best viewing (east-west striking exposures). The two profiles taken along Locality West reveal thickness values of 112–133 m for the fractured unit (down to talus), 13–29 m for the boulder-dominated unit, and 4.2–5.0 m for the fines-dominated unit (Figure 13a). Average slope values range from 59° to 66°, 45°–46°, and 19°–20° for the fractured, boulder, and fines-dominated units, respectively. The slope values are consistent with the stratigraphic observations suggesting that both the fractured and boulder-dominated units hold steep slopes that exceed the stable angle of repose for unconsolidated materials (~30°–40°).

The steepness, thickness, and structure of the lower fractured unit are most consistent with resistant bedrock. The fractures may represent cooling fractures in a basaltic lava flow, and in places, bear a striking similarity to hexagonal columns (Golombek et al., 2017; Warner, Golombek, et al., 2017). The overlying boulder-dominated unit also supports steeper slopes, but may either represent the primary, flow-fractured blocky surface of a lava flow or a surface fractured and brecciated by impacts. In the latter case, the blocky unit may be the coarser portion of a regolith column that grades upwards into the fines-dominated unit and downwards into the bedrock. The slope of the fines-dominated unit is notably lower than the angle of repose and is consistent with unconsolidated, fine granular material. However, some of the queried pixels in the 3 pixel by 3 pixel slope calculation window include the surrounding plains, which have a near-zero slope. This could produce lower average slopes than those present.

Figures 12c and 12d, and Figure 13b presents supporting data for Locality East. This exposure is 70-km from Locality West and shows similar stratigraphic characteristics down to the contact between a fines-dominated and boulder-dominated unit. A thick, fractured unit is not visible here. The deepest segment of the fracture is only ~80-m-deep and talus covers a significant portion of the exposure. Contacts were mapped between the units along a 1.1 km stretch of the exposure. The standard deviation of elevation for the contact between the fines and boulder-rich unit is 3.3 m. For the elevation of the plains at the top of the exposure, the standard deviation is

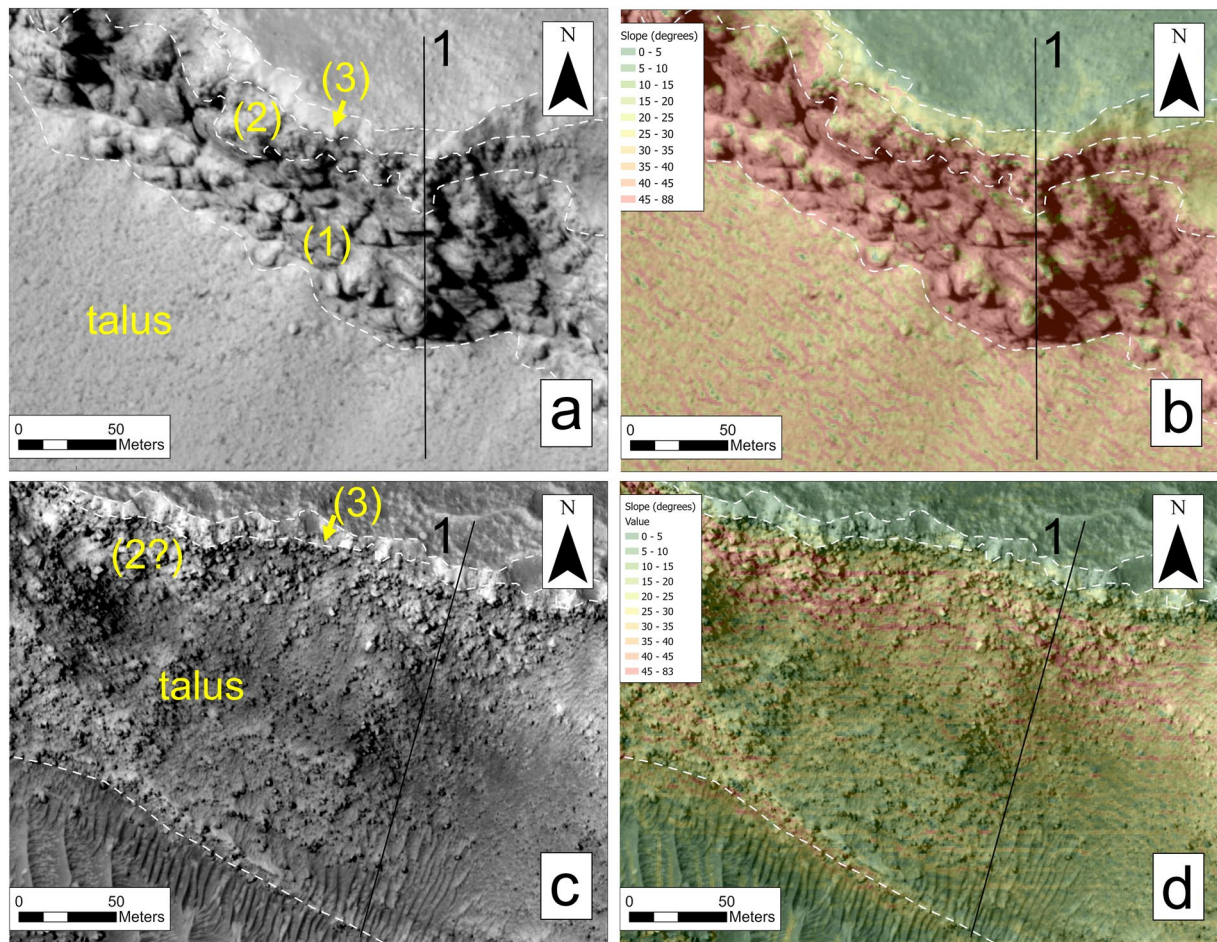


Figure 12. (a, b) Zoomed in view of Hephaestus Locality West (ESP_052638_2020) and (c, d) East (PSP_001462_2015). Slope maps and topographic profiles (profile line 1) reveal stratigraphic variations and thicknesses beneath the lava plains. Both exposures are capped by a fines-dominated slope-forming unit (3) that extends below the surface by up to 6 m. This unit is underlain at both localities by an up to ~29 m thick boulder-dominated, cliff-forming unit (2) that exceeds the angle of repose for loose, granular materials. At Locality East this unit is partially covered by mass wasting debris (i.e., talus). Locality West exposes an additional cliff-forming fractured unit (1) beneath the boulder-dominated unit that may be the primary basalt bedrock. The fractured unit appears to be entirely covered by talus at Locality East. The entire stratigraphic sequence is consistent with an impact comminuted lava plain with a gardened regolith that is tens of meters thick. The regolith fines upwards, a result of the higher frequency of small (order of 1–10 m) impacts.

2.5 m. This suggests that the units are mostly horizontal. The average thickness of the fines unit along the contacts is only ~2.0 m at this locality. Two topographic profiles reveal similar thickness relationships, suggesting a thickness range of 1.9–6.2 m for the upper unit with a slope of only 8°–10°. The boulder-dominated unit quickly transitions to talus and holds slopes between 21° and 23°.

The data from the two localities at Hephaestus Fossae suggest a consistent stratigraphy of a ≤ 7 -m-thick fines-dominated unit that grades into an underlying, ~10–30 m thick boulder-dominated unit. Below this depth, more competent bedrock is indicated at Locality West, extending down to a minimum depth of ~150 m. Other HiRISE images, stretching ~100 km along length of the exposure, confirm this general stratigraphy, including PSP_002359_2020 where the exposure was first described (Golombek et al., 2017; Warner, Golombek, et al., 2017) (Figure 3d). This suggests significant lateral stratigraphic continuity. A similar fines-dominated capping unit, interpreted here to represent a granular regolith, is visible along the entire length of Hephaestus Fossae, stretching ~300 km from exposures in the northwest to the southeastern portion of the fracture system.

Stratigraphic similarities between the Hephaestus exposure and InSight are indicated in the depth of excavation relationships of RECs/NRECs and in the relief the Etched Terrain, implying similar regolith production and geologic histories. To further constrain the geologic similarities between InSight and Hephaestus, we present impact crater statistics from the plains unit that surrounds Hephaestus Fossae. Previous mapping from Tanaka et al. (2014)

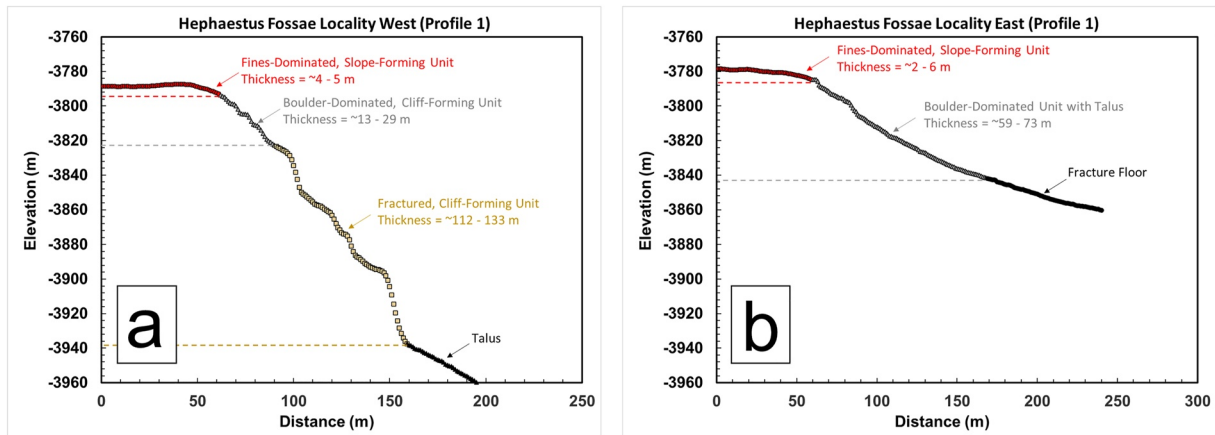


Figure 13. Example topographic profiles from Hephaestus Fossae exposure West and East. The range of unit thicknesses, determined from two profiles at each section, are shown. Locality East is likely an incomplete exposure. The base contact of the boulder-dominated unit is obscured by talus here. Locality West is a more complete exposure and uniquely displays the thickness, texture, and structure of the entire column of an impact-comminuted regolith resting on basaltic lava flows.

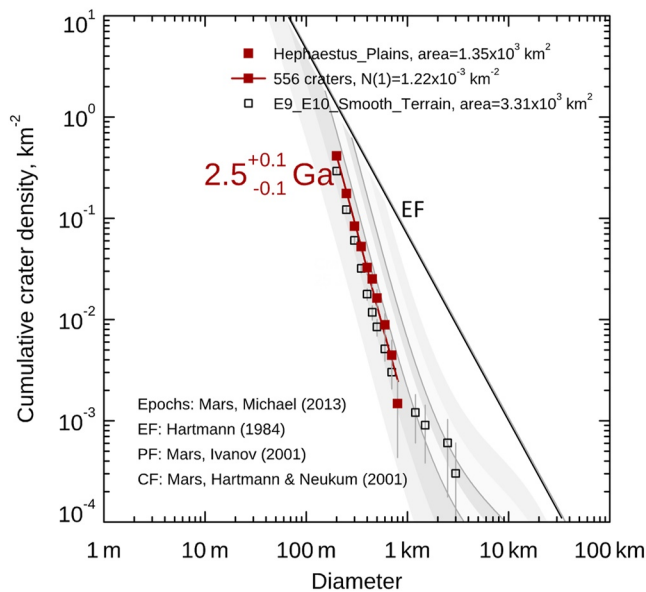


Figure 14. Cumulative crater size frequency distribution histogram comparing the crater statistics of the lava plains surrounding Hephaestus Fossae (closed red squares) to the Smooth Terrain at InSight (open black squares). The plains unit at Hephaestus Fossae has a slightly higher crater frequency for craters with diameters ≥ 200 m. The model age fit (2.5 Ga) suggests a similar Early Amazonian age to InSight (1.7 Ga). Like at InSight, the 2.5 Ga model age is interpreted here to represent the timing of crater resurfacing, likely by effusive volcanics associated with Elysium volcanism. These volcanic materials are now exposed in the walls of Hephaestus Fossae. The observed regolith stratigraphy at Hephaestus therefore represents a plausible example of the regolith stratigraphy for all Early Amazonian-age lava plains across Mars, including the Smooth Terrain at the InSight landing site. Crater production functions (PF, solid gray lines) from Ivanov (2001). Chronology functions (CF, derived model ages) from Hartmann and Neukum (2001). Martian epoch boundaries (Late Amazonian to Mid Noachian gray fill between production lines) from Michael (2013). Crater equilibrium function (EF, darker solid black line) from Hartmann (1984).

indicated a Late Hesperian age for the plains material at Hephaestus (IH) and an Early Hesperian Age for InSight (eHT) using ≥ 2 km-size craters. However, geologic mapping and crater statistics that extend to 200-m-size craters suggest that a resurfacing event buried the terrain in the Early Amazonian at InSight (Golombek et al., 2018; Pan et al., 2020; Warner, Golombek, et al., 2017). For Hephaestus, we similarly count craters down to 200 m in diameter over an area of 1,480 km² to compare both the crater size-frequency distribution and derived model ages of the two locations (Figures 11 and 14). Similar to InSight, the data covering the diameter bins from 200 m to 1 km follow an Early Amazonian production function. The cumulative frequency of craters over this range is however higher at Hephaestus than at InSight. A fit to the distribution of craters over this range provides a 2.5 Ga \pm 0.1 model age for Hephaestus where a similar fit suggests a 1.7 Ga \pm 0.1 age at InSight.

Given the stratigraphic exposure that suggests up to 150 m of regolith-covered, competent bedrock, and the presence of ghost craters near Hephaestus Fossae (Figure 11), we suggest that the 2.5 Ga model age dates the timing of volcanic resurfacing in this region of Mars, similar to the interpretation at InSight. Furthermore, the thickness of the fines-dominated unit at Hephaestus, at 2–7 m, is similar to the proposed thickness of ~ 3 m for the granular material beneath the InSight lander. The time-averaged, order of magnitude production rate for the fines-dominated regolith at both locations is therefore $\sim 10^{-3}$ m/Myr. The depth and thickness of the boulder-dominated unit at Hephaestus at ~ 10 –30 m also suggest, by comparison, that ~ 100 to 300-m-diameter craters at InSight may have excavated a coarser portion of a fractured regolith, and not competent bedrock. If the boulder-rich section of the stratigraphy is a coarsely-fractured regolith, the overall time-averaged regolith production rate at both locations is as high as $\sim 10^{-2}$ m/Myr. Both production estimates are generally consistent, within an order of magnitude, to regolith production rates (by impact gardening) reported for Hesperian to Early Amazonian-age surfaces at the Viking and Pathfinder landing sites (Hartmann et al., 2001). Furthermore, at the Gusev cratered plains, Grant et al. (2006) and Golombek et al. (2006) estimated 10 m regolith at Bonneville crater with a Hesperian age of 3.6 Ga, which also yields a regolith production rate on the order of 10^{-2} m/Myr.

5. New Observations From Lander Based Data

InSight's landing and surface operations provide a unique view into the cm-scale stratigraphy of regolith on Mars. Landing retrorockets mobilized the upper few mm to cm of sediment within *Homestead hollow*, causing visible albedo and textural changes. Pits were also excavated beneath the lander and were imaged by the IDC (Golombek, Warner, et al., 2020). Percussive hammering by the HP³ also generated a ~5 cm diameter hole in the soil, called the “mole hole”, that exposes the upper few cm of regolith. Finally, soil scraping, piling, and dumping were performed by a scoop attached to the Instrument Deployment Arm (IDA). The scrapings and piles reveal important information about the texture and cohesion of the soil in the immediate (<1 cm) subsurface, albeit after surface modification by the retrorockets. This section highlights these soil observations, including descriptions of clast morphology, texture, color, and evidence for stratigraphic variation within *Homestead hollow*.

5.1. Surface Alteration During Landing

InSight used retropropulsive pulse thruster rockets to slow the lander's descent and perform a safe soft landing (Golombek et al., 2017). Rocket exhaust from previous landings on Mars (Daubar et al., 2016; Johnson et al., 2015; Lorenz, 2016; Plemmons et al., 2008) and Earth's Moon (Clegg et al., 2014) modified the near surface by redistributing primarily fine-grained materials. This surface alteration is most easily identified as “halos” of albedo and/or color variations in visible images, especially from orbit. For Mars landing sites, alteration halos have appeared dark in orbital images because the relatively brighter dust has been blasted away, leaving behind the larger and relatively darker grains. For lunar landings, multiple halos appear due to macroscopic disruption of regolith resulting in either increased or decreased surface roughness. The pattern of surface alteration around the InSight landing site can be compared to patterns at previous landing sites and impacts to help assess the physical properties and structure from the upper few microns to few centimeters of the surface.

We leverage two primary datasets for assessing landing-induced surface alteration around InSight: images taken from orbit and taken in situ by the lander itself. The HiRISE camera (McEwen et al., 2007) acquired ~25 cm/pixel infrared/red/blue (IRB) color images of the InSight lander and surrounding terrain on 6 December 2018, and again on 11 December 2018 (Figure 15). Additionally, the IDC acquired red/green/blue (RGB) color images (Maki et al., 2018) from a height of ~1.5 m above the surface, including a panorama of mid- and far-field terrain around the lander on sol 14 or 11 December 2018 (Figure 16), as well as many more images of the surface directly south of the lander.

Similar to other landing sites, HiRISE imaging reveals the area surrounding InSight to have been darkened relative to its surroundings. Reflectance varies nonlinearly with radial distance from the lander, which we divide into four zones: a proximal inner halo, an outer halo, a directional streak, and unaltered distal terrain. At close range up to ~8–11 m radial distance, the inner halo has a 30% lower relative reflectance in the red channel compared to unaltered distal background. The inner halo is surrounded by an even lower reflectance outer halo, extending from the inner halo out to 15–21 m (~990 m² area) from the lander, with as much as a 43% lower mean relative reflectance compared to unaltered background (Figure 15). A directional streak of more moderate reflectance progressively approaching background levels extends ~100 m toward the southeast at an azimuth of 148° clockwise from North, along the expected prevailing wind direction (Golombek et al., 2018). Additionally, a discontinuous pattern of rays (showing up in blue in Figure 15a) extends up to ~5 m from the lander but is not obvious in IDC images. The IDC mosaic does show a slight darkening of the mid-field (up to ~20 m away) relative to the far-field, approximately coincident with both the outer halo edge and the rim of *Homestead hollow* (Figure 16).

A decorrelation stretch (DCS) was performed on the HiRISE image and IDC panorama to aid in identifying the boundaries of the haloes (Figures 15a and 16b). The DCS is a principal component analysis that enhances color separation in a multispectral image (here, $n = 3$ bands) that has significant band-to-band correlation. The mean pixel DN values (± 1 standard deviation) per band were also calculated as a function of radial distance in 1 m increments (Figure 15). Lander hardware and the sky were clipped from images prior to performing the stretch to focus on color differences only on the surface. The HiRISE (IRB) DCS and plots of pixel value versus radial distance show the higher-reflectance inner halo to be stronger at short wavelengths, particularly via blue channel. The IDC (RGB) panorama DCS also exaggerates the relatively higher-reflectance shorter-wavelength zone close to the lander as green/blue. The higher-reflectance inner halo also spectrally contrasts with the lower-reflectance outer halo, which appears as red, in the IDC DCS. In the HiRISE DCS, the halos contrast with the more distal

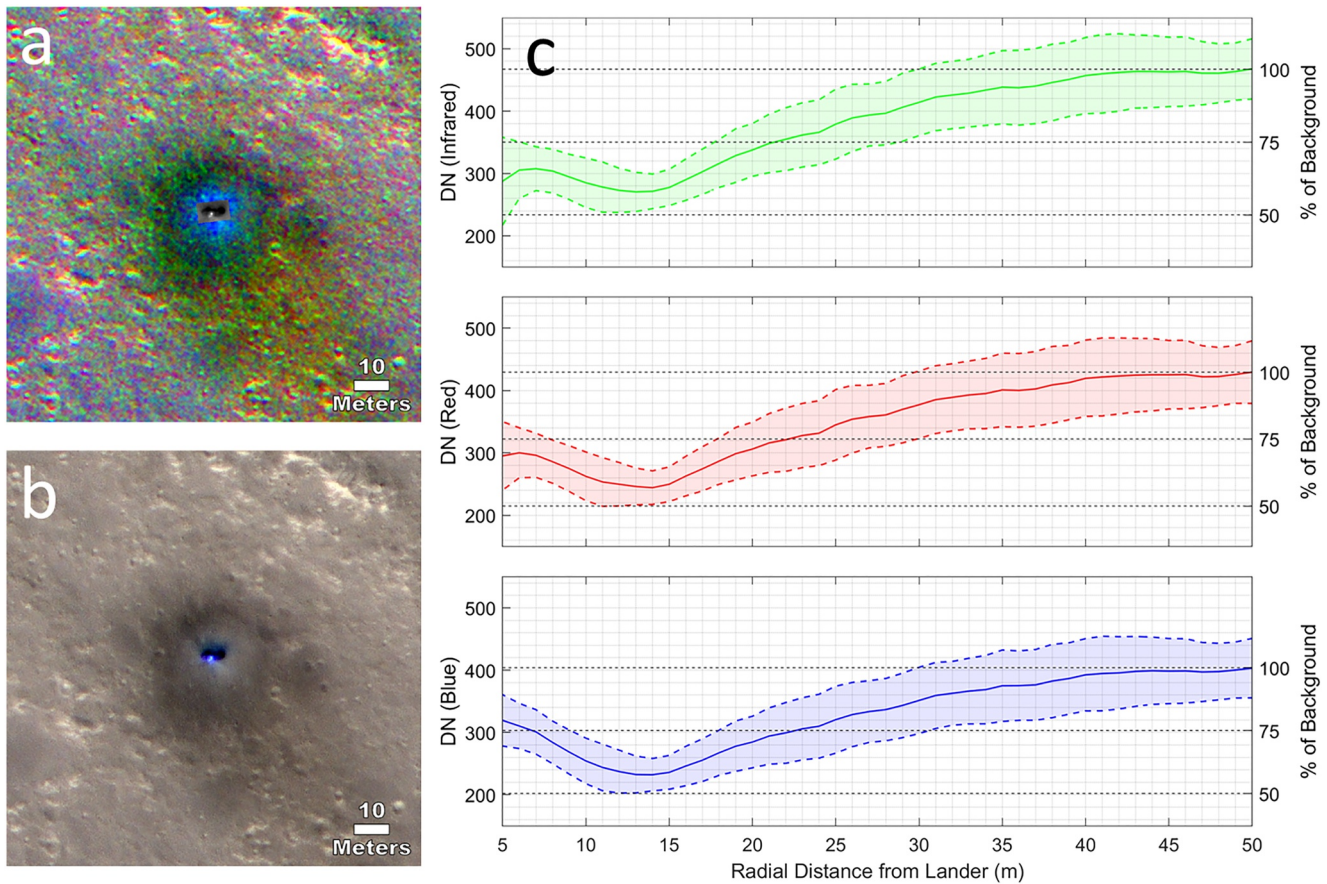


Figure 15. (a) Decorrelation stretch “DCS” of (b) HiRISE infrared/red/blue image ESP_057939_1845 taken 6 December 2018, over the InSight landing site showing the distribution of lander-proximal surface alteration. (c) Plots of the mean ± 1 standard deviation pixel digital number “DN” brightness values for each band in the non-stretched image, as a function of radial distance from the lander calculated in 1 m radial increments.

unaltered background terrain that appears more spectrally red. Surfaces of rocks facing the lander also appear green in the IDC color panorama DCS.

The quasi-circular disturbed zone of 15–21 m radius ($\sim 990 \text{ m}^2$) around InSight is remarkably consistent with the disturbed zone measured around Phoenix (same lander system) of 18 m mean radius ($1,020 \text{ m}^2$; Lorenz, 2016). Darkening of the surface by up to 43% is consistent with the expected removal of a thin layer (microns) of dust during landing, similar to previous Mars landing sites (Daubar et al., 2016; Johnson et al., 2015; Lorenz, 2016) including a $\sim 20\%$ – 40% darkening by Phoenix (Daubar et al., 2016), an average 35% darkening around fresh

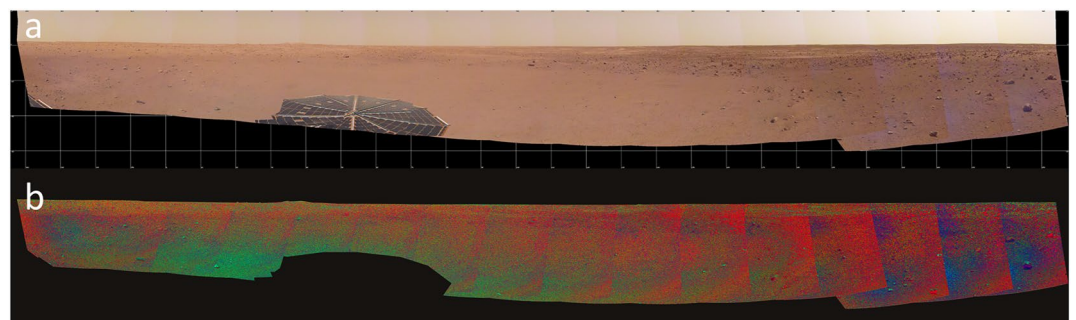


Figure 16. (a) Instrument Deployment Camera (IDC) red/green/blue mosaic taken on 11 December 2018 by the lander and (b) the corresponding decorrelation stretch “DCS” of terrain showing proximal alteration.

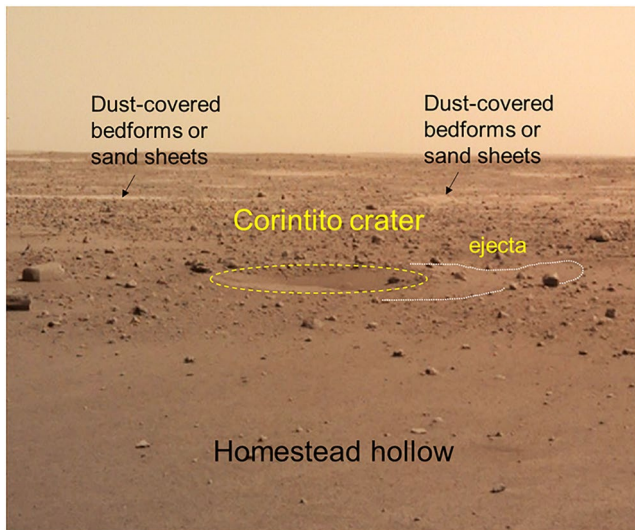


Figure 17. Instrument Deployment Camera (IDC) image (D024L0014_597777981EDR_F0103_0100M) taken on Sol 14 looking southeast from the InSight lander. The *Corintito* impact crater is 14.7 cm deep and is ~20 m from the lander. It superposes the remnant rim of *Homestead hollow*. *Corintito* has a thin, reddish ejecta blanket that is best observed here extending westward (to the right of the image) from the crater rim. In HiRISE images, the ejecta of *Corintito* has a relatively higher albedo compared to the surrounding plains, consistent with all secondary craters ejected from the young (between 0.1 and 1 Ma and 2.5 ± 0.2 Ma) Corinto impact (see Golombek, Warner, et al., 2020). Excavation of *Corintito* did not reveal bedrock. Rather, *Corintito* impacted into a loosely-consolidated regolith dominated by fine sand, which partially obscured granule to cobble-size basaltic clasts beneath. Dust coating of the *Corintito* impact ejecta likely explains its overall brighter, reddish appearance in both the IDC and HiRISE images. Darker albedo of surrounding terrain suggests a larger component of coarser, darker basaltic clasts.

impacts (Daubar et al., 2016), and analogous to the formation of typical dust devil tracks (Reiss & Lorenz, 2016). Although much brighter than the outer halo, the higher-reflectance inner halo is still darker than unaltered background and likely also had a veneer of dust removed, as well as some sand-sized particles. The blue inner halo in the HiRISE (IRB) DCS and the green proximal zone in the IDC (RGB) panorama DCS consistently demonstrate that the exposed inner halo material has a relatively stronger reflectance at shorter visible wavelengths compared to surface materials nearby.

Previous Mars landing sites have not shown high-reflectance inner halos, although they do sometimes occur near small impacts (Daubar et al., 2016). Lunar landing sites also have high-reflectance halos and are interpreted to be caused by decreased surface roughness resulting from the destruction of fine-scale “fairy-castle” structures (Clegg et al., 2014), but such delicate structures are not expected in the Martian environment. Nonetheless, with stronger alteration more proximal to the lander, small-scale surface roughness could have been affected during landing by redistributing sand and/or pebbles. The non-linear horizontal pattern of alteration seen around InSight likely results from varying levels of material removed and is likely coupled with the vertical effects of alteration. The darkest areas represented by the outer halo and directional streak likely represent only the removal of a few microns thin coating of dust, with perhaps some saltation of sand grains across the surface. More proximal areas represented by the inner halo, rays, and other features described in the following sections experienced alteration to greater depths of up to a few centimeters and include displacement of dust, sand, and larger grains up to pebbles. With dust removal typically darkening the surface, the brighter inner halo may represent exposure of a very shallow subsurface layer that is naturally higher reflectance, possibly the duricrust discussed in following sections.

5.2. Surface Observations Within *Homestead Hollow*

The landscape within and outside of *Homestead hollow* is relatively flat aside from approximately a dozen bright-reddish 1–10 m wide, soil-filled, impact craters that are located within 20 m of the lander (Golombek, Warner, et al., 2020; Golombek, Williams, et al., 2020) (Figures 4; 16). No outcrops are present within the hollow or in the walls of the small craters. The freshest craters in view, informally dubbed *Corintito* and *Corintitwo* (Golombek, Warner, et al., 2020), are morphologically similar to other young secondary craters from Corinto crater, a 14-km-diameter, fresh impact structure that is located ~800 km north of the InSight landing site (Golombek et al., 2017). The estimated age of Corinto crater is between 0.1 and 1 Ma and 2.5 ± 0.2 Ma from crater counting and superposition relationships (Bloom et al., 2014; Golombek et al., 2014; Hundal et al., 2017).

Thousands of Corinto secondaries stretch across the landing ellipse and are noted for their shallow bowl shapes and relatively bright ejecta (Bloom et al., 2014; Golombek et al., 2017). *Corintito* crater, located along the southeastern margin of *Homestead hollow*, ~20 m from the lander, is ~3 m in diameter (Figures 4 and 17). In IDC images, the region outside of *Corintito*'s rim contains dust-coated, sand sized material with an overall lower abundance of darker pebble to cobble-size clasts compared to the surrounding terrain (Figure 17). This is interpreted as ejecta, derived from the shallow subsurface. The dust-covered fines of the ejecta brighten the landscape relative to the surrounding rockier plains that contain a higher abundance of darker basaltic pebbles and cobbles, consistent with the bright ejecta pattern of Corinto secondaries visible in HiRISE (Golombek, Warner, et al., 2020). *Corintito*'s maximum measured depth is ~14.7 cm (Golombek, Kass, et al., 2020). The average depth to diameter ratio of Corinto secondaries, at 0.05 (Golombek et al., 2017; Golombek, Kass, et al., 2020), is consistent with relatively shallow (~10 cm) excavation, and the crater shape is similar to parabolic models of Corinto secondaries in HiRISE images (Golombek et al., 2017; Golombek, Kass, et al., 2020). *Corintito* indi-

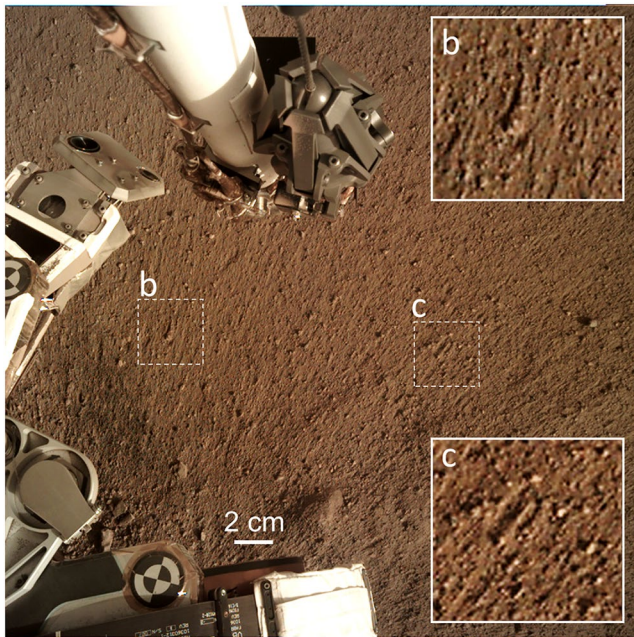


Figure 18. Instrument Deployment Camera (IDC) image (D000M0008_597253045EDR_F0000_0463M) taken on Sol 8 within the instrument deployment workspace. The surface is striated and scoured, with multi-millimeter relief ridges and troughs that extend radially away from the lander. Some granules and small pebbles have tails extending away from the lander (see inserts), suggesting that material behind small clasts has been preserved from the erosive rocket blast and the total amount of scouring is limited to several mm.

icates that the upper ~10 cm of soil at the edge of *Homestead hollow* consists mostly of fines, with a low abundance of larger and darker clasts.

A large number of color IDC images, including stereo coverage, were also acquired within the ~6 m by 4 m instrument deployment workspace that is located immediately south and in front of the lander. Aside from a slightly lower abundance of ≥ 3 cm size rocks (Golombek et al., 2021), the region in front (to the south of the lander), including the instrument deployment workspace, is texturally similar to the far RAD spot, containing granule to pebble-size clasts within a matrix of unresolvable fines (Golombek, Warner, et al., 2020; Piqueux et al., 2021). The fines at the surface of the workspace, by comparison to the RAD spot, are also likely dominated by fine sand. Examination of the prominence of rocks within and outside of the hollow indicate that rocks interior to the hollow, including in the workspace, are partially buried in the matrix of fines, consistent with a model of sediment trapping inside *Homestead hollow* (Grant et al., 2022). Imagery and DEMs of the workspace also reveal multi-millimeter relief that forms ridges and troughs that extend radial from the lander (Figure 18). This pattern is consistent with scouring of the upper few mm of granular materials by the retrorockets, which eroded a loose, fine component. The relief of the ridges and troughs, with most larger pebbles only partially buried, limits the total erosion of sand size particles to a few mm. Some granules and small pebbles have streaks or tails extending away from the lander, suggesting that fines behind the small clasts were preserved from the erosive blast.

Lithologically, larger cm-size clasts in and around the workspace consist of two types (Figure 19); one is dark-toned, gray, and aphanitic at the IDC resolution, likely corresponding to a basaltic composition, and the other is lighter toned and reddish with no visible texture and unknown composition. Based on analogy with basaltic fragments in a range of environments (including impact) on the Earth (e.g., Craddock & Golombek, 2016; Ehlmann

et al., 2017; Kumar et al., 2014), many of the dark rocks should be compact/equant with significant numbers of platy/disc-shaped and bladed fragments. Their current more platy/disc-shaped, bladed, or elongate expressions owe to the fact they are partially buried (Grant et al., 2022). Lighter reddish clasts may be equant but are also sometimes thin and platy, with angular to sub-angular edges. Many of the lighter-toned, equant clasts in the workspace may be dust covered clasts of the darker basaltic material. Dust-coated basalts are evident throughout the workspace and in the region beneath the lander. *Ace of Spades* (~30 cm) and *Turtle* (~20 cm) rocks are located immediately beneath and in front of the lander's southern footpads and are the largest examples, exhibiting dark gray surfaces that contain remnants of a reddish coating (Golombek, Warner, et al., 2020) (Figures 19a and 19d). Dust-covered rocks are abundant further from the lander, beyond the influence of the retrorockets, and are likely the norm at this location on Mars. This implies relative stability of the surface with limited dust clearing events or active sand saltation.

The reddish, platy, angular clasts are texturally and morphologically unique to all clasts in the workspace and may have a different origin from the dust covered basalts (Figure 19c). These clasts are more common proximal to and beneath the lander, where they appear to have been displaced by the lander's rockets. In some instances, the plates are broken, forming small angular pieces that sometimes appear to match indicating fracturing during transport and impact with the surface. This suggests that the clasts are less competent than the basaltic rocks. Where broken and exhumed, there is no evidence of darker material inside. Based on their color and shape (textures cannot be resolved) we interpret these clasts as exhumed remnants of a weakly-cohesive material or duricrust that rests below the sand-dominated granular surface. Weakly-cohesive, mm to cm thick encrustations on the surface of dusty and/or sandy materials have been identified across Mars in orbital thermal data (Christensen et al., 2001; Christensen & Moore, 1992; Jakosky & Christensen, 1986) and by multiple landers (Arvidson et al., 1989; Arvidson et al., 2010; Arvidson et al., 2014; Binder et al., 1977; Cabrol et al., 2006; Golombek et al., 2006, 2008; Herkenhoff et al., 2008; Jones et al., 1979; Moore et al., 1999; Mutch et al., 1977; Weitz et al., 2020). Chemical

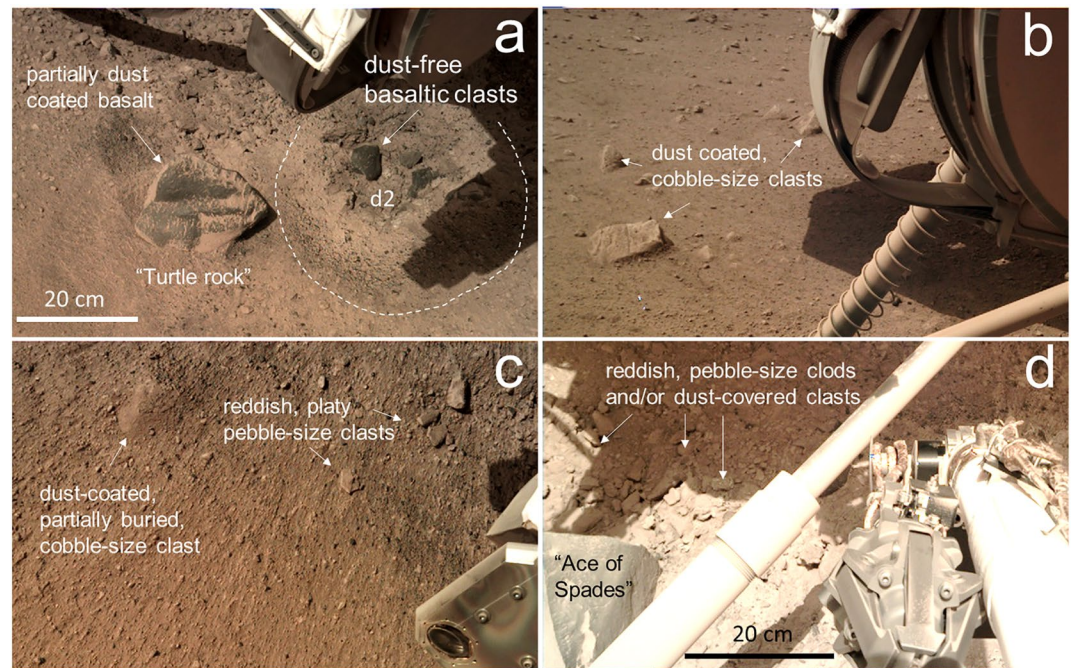


Figure 19. Instrument Deployment Camera (IDC) images displaying rocks and soils immediately beneath and in front of the lander. (a) IDC image D001L0014_597774194EDR_F0909_0010M taken on Sol 14. Partially-dust coated, angular, fine-grained, dark gray rocks are the most common clast types in the vicinity of the lander. These are interpreted to be basaltic clasts that were partially exhumed from the regolith by the lander retrorockets. Depression d2 contains a relatively high abundance of pebble-size clasts on its floor and margins. (b) Angular pebble to cobble-size clasts that are more distal to the lander rockets retained their dust coatings (IDC image D000M0014_597773743EDR_F0000_0127M) and are likely also basaltic clasts. (c) IDC image D001L0012_597601745EDR_F0101_0060M taken on Sol 12 showing platy reddish clasts that are proximal to the lander. These clasts may represent ejected remnants of the cohesive soil layer or duricrust that is visible in the excavated pits and depressions. (d) IDC image D000M0014_597774532EDR_F0000_0130M (Sol 14) taken beneath the lander's footpad strut (*Ace of Spades* rock also visible). Multiple angular, reddish clasts are visible in the region surrounding the excavated thruster pits and depressions. The clasts lack visible dark gray basaltic material and have a similar reddish color to the platy clasts and the steep walled margins of the pits. While some of these clasts may be dust-coated basalts, the clasts may also represent clods of the cohesive unit in the pits.

measurements indicate that these soils are typically sulfur and chlorine rich indicating cementation by salts that may be produced through long-term low water-rock interactions, with the Martian atmosphere (e.g., Banin et al., 1992; Haskin et al., 2005; Hurowitz et al., 2006). The depth to the duricrust at InSight cannot be inferred from the workspace images, but instead requires a three-dimensional view that is enabled by the retrorocket pits and HP³ mole hole.

5.3. Sedimentology and Stratigraphy of the Retrorocket Pits and Depressions

The IDC camera was able to acquire images under the lander with sufficient precision to create a mosaic of orthorectified images and a partial DEM with postings at 1–2 mm/pixel. The IDC images display the partial sinking of the front lander footpads, consistent with an upper surface that is comprised of loose material that is load bearing (Figure 20). A small bulge of granular material is evident on the south edge of the southern footpads that suggests the lander slid very slightly during landing. The southeastern footpad shows evidence of near complete burial by up to a few cm of granular material.

The shock wave from the retrorockets on InSight led to substantially more erosion than conventional jets (Mehta et al., 2011, 2013; Plemmons et al., 2008). The same pulsed thrusters on Phoenix excavated 5–18 cm of soil beneath the lander to uncover hard subsurface ice that prevented further erosion (Mehta et al., 2011). Three larger pits (P1, P2, and P3) and smaller depressions (d1, d2, and d3), excavated by the retrorockets during InSight's landing, are visible in IDC images acquired on Sols 14–18 (Figures 21 and 22). The larger pits are closer to

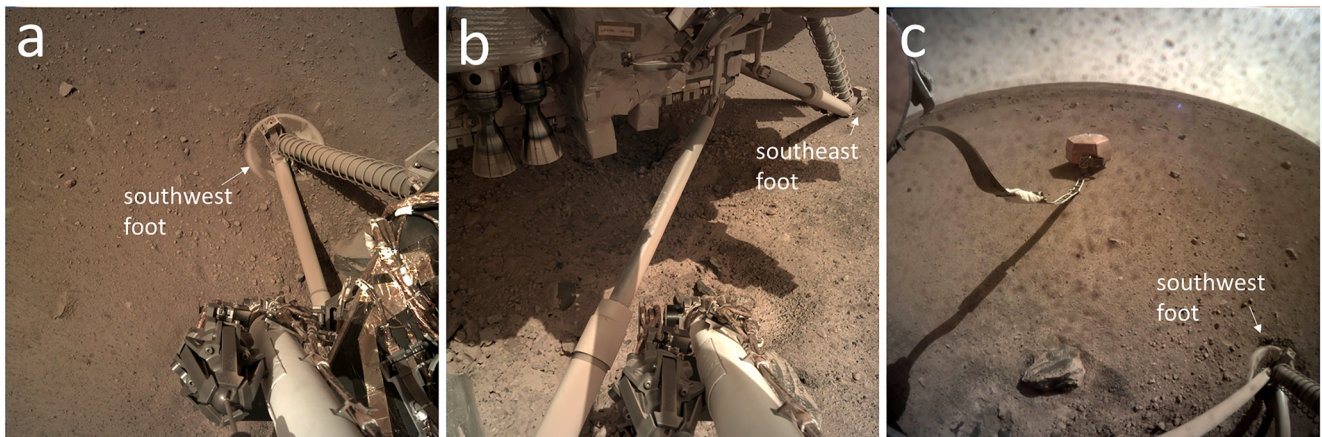


Figure 20. Instrument Deployment Camera (IDC) images (a) D000M0010_597416083EDR_F0000_0125M (Sol 10) and (b) D000M0014_597773991EDR_F0000_0126M (Sol 14) showing the southern lander footpads. The footpads are partially buried in the upper few cm of loose soil and a bulge in the granular material occurs on the southern edge of the footpad suggesting slight southward-directed translation of the spacecraft upon landing. (c) Instrument Context Camera (ICC) image C000M0030_599199818EDR_F0000_1400M on Sol 30 showing a view of the southwest footpad and soil bulge to the south of the footpad (blotches are dust on the camera lens). These collective observations suggest that the upper few cm of the regolith at the landing site is loosely consolidated and load bearing.

the northern portion of the lander, are up to ~12 cm deep, and ~50 cm-in-diameter. The sub-surface material in the pits is composed of only a few scattered dark-toned aphanitic basaltic pebbles. Instead, brighter reddish, pebble-size clasts are more abundant here, occurring within a reddish finer-grained matrix or loosely scattered on the pit floors and along the pit rims. Similar to the dust coated basalts at the surface, they are equant in shape and angular to sub-angular. Some of the clasts in the pits show partial red coatings, exposing dark gray basaltic material beneath. However, the majority of the clasts lack evidence of dark gray material and are in a much higher abundance here relative to basaltic rocks and similar reddish clasts within the workspace. The high abundance and association with pit excavation suggest the brighter clasts are clods or clumps of the relatively thick, more cohesive duricrust (Golombek, Warner, et al., 2020).

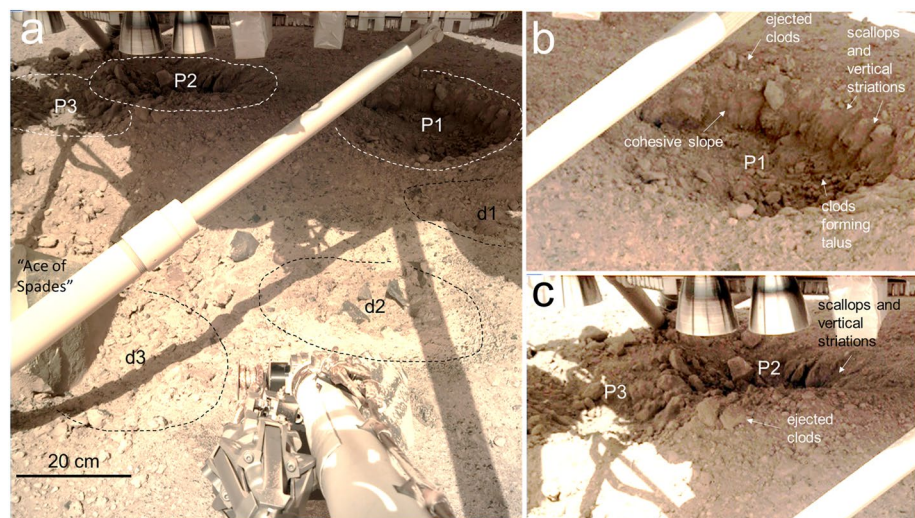


Figure 21. Instrument Deployment Camera (IDC) images taken beneath the lander on Sol 18 (D001R0018_598131636EDR_F0606_0010M). (a) The pits and depressions were excavated by the lander's pulsing retrorockets. P1 (b) and P2 (c) are the largest and deepest pits. (b) P1, the deepest pit, is ~50 cm in diameter and reveals ~12 cm of the shallow stratigraphy. The pit walls are vertically Etched and steep (see Figures 22 and 23) and likely expose an up to ~10-cm-thick cohesive duricrust. The floor of each pit contains abundant reddish, pebble-size clasts or clods of material that broke off the steep pit walls. The pit rims also have abundant clod-like materials and a few pebble-size basaltic clasts that were ejected from the pits by the thrusters.

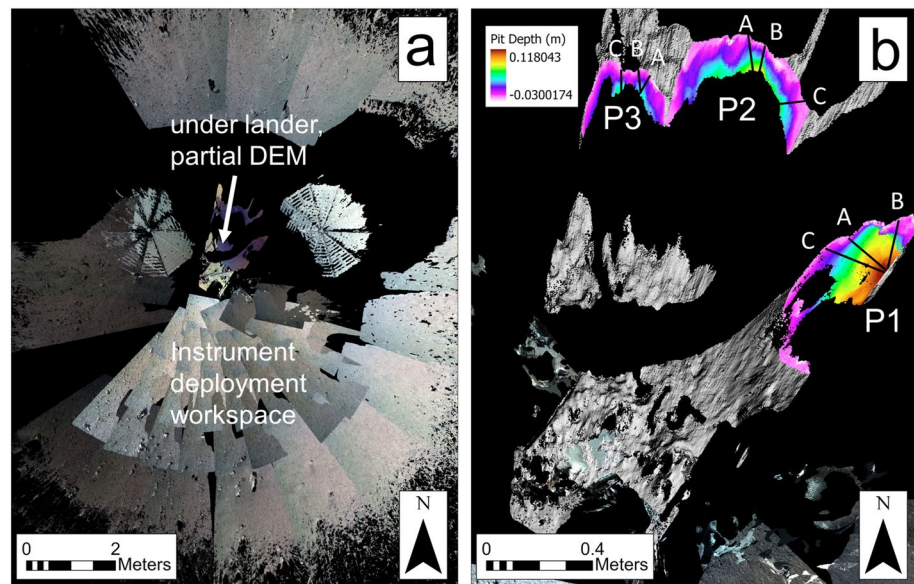


Figure 22. (a) A partial 360°, 1 mm/pixel Instrument Deployment Camera (IDC) mosaic including the location of the instrument deployment workspace to the south of the lander. The mosaic represents the region of available stereo coverage. Partial stereo coverage is also available beneath the lander. Here, 1 mm/pixel orthoimages were used to construct a ~ 1.3 mm digital elevation model that partially covers pits P1, P2, and P3. (b) Hillshade relief of the under-lander DEM and DEM of the pits showing the measured depth of each pit. Pit P1 is the deepest at ~ 12 cm. Three profiles (A, B, and C) were constructed across each pit to measure pit depth and slopes (see Figure 23).

Each pit is scalloped at the cm-scale in planform. In cross-sectional view, the pit walls are marked by columns or vertical etchings that extend downwards from these scallops. The scallops and etchings are interpreted here as scour marks in the soil from the downward pulsing retrorockets. The soil exposed along the pit walls and within the scours is fine-grained (with a few observable pebble-size clasts) and was capable of holding the scalloped and scoured texture for up to 18 Sols without collapsing by mass wasting, indicating some cohesion. The partial under-lander DEM that was generated from the Sol 18 data also indicates variable pit wall slopes that in places far exceed the angle of repose for loose granular material (Figure 23). The steepest slopes in the pits, measured here along six profiles in P1, P2, and P3, range between 50° and 60° . The steeper slopes begin at a relatively consistent depth of 1–2 cm beneath the rim of the pit walls and extend downwards to a maximum observable depth of ~ 10 cm before the wall is partially obscured by pebble-size clasts. There are no smooth, conical debris piles at the pit base that might be consistent with slope replacement by mass wasting of loose sand. Instead, the reddish equant clasts form small pebbly piles of talus that collected from material that wasted from the pit walls after excavation. The clasts outside of the rim were ejected by the downward force of the pulsed retrorockets. The reddish clasts, both inside and outside of the pits, have a similar texture to the cohesive pit walls and are likely clods of the soil that were removed during excavation without completely disaggregating. Above the steeper slopes, at consistent depths of 1–2 cm, the rim walls are at or near the angle of repose ($\sim 30^\circ$), suggesting the presence of less cohesive, more loosely granular material. The slope break between the granular material and cohesive material is best observed in the largest pit, P1, along its northern (south-facing) slope (profile P1-B) (Figures 22 and 23). A loose, granular surficial layer is consistent with the radial streaks in the surface and slight sinking of the lander feet (Figures 19 and 20).

The shallower, lower sloping depressions d1, d2, and d3 are located beneath the southern portion of the lander (Figure 19a). Depression d2 was imaged closely, and in stereo, by the IDA. It is ~ 6 -cm-deep and exposes a concentration of dark gray granules to small pebble-size clasts down to a depth of ~ 1 –2 cm. Below this, the walls are steeper and expose finer, brighter red material that contains few larger, dark cm-size pebbles down to a depth of ~ 4 cm. The base of the pit contains abundant large, dark gray pebbles. The lower margins/flanks of these pebbles exhibit partial dust cover, suggesting that their darker tops were exhumed from a reddish, fine matrix

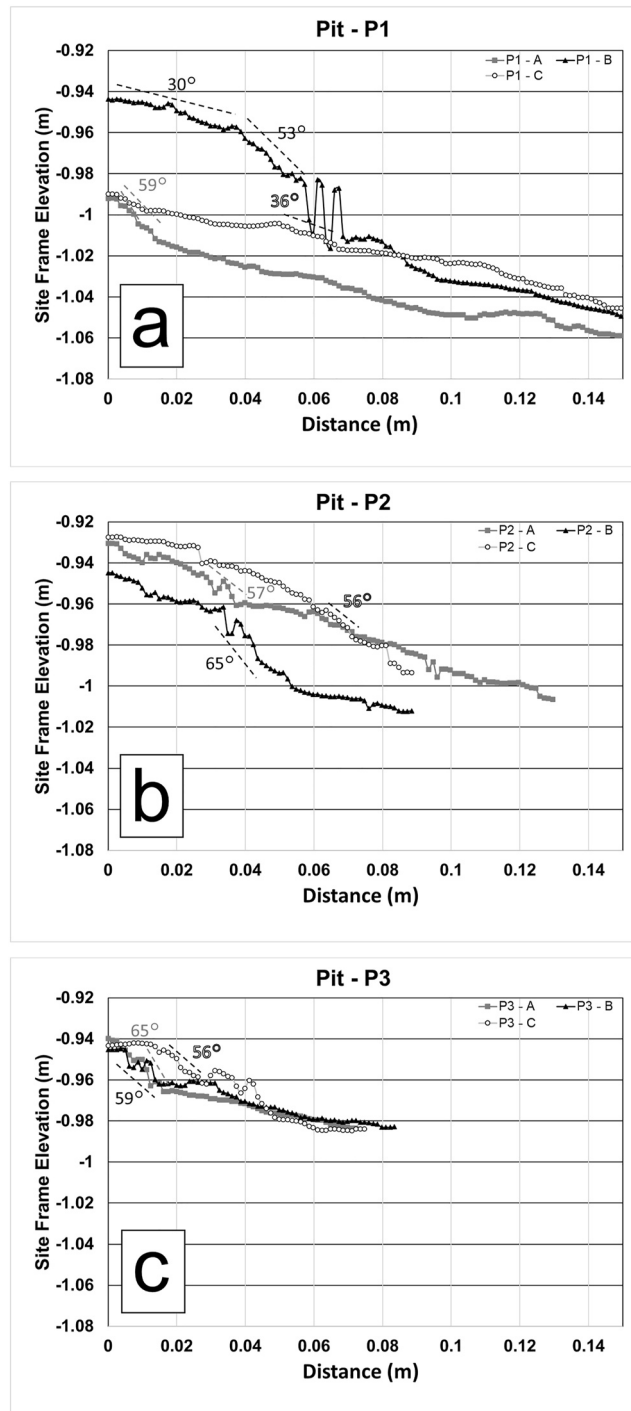


Figure 23. Pit topographic profiles for (a) P1, (b) P2, and (c) P3. The location and magnitude (in degrees) of the steepest slopes in each pit are illustrated. In all cases, the steepest walls of each pit exceed the angle of repose for unconsolidated, sand-size granular material (normally 30–40°). Profile B of Pit P1 is the most complete vertical profile, showing the upper ~12 cm of soil. The upper 2 cm of profile B in P1 reveals a material that holds a slope of ~30°, consistent with the presence of loosely-consolidated fine sand. Beneath this horizon, the pit slope increases to 53° suggesting the presence of a more cohesive layer. This steep horizon extends to a depth of ~8–10 cm where it is obscured by the talus of clods/clasts at the base of the pit wall. In almost all pits, the steep pit slopes begin at a relatively shallow depth 1–2 cm, suggesting that the cohesive duricrust layer rests immediately below the loose granular surface at the landing site.

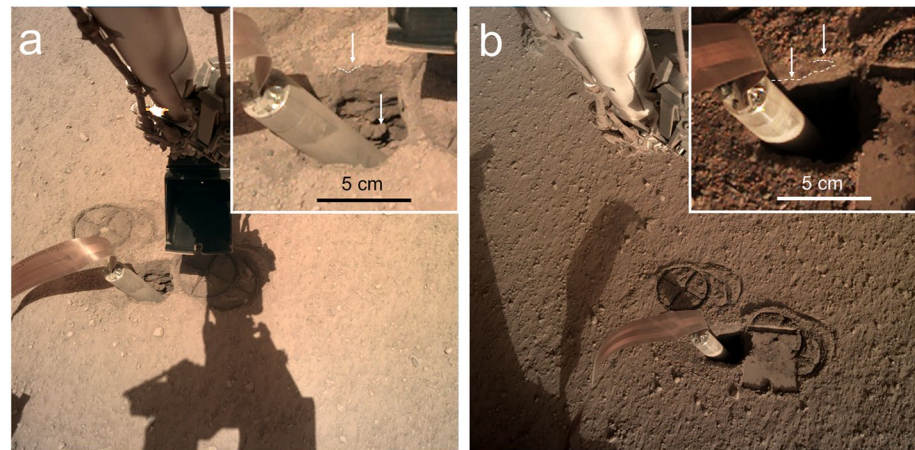


Figure 24. (a) Instrument Deployment Camera (IDC) image D000M0235_617388344EDR_F0000_0250M taken on Sol 235 showing the HP³ mole, mole hole, and HP³ support structure foot impressions. The mole hole exposes ~5 cm of the regolith (see Figure 24). The top white arrow points to a thin transition between the bright, dust-coated surface and darker sandy material beneath. The lower white arrow highlights an exposed clast or clod within the upper column of the duricrust. Multiple, shadow-forming overhangs are also present, suggesting multiple cm-scale horizons of soil with variable strength. (b) IDC image D000M0240_617848315EDR_F0000_0829M taken on Sol 240 under different lighting conditions. The upper arrow points to a brighter, upper, dust-mantled surface. The dashed line highlights an albedo and color transition to darker, sandy materials (lower white arrow). The lower dashed line marks a possible second transition to a brighter material that may represent the upper surface of the duricrust. The overhanging horizons are present below this lower dashed line. The ~1 cm deep IDA scoop impression can also be seen.

of material that can adhere to rocks. Some variability in clast color and texture is evident in both depressions although all observations are at the limit of IDC image resolution.

The combined pit/depression observations indicate that InSight rests on a regolith/soil that consists largely of fines that contain a variable abundance of \geq granule-size basaltic clasts as float. Comparisons with the rock abundance at the surface of *Homestead hollow* suggest that the near surface rock abundance may not exceed 2%–3% CFA for clasts \geq 3 cm in diameter (Golombek et al., 2021). Furthermore, in both the pits and depressions, the steepest slopes are held up by a bright-reddish, fines-dominated unit that is located only ~1–2 cm beneath the surface. This unit corresponds to the vertically-Etched, clod-producing material seen in P1–P3. Depressions d1 through d3 do not have a similar Etched, steep wall, but exhibit a brighter-toned, reddish horizon that corresponds with the steepest slope in the depression. We interpret this as weakly-cohesive material or a duricrust. From these direct image observations, the duricrust is at least ~10 cm thick, measured from the base of the loose, granular layer down to the maximum observable depth of the deepest pit floor.

5.4. Mole Hole Characteristics

The HP³ mole hammering provides additional constraints on the upper few cm of soil stratigraphy. During sol 76 (12 February 2019), HP³ was placed on the ground ~1.5 m from the lander. The first hammering of the mole began a few days later and quickly penetrated ~37 cm into the soil (Grott et al., 2021; Hudson et al., 2020). At this depth, the mole failed to continue its penetration. Ongoing hammering resulted in shifting of the HP³ surface support assembly from its original position and broadening of the mole hole to a diameter of 5 cm, almost twice that of the mole itself. Hammering was subsequently stopped and the HP³ surface support assembly was lifted and re-positioned by the IDA to visualize the hole and state of the mole. An intensive IDC imaging campaign followed enabling stereo views of the soil and mole and showed very steep walls (Figures 24 and 25). The team concluded that the mole failed to penetrate due to a loss of friction with the hole wall (Hudson et al., 2020). The material comprising the mole hole failed to collapse, suggesting cohesion. Analysis of the response of the mole to hammering further suggests a weakly cohesive layer or duricrust that is <20 cm thick with loose unconsolidated material beneath and perhaps a pebble rich layer at the maximum penetration depth of ~37 cm (Hudson et al., 2020).

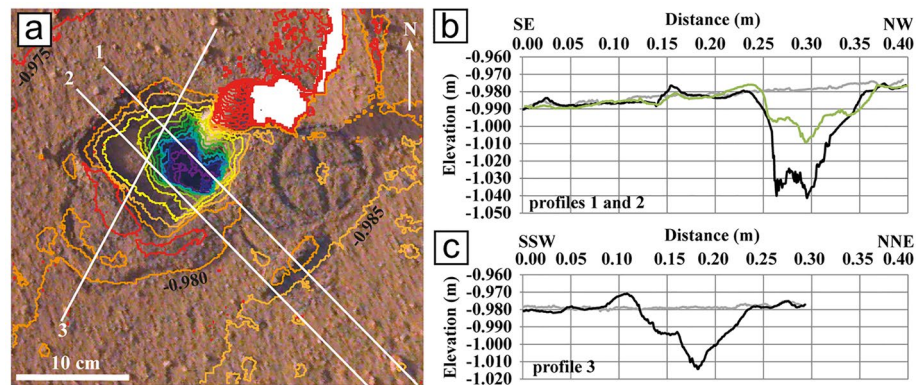


Figure 25. (a) Ortho-rectified Instrument Deployment Camera (IDC) image and DEM acquired on sol 417 showing the mole hole. Color lines are height contours at intervals of 5 mm. White areas have no data. (b, c) Topographic profiles across the hole. The light gray lines correspond to pristine profiles acquired on sol 14 before HP³ deployment and mole penetration. The dark black profiles correspond to topographic profiles 1 and 3 on (a). The green profile line corresponds with profile 2 on (a). The maximum depth of the mole is ~5 cm.

The mole hole is straddled by circular imprints of the HP³ feet that are a few mm deep (Figure 24). The smooth imprints occur within an upper, loose, layer that is composed of intermixed sand and dust. This layer of loose material overlies the observed duricrust. The eastern rear foot of HP³ was partially covered by some of this material which continued to adhere to the instrument after the housing was lifted by 50 cm and re-deposited on the surface. To support mole penetration, the soil adjacent to the hole was compressed by the scoop attached to the IDA. The objective of the compression experiments was to collapse the mole hole, enabling the required friction between the wall and the mole. The first imprint made by the scoop was ~0.5 cm deep and formed a relatively flat surface (Figure 24b). Ongoing compression of the scoop into the soil created a ~1 cm deep depression that implies compressibility and therefore porosity of the upper, loose layer.

Well illuminated IDC images and DEMs taken of the mole hole, between Sol 235 and Sol 417, reveal ~5 cm of exposure in the hole wall. The upper ~1–2 cm are composed of relatively dark fine sand with sparse granules, capped by a thin layer (likely microns) of reddish dust (Figure 24). This loosely-consolidated layer appears to cap the entire interior of *Homestead hollow*, except where retrorocket excavation was the strongest. Below this, a coarser horizon of granules and small, ~5 mm-size, reddish, sub-rounded to sub-angular pebbles is visible within the mole hole. Like the pits, these clasts are either dust-coated basaltic pebbles or clods of the duricrust. Steep, shadow-forming overhangs are also present in the hole wall that suggest cohesion of the soil at the cm-scale and/or resistance of harder granules/pebbles that are anchored in the soil. Similar overhangs are visible where clasts or clods protrude from the walls of the retrorocket pits suggesting that the pebbles and clasts are cemented among the finer matrix. Some of the clasts that line the bottom-most portion of the hole exposure appear to consist of an aggregate of coarse sand/granule grains, suggesting a duricrust clod origin (Marteau et al., 2021).

Despite the hammering results and image observations of the soil that indicate cohesion, thermal conductivity measurements from HP³ indicate a low soil thermal conductivity, low soil density, and a high porosity (~60%) for this material that is more consistent with loosely consolidated, fine sand with little to no cohesion (Grott et al., 2021) (Section 3.2). To date, the thermal characteristics have not been reconciled with the image observations and mechanical experiments that indicate a duricrust.

5.5. Soil Characteristics From IDA Pressing, Scraping, and Dumping Experiments

Prior to landing it was recognized that much could be learned about the mechanical properties of the soil by using the scoop attached to the IDA (Golombek et al., 2018). Specifically, forces acting on the IDA can be derived from motor currents in the arm as was done with both the Viking and the Phoenix lander robotic arms (Moore et al., 1987; Shaw et al., 2009). Scraping, trenching, and scooping activities can be used to determine standard soil parameters such as cohesion and angle of internal friction (from the angle of repose). Elastic parameters could

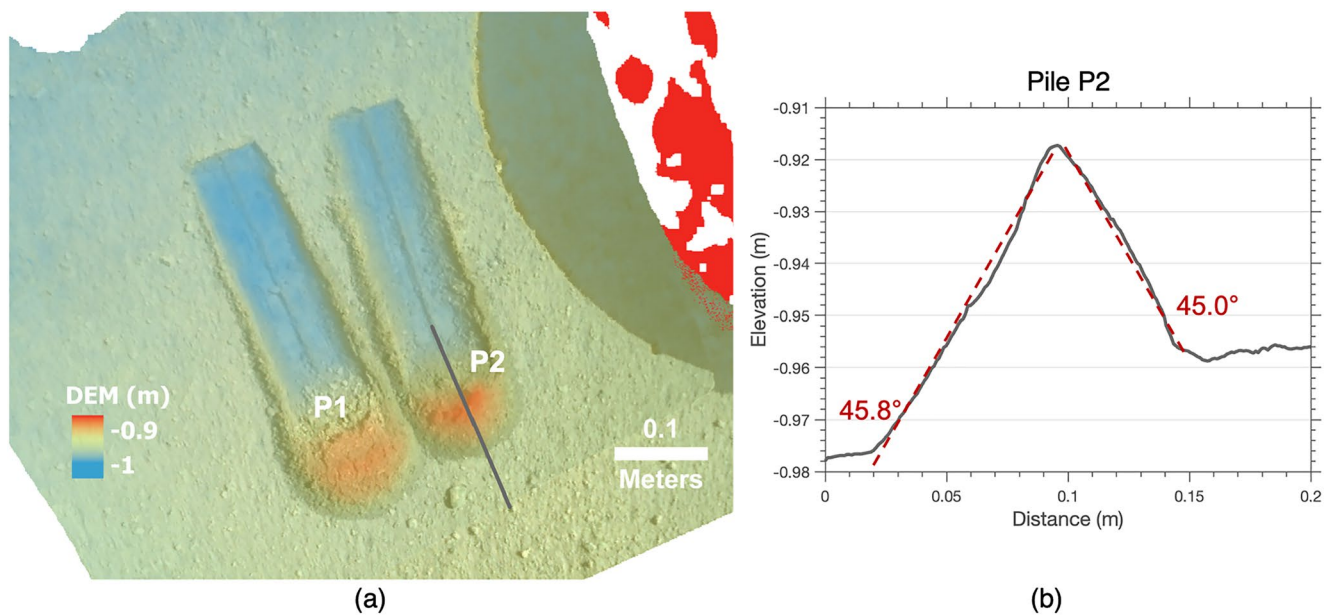


Figure 26. (a) A ~1 mm DEM overlay on an Instrument Deployment Camera (IDC) orthophoto acquired on Sol 803 showing the scoop scrapes and piles. The elevation profile of scoop pile P2 (b) reveals slopes ($\sim 45^\circ$) exceeding the angle of repose of loose, fine sand. The scrape piles likely include some component of the underlying cohesive duricrust.

also be derived by indentation experiments and SEIS measurement of accelerations from the ground tilt (e.g., Golombek et al., 2018).

The force applied by the scoop during the attempt to collapse the mole hole, as well as slope analyses of small soil piles made by scraping experiments, enabled an assessment of the resistance and cohesion of the soil in the upper few cm around the hole (Marteau et al., 2021) (Figure 24). The results suggest an angle of internal friction of 30° – 35° and a cohesion of 2–14.5 KPa (Marteau et al., 2021). The cohesion values are consistent with weakly to more strongly cohesive sandy soils, with the upper limit slightly exceeding soil cohesion values for other landing sites on Mars (e.g., Arvidson et al., 2014; Golombek et al., 2008; Herkenhoff et al., 2008; Moore et al., 1999).

The arm and scoop were later used to bury the SEIS tether between the edge of the wind and thermal shield (WTS) and the pinning mass (about 20 cm) with soil to reduce thermal noise. To accomplish this, a large number of soil scrapes were conducted between the HP³ and SEIS to create soil piles (Figure 26a). The scrapes targeted the topmost unconsolidated layer of soil to avoid the stronger duricrust. For the majority of scrapes, strong material was not encountered indicating that the surface layer of unconsolidated fine-material is ~ 1 – 3 cm thick (as deep as the scrapes). In a number of cases, clods of soil after scooping the soil were visible while the sample was still inside of the scoop. The clods disaggregated upon impact and were not present in the piles after dumping. The clods were likely derived from the uppermost surface of the cohesive duricrust layer that is only a few cm beneath the unconsolidated layer. The majority of the soil dumped from the scoop visible is dominantly fine grained, composed of individual particles below the resolution of the IDC (~ 1 mm), indicating mostly sand sized grains. Some granules and pebbles are observed with an abundance similar to that of the workspace.

Elevation profiles were extracted from IDC DEMs obtained between Sols 803 and 822 to measure the slopes of the scraped walls and dumped piles (Figure 26b). The mean slope of the regolith piles created by scraping is $42^\circ \pm 2.7^\circ$ with a range from 40° to 45.8° . The interior sides of the scraped walls have slope values with a mean of $54.7^\circ \pm 6.6^\circ$ with a range from 46° to 63° . At its highest point, the height of the dumped piles on the SEIS tether is ~ 3 cm and the material rests at slope values with a mean of $24.1^\circ \pm 6.1^\circ$ with a range from 16.6° to 32° . It is worth noting that, because the amount of soil deposited was not sufficient to confirm that the maximum possible inclination of the slope had been reached, the slope value of 24.1° for the dumped pile provides only a lower bound estimate of the angle of repose. Difference in slope angles between the scraped and dumped piles are likely due to the difference in how the piles were formed. Piles obtained by scraping typically yield different geometries

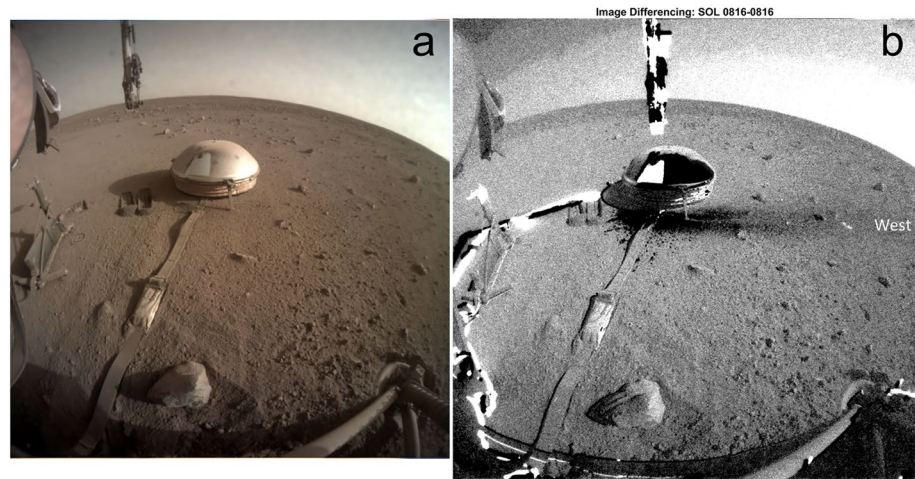


Figure 27. Instrument Context Camera (ICC) images of the Seismic Experiment for Interior Structure (SEIS) and HP³ to the south of the lander obtained on sol 816. (a) shows ICC image with soil scrapes to the east of SEIS. A scoop of soil was dumped onto the wind and thermal shield (WTS) and the tether below from a height of 55 cm in the first attempt to bury this portion of the tether. The soil cleared the dust off the WTS (brownish material) creating the white area. (b) shows differenced ICC images, before and after the dump) showing darkened area on, around and to the west of the WTS. Initial hypotheses were that the dark area was produced by the addition of dark soil or by sand size particles that impacted the surface and kicked the dust into suspension in the atmosphere. Dispersion of soil onto the solar arrays that improved power generation indicated the latter process was the cause.

and soil bulk densities than piles formed by pouring the material from a given height (Hamzah et al., 2018; Jiang et al., 2017). As a result, the slope value of 24.1° obtained from the dumped pile is interpreted as a lower bound estimate of the internal friction angle of the regolith in a loose state while the value of 42° obtained from the scrapped piles corresponds to the internal friction angle of the soil in a denser state. In addition, the slopes of the side walls left by the scoop's scrapes are larger than the slopes of the piles, and slope failure was not observed on these walls. This result can be explained by the presence of some cohesive forces in the undisturbed soil, which is consistent with the measured cohesion values.

Following the scraping and piling experiments, the piles of soil were lifted and dumped on the WTS from a height of 55 cm. The dumped soil removed dust from a portion of the WTS, was deposited on other areas of the WTS, and left an ~0.6 m elongated dark zone in differenced (before and after) ICC images downwind (toward the west) (Figure 27). The length of the elongated dark zone scales with the wind speed, with stronger winds creating longer dark zones (>2 m). The dark zones were created by sand particles entrained by the wind during freefall (e.g., Holstein-Rathlou et al., 2010) that were either deposited on the surface and/or impacted the surface kicking the dust into suspension. After tether burial, four solar array cleaning experiments were also performed (along with a number of additional scrapes to create piles of soil) in which scooped soil was similarly dumped on the western edge of the lander deck. Sand was dispersed by the wind onto the western solar array, which measurably improved power generation.

The dispersion of soil during the dumps provides information on the particle size of transport. Transport is dependent on the drag by the wind and gravitational forces (Holstein-Rathlou et al., 2010). Sand sized particles are most easily moved under the observed atmospheric winds and further argues that the soil is dominantly composed of sand (e.g., Greeley & Iversen, 1987; Greeley et al., 1980; Iversen et al., 1976; Sullivan et al., 2005; Sullivan et al., 2008; Weitz et al., 2018). The improvement in solar array power indicates that the sand dispersed by the wind impacted the solar array with sufficient kinetic energy to kick the surface dust into suspension and that the area cleaned of dust exceeded the area of the sand particles (estimated to be a factor of ~100 greater). Finally, although some granules were observed to move on the surface and across the surface of the deck (Baker et al., 2021; Charalambous et al., 2021), there was no solar array cleaning except during the dumps. This indicates the threshold friction wind speed needed to induce saltation on the deck is higher than the measured winds (even at the height of the lander deck), which is consistent with the limited observed grain motion at the site and dearth of eolian bedforms observed from the lander.

6. Summary of the Stratigraphy and Geologic History at the InSight Landing Site

Pre-landing and post-landing geological assessments of the InSight landing site have converged on a multi-scale stratigraphic model for this region of western Elysium Planitia. InSight not only landed on a regolith-covered lava plain as expected but landed within a degraded impact crater that provides important constraints on both the meter and cm-scale stratigraphic architecture beneath the lander. The stratigraphic model is summarized in Figure 28. A summary of the stratigraphic constraints and overall geologic history of the landing site is bulleted in sequence from oldest to youngest below.

1. Clastic rocks of possible sedimentary origin were deposited mostly in the Noachian in western Elysium Planitia at depths ≥ 170 m (Golombek et al., 2018; Pan et al., 2020; Warner, Golombek, et al., 2017). Some of the sedimentary units are layered and contain phyllosilicates, similar to other Noachian terrains on Mars that indicate aqueous alteration (Pan et al., 2020).
2. Landscape degradation, including Early Hesperian-age volcanic resurfacing and erosion, occurred immediately after 3.6 Ga. This was followed by complete resurfacing of the landscape by up to ~ 170 m of effusive volcanics in the Hesperian to Early Amazonian (Warner, Golombek, et al., 2017). Emplacement of up to ~ 140 m of Early Amazonian lavas was preceded or interrupted by deposition of likely clastic materials of unknown origin at depths between 30 and 75 m (Hobiger et al., 2021). It is unclear whether fluvial sedimentation could have occurred in the Late Hesperian to Early Amazonian in this region of Mars, corresponding with the late-stage activity that has been identified at discrete locations across the planet (e.g., Grant & Wilson, 2012; Kite et al., 2017), including nearby Gale crater (Figure 1) (Grant et al., 2014; Grant & Wilson, 2019). If so, the Hobiger et al. (2021) unit may represent a previously unidentified pulse of fluvial/sedimentary activity that influenced the far reaches of the northern plains. However, a mechanism for fluvial sedimentation on the northern plains at this location, distal to any elevated topographic features or notable channels in the southern highlands, is not evident. Rather, emplacement of a sheet of eolian sediments (e.g., an erg) or deposition of airfall deposits (volcanoclastic or dust airfall) that interrupted the effusive volcanic sequence are plausible explanations, particularly given the proximity of the Medusa Fossae Formation that has been shown to underlie Amazonian-age, Elysium volcanics just ~ 200 km east of the InSight landing site (Golombek et al., 2017, 2018) (Figure 1). The low velocity zone could also represent a time break in effusive volcanism that allowed for regolith development. However, the thickness of the Hobiger et al. (2021) unit, at ~ 45 m, is thicker than the regolith that superposes the Smooth Terrain and therefore would require a significant ~ 2 to 3 billion year time break, given estimated regolith production rates for the Hesperian to Amazonian (this study and Hartmann et al., 2001).
3. The surficial regolith on the Smooth Terrain was produced by impact gardening and eolian modification (including infilling of impact craters) from ~ 1.7 Ga. The maximum depth of the total column of comminuted regolith is ~ 10 – 30 m, based on comparisons to analog locations (e.g., Hephaestus Fossae) and other landing sites (Golombek et al., 2006; Hartmann et al., 2001). The thickness of the fines-dominated surficial regolith is ~ 3 m. Smaller RECs and nested craters require some boulder-rich horizons within the regolith as shallow as ~ 2 – 3 m that likely reflects heterogeneities in the random distribution of impacts responsible for the regolith. Time-averaged regolith production rates are (order of) 10^{-2} to 10^{-3} m/Myr averaged over the entire exposure timescale.
4. The *Homestead hollow* impact occurred in the Middle Amazonian between ~ 400 and ~ 700 Ma (Warner, Grant, et al., 2020). The target material was a moderately mature regolith that includes blocky impact ejecta from older neighboring ~ 100 -m-scale craters (Grant et al., 2020; Warner, Grant, et al., 2020). The pristine crater was ~ 3 m deep with a ~ 0.7 m high rim.
5. *Homestead hollow's* interior filled with lenses of sand to pebble-size materials, derived from mass wasting/hillslope creep of interior slopes. The lenses most likely thin toward the crater interior and inter-finger with stratified, well-sorted, eolian sands that we infer would be planar to cross-laminated. Deflation and ongoing impact gardening, largely by 10 cm to 1-m-scale craters, helped to reduce the rim height of the crater and exhume pebble to cobble-size rocks (with the occasional boulder) that were embedded in the matrix of sand. The bulk of crater rim degradation and filling occurred within ~ 50 Myr of formation during the Middle Amazonian at a degradation rate of 10^{-2} m/Myr (Warner, Grant, et al., 2020).
6. The younger, 100-m-diameter *Sunrise* crater impact formed about 400 m to the east of *Homestead hollow* but ejected boulders did not make it to the hollow. However, smaller clasts from *Sunrise* may be present within the hollow's fill. The cumulative size frequency distribution of craters at a similar state of degradation in the

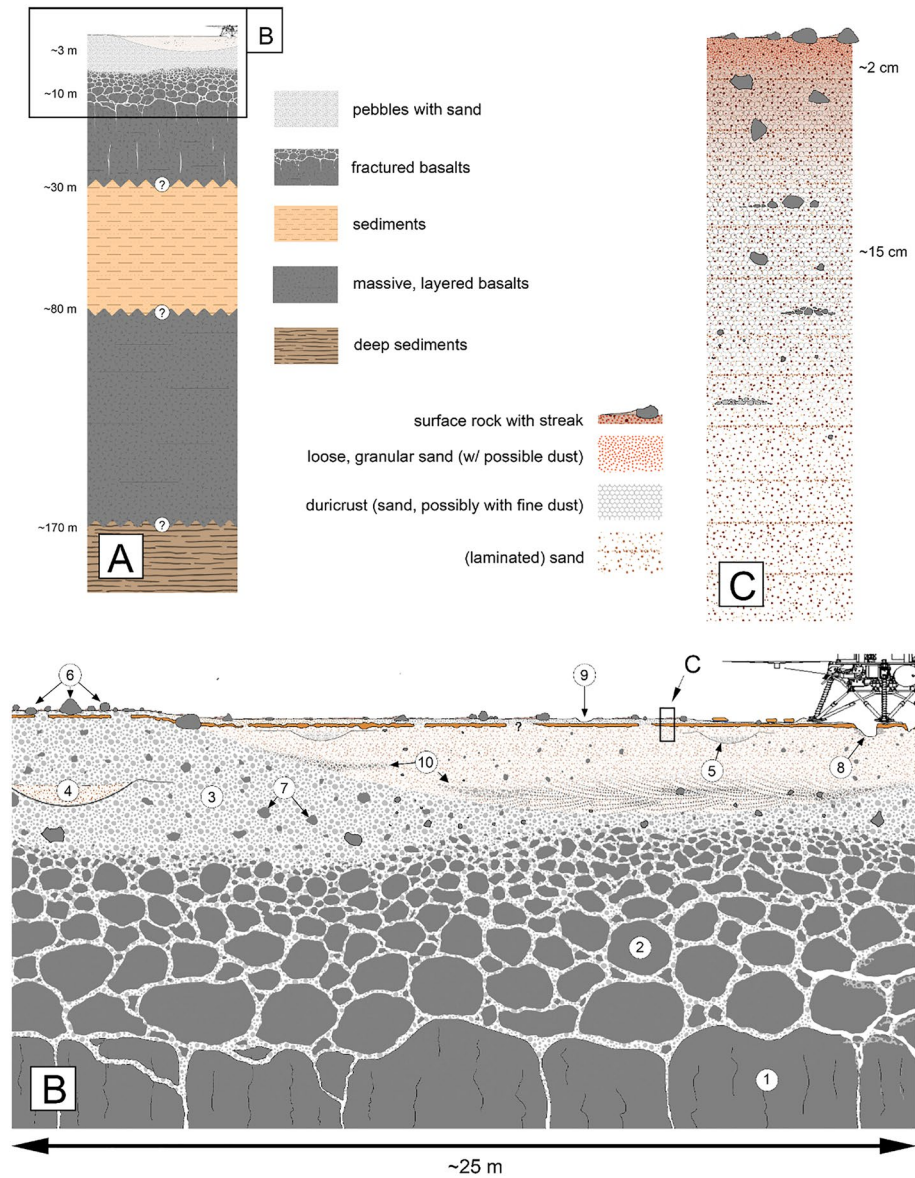


Figure 28. Stratigraphic model beneath the InSight lander illustrating the proposed stratigraphic sequence at the (a) one hundred-meter-scale, (b) meter-scale, and (c) cm-scale. At the one hundred-meter-scale, ~170 m of Early Amazonian to Hesperian-age, regolith-covered, basalts overly Noachian-age clastic materials. The basaltic sequence is interrupted by a ~45 m thick, possible clastic horizon described by Hobiger et al. (2021). At the meter-scale, the stratigraphy consists of the following features: (1) fractured basaltic bedrock, (2) 10–30 m of brecciated/broken basaltic regolith consisting of boulders that grade upwards into finer pebble-sized particles, (3) ~3 m of sand to pebble-dominated regolith, (4) small, sand-filled primary impact craters, (5) sand-filled secondary craters (e.g., *Corintito*), (6) superposing to partially buried pebble to cobble-size clasts of aphanitic basalt, (7) buried pebble to cobble-size basaltic clasts, (8) retrorocket pit exposing a laterally continuous to possibly discontinuous (?) duricrust horizon (orange layer in graphic shows steepest exposure in pit and mole hole), (9) modified/displaced sand, including small, cm-deep depressions and streaks produced by rolling and hopping clasts that were mobilized during landing, (10) buried lenses of slope debris and eolian material that fill *Homestead hollow*. At the cm-scale, the landing site is coated by 1–2 cm of loose, granular sand with a few overlying pebbles and cobbles. Beneath this, the duricrust extends to a depth of up to ~20 cm. The upper several tens of cm of the soil here may contain more dust by volume (indicated by reddish hue in graphic) than in lower horizons. Loose, planar laminated sands likely rest immediately beneath the duricrust. Pebble to cobble-size rocks are buried here as float.

InSight landing site (Sweeney et al., 2018; Warner, Grant, et al., 2020) suggest that *Sunset* crater is Middle to Late Amazonian in age or $\sim 300 \pm 50$ Ma.

7. The degradation rate at *Homestead hollow* slowed at this time to 10^{-4} m/Myr and less than 1 m of crater filling occurred over the next few hundred million years (Grant et al., 2020; Warner, Grant, et al., 2020). Interior eolian bedforms that are today common in fresher impact craters in the region stabilized and flattened in *Homestead hollow*, forming a smooth interior surface.
8. The *Homestead hollow* impact crater is at or near equilibrium with the surrounding terrain throughout the entire Late Amazonian. The last $\sim 10^3$ s of cm of rim deflation and fill occurred at incredibly slow rates ($<10^{-4}$ m/Myr) (Warner, Grant, et al., 2020). Stability of the soil over this time potentially promoted the long-term exchange (order of ~ 100 Myr) of small volumes of atmospheric water vapor within a sand/dust mixture producing a ~ 10 – 20 cm-thick cohesive duricrust. Thermal data from RAD and HP³ do not support significant cohesion of the sandy soil in the upper few tens of centimeters of soil. Small volumes of cement ($\sim 1\%$) have been shown experimentally to drastically increase soil thermal inertia and conductivity, which is not indicated by the thermal observations (Mellon et al., 2008; Piqueux & Christensen, 2009a, 2009b). If a cementing agent is present within the fine sand, it must be in extremely low abundance, forming only thin veneers on the particles. However, if the sandy soil includes a component of low thermal inertia/conductivity dust, the volume of cement could be greater, approaching 0.02% by volume if the entire column is comprised of only cemented dust-sized materials (Grott et al., 2021).

Within the context of the degradation of *Homestead hollow*, dust accumulation may have been volumetrically more important, in terms of its relative abundance to other fill materials, in this last stage of crater modification, thus explaining both the observations of weak cohesion and the thermal data. Over time, fill rate of *Homestead hollow* diminished non-linearly to near zero as the crater degraded to a near equilibrium condition with the surrounding plains (Grant et al., 2020; Sweeney et al., 2018; Warner, Grant, et al., 2020). The supply of airfall dust likely remained constant through this degradation process while the supply of slope-derived materials and eolian sand was finite. Image analysis of the landing region demonstrates that the most recent mobile supply of sand, indicated by dust-covered, meter-scale bedforms in HiRISE images, is spatially limited to the continuous ejecta of relatively fresh impact craters (Sweeney et al., 2018; Warner, Grant, et al., 2020). There are few bedforms on the inter-crater plains or surrounding highly degraded craters like *Homestead hollow*. From observations of craters at different stages of degradation, smaller bedforms in the ejecta organize over time into larger bedforms that become trapped against the crater rim, partially fill the crater, and then disappear altogether. These observations suggest a supply-limited system where the original sand in the ejecta was produced by the impact process itself (Golombek, Charalambous, et al., 2020; McGlynn et al., 2011), either through fragmentation of bedrock and/or excavation of the upper column of sandy regolith. Freshly exhumed sand is quickly transported into the nearest topographic depression that is downwind of its location, which for some of the sand in the ejecta, is the crater itself (Grant et al., 2020, 2022). Once the locally-derived sand is exhausted, crater fill may be supplied, at lower rates, by more distal sand sources. Aside from the sand that surrounds other fresh impacts, an additional sand source for crater filling on the Smooth Terrain has yet to be identified. The lack of bedforms on the inter-crater plains and within and around craters like *Homestead hollow* suggests that the sand here is in aerodynamic equilibrium and is not typically mobile. Change detection analyses within the sand-dominated workspace of *Homestead hollow* indicates only limited motion of sand and granules corresponding with passing pressure vortices (Baker et al., 2021; Charalambous et al., 2021). If dust accumulation can occur within craters at a relatively constant rate, even at low rates that are limited by dust lifting events (e.g., pressure vortices or impacts from saltating sand), the last tens of centimeters of crater fill at *Homestead hollow* may have developed with a higher relative percentage of dust compared to sand due to this change in supply. The small volume of sand and larger ejecta particles that managed to make their way into the remnant *Homestead hollow* at this time may have buffered or shielded some dust-sized particles from lifting. Importantly, dust devil tracks are less common across the landing region (Reiss & Lorenz, 2016) than experienced by the Mars Exploration Rovers and no major dust removal events have occurred at this point in the mission.

9. An occasional impact, including the most recent *Rocky Field* ejecta event (of unknown crater origin) (Grant et al., 2020), as well as limited eolian transport, provided a coating of loose, sand, granules, and pebbles that now caps the surface of *Homestead hollow*. The combined processes produced a 1–2 cm thick surficial layer of loose material that caps the cohesive material.

10. *Corintito* impact occurred within the fill between 0.1 and 1 Ma and 2.5 ± 0.2 Ma (Bloom et al., 2014; Golombek et al., 2014; Hundal et al., 2017), exposing the upper tens of centimeters of the fines-dominated regolith at the edge of *Homestead hollow*. The ongoing dust accumulation coated clasts and the stabilized sand sheets and ripples outside of the hollow, including *Corintito* impact ejecta.
11. InSight landed on the northwestern interior margin of *Homestead hollow* on 26 November 2018. The landing disturbed the soil by lowering the landing site albedo as dust was blown away and produced cm-scale pits, depressions, and holes in the landscape.

7. Conclusion

While the stratigraphic model above and in Figure 28 is specific to this location on Mars, the overall processes and basic stratigraphic architecture are likely similar across all Hesperian to Early Amazonian-age lava plains that have experienced limited surface modification by impact, eolian, and gravity-driven processes. The InSight landing site is morphologically and chronologically similar to other lava plains on Mars, including the Gusev cratered plains, Hesperia Sinai, Solis Plana, and Syrtis Major. Furthermore, *Homestead hollow* itself is morphologically and stratigraphically similar to hollows on other volcanic plains on Mars, such as at Gusev crater (Weitz et al., 2020). In all cases, regolith-covered basalts across Mars have surfaces that are dominated by sand, with low rock abundance and smooth surfaces (Rogers et al., 2018). This terrain type is one of the most areally-extensive (Tanaka et al., 2014) and safest surfaces to land (Golombek et al., 2003b, 2017). In this regard, the stratigraphy at InSight represents the type example of a regolith-covered basaltic surface. The rigorous orbital and in-situ geological investigation at InSight therefore strengthens future predictions for landing operations, particularly if those operations involve work in the shallow subsurface. Pending available power, thermal modeling and seismic data collection by the InSight mission will continue and model results can be tested against these stratigraphic constraints.

Data Availability Statement

HiRISE (McEwen, 2005), CTX (Malin, 2007), THEMIS (Christensen, 2002), and InSight lander-based imagery (Deen et al., 2019) are available through the NASA Planetary Data System (see references). All supporting data, including ArcGIS files, relevant to the Etched Terrain, Hephaestus Fossae, rocky ejecta crater, and lander pit/depression analyses are available through Figshare (see references: Warner, 2022a, 2022b, 2022c, 2022d).

Acknowledgments

Warner's contribution was supported through the NASA Participating Scientist program under Grant 80NSSC18K1624. Grant, Wilson, and Weitz's contributions were supported through the NASA Participating Scientist program under Grant 80NSSC18K1625. A portion of the work was also supported by the InSight Project at the Jet Propulsion Laboratory, California Institute of Technology, under a contract with the National Aeronautics and Space Administration. We are especially grateful to the Mars Reconnaissance Orbiter HiRISE (University of Arizona) and CTX (Malin Space Science Systems) imaging teams for their high-quality data and hard work acquiring InSight-related orbital imagery. We would like to thank Larry Crumpler and Horton Newsom for their thorough and helpful reviews. This is InSight Contribution Number 171.

References

- Arvidson, R. E., Bell, J. F., III, Bellutta, P., Cabrol, N. A., Catalano, J. G., Cohen, J., et al. (2010). Spirit Mars rover mission: Overview and selected results from the northern Home Plate Winter Haven to the side of Scamander crater. *Journal of Geophysical Research*, *115*, E00F03. <https://doi.org/10.1029/2010JE003633>
- Arvidson, R. E., Bellutta, P., Calef, F., Fraeman, A. A., Garvin, J. B., Gasnault, O., et al. (2014). Terrain physical properties derived from orbital data and the first 360 sols of the Mars Science Laboratory Curiosity rover observations in Gale crater. *Journal of Geophysical Research: Planets*, *119*, 1322–1344. <https://doi.org/10.1002/2013JE004605>
- Arvidson, R. E., Gooding, J. L., & Moore, H. J. (1989). The Martian surface as imaged, sampled, and analyzed by the Viking landers. *Reviews of Geophysics*, *27*(1), 39–60. <https://doi.org/10.1029/RG027i001p00039>
- Baker, M., Newman, C., Charalambous, C., Golombek, M., Spiga, A., Banfield, D., et al. (2021). Vortex-dominated aeolian activity at InSight's landing site, Part 2: Local meteorology, transport dynamics, and model analysis. *Journal of Geophysical Research: Planets*, *126*(4), e2020JE006514. <https://doi.org/10.1029/2020JE006514>
- Banerdt, W. B., Smrekar, S. E., Banfield, D., Giardini, D., Golombek, M., Johnson, C. L., et al. (2020). Early results from the InSight mission on Mars. *Nature Geoscience*, *13*(3), 183–189. <https://doi.org/10.1038/s41561-020-0544-y>
- Banin, A. (1992). In H. H. Kieffer, B. M. Jakosky, C. W. Snyder, & M. S. Matthews (Eds.), *Mars* (pp. 594–625). University of Arizona Press.
- Bart, G. D., & Melosh, H. J. (2010). Distributions of boulders ejected from lunar craters. *Icarus*, *209*(2), 337–357. <https://doi.org/10.1016/j.icarus.2010.05.023>
- Bart, G. D., Nickerson, R. D., Lawder, M. T., & Melosh, H. J. (2011). Global survey of lunar regolith depths from LROC images. *Icarus*, *215*(2), 485–490. <https://doi.org/10.1016/j.icarus.2011.07.017>
- Binder, A. B., Arvidson, R. E., Guinness, E. A., Jones, K. L., Morris, E. C., Mutch, T. A., et al. (1977). The geology of the Viking lander 1 site. *Journal of Geophysical Research*, *82*(28), 4439–4451. <https://doi.org/10.1029/J082i028p04439>
- Bloom, C., Golombek, M., Warner, N., & Wigton, N. (2014). *Size frequency distribution and ejection velocity of Corinto crater secondaries in Elysium Planitia*. In Eighth International Conference on Mars, Pasadena, CA, July 14–18. Lunar and Planetary Institute. Abstract #1289.
- Brinkman, N., Schmelzbach, C., Sollberger, D., van Driel, M., ten Pierick, J., Robertsson, J. O. A., et al. (2019). The first active-seismic experiment on Mars to characterize the shallow subsurface structure at the InSight landing site. *SEG Technical Program Expanded Abstracts*, 4756–4760. <https://doi.org/10.1190/segam2019-3215661.1>

- Cabrol, N. A., Farmer, J. D., Grin, E. A., Richter, L., Soderblom, L., Li, R., et al. (2006). Aqueous processes at Gusev crater inferred from physical properties of rocks and soils along the Spirit traverse. *Journal of Geophysical Research*, *111*(E2), EOZS20. <https://doi.org/10.1029/2005JE002490>
- Charalambous, C. (2014). *On the evolution of particle fragmentation with applications to planetary surfaces*. PhD Thesis. Imperial College London.
- Charalambous, C., Golombek, M., Pike, T., Warner, N. H., Weitz, C., Ansan, V., et al. (2019). *Rock distributions at the InSight landing site and implications based on fragmentation theory*. In 50th Lunar and Planetary Science. Lunar and Planetary Institute. Abstract #2812.
- Charalambous, C., McClean, J. B., Baker, M., Pike, W. T., Golombek, M., Lemmon, M., et al. (2021). Vortex-dominated aeolian activity at InSight's landing site, Part 1: Multi-instrument observations, analysis and implications. *Journal of Geophysical Research: Planets*, *126*(6), e2020JE006757. <https://doi.org/10.1029/2020JE006757>
- Christensen, P. R. (2002). *ODYSSSEY THEMIS IR BTR V1.0, ODY-M-THM-3-IRBTR-V1.0, Mars Odyssey THEMIS standard products*. NASA Planetary Data Systems.
- Christensen, P. R., Bandfield, J. L., Hamilton, V. E., Ruff, S. W., Kieffer, H. H., Titus, T. N., et al. (2001). Mars global surveyor thermal emission spectrometer experiment: Investigation description and surface science results. *Journal of Geophysical Research*, *106*(E10), 23823–23871. <https://doi.org/10.1029/2000JE001370>
- Christensen, P. R., Jakosky, B. M., Kieffer, H. H., Malin, M. C., McSweeney, H. Y., Jr., Neelson, K., et al. (2004). The thermal emission imaging system (THEMIS) for the Mars 2001 Odyssey mission. *Space Science Review*, *110*, 85–130. https://doi.org/10.1007/978-0-306-48600-5_3
- Christensen, P. R., & Moore, H. J. (1992). In H. H. Kieffer, B. M. Jakosky, C. W. Snyder, & M. S. Matthews (Eds.), *Mars* (Vol. 686–727). University of Arizona Press.
- Clegg, R. N., Jolliff, B. L., Robinson, M. S., Hapke, B. W., & Plescia, J. B. (2014). Effects of rocket exhaust on lunar soil reflectance properties. *Icarus*, *227*, 176–194. <https://doi.org/10.1016/j.icarus.2013.09.013>
- Craddock, R. A., & Golombek, M. P. (2016). Characteristics of terrestrial basaltic rock populations: Implications for Mars lander and rover science and safety. *Icarus*, *274*, 50–72. <https://doi.org/10.1016/j.icarus.2016.02.042>
- Daubar, I. J., Dundas, C., Byrne, S., Geissler, P., Bart, G., McEwen, A., et al. (2016). Changes in blast zone albedo patterns around new Martian impact craters. *Icarus*, *267*, 86–105. <https://doi.org/10.1016/j.icarus.2015.11.032>
- Daubar, I. J., Lognonne, P., Teanby, N. A., Collins, G. S., Clinton, J., Stahler, S., et al. (2020). A new crater near InSight: Implications for seismic impact detectability on Mars. *Journal of Geophysical Research: Planets*, *125*(8), e2020JE006382. <https://doi.org/10.1029/2020JE006382>
- Deen, R., Abarca, H., Zamani, P., & Maki, J. (2019). *InSight cameras bundle*. NASA Planetary Data System. <https://doi.org/10.17189/1510484>
- Delage, P., Karakostas, F., Dhemaied, A., Belmokhtar, M., Lognonné, P., Golombek, M., et al. (2017). An investigation of the mechanical properties of some Martian regolith simulants with respect to the surface properties at the InSight mission landing site. *Space Science Review*, *211*(1–4), 191–213. <https://doi.org/10.1007/s11214-017-0339-7>
- Ehlmann, B. L., Edgett, K. S., Sutter, B., Achilles, C. N., Litvak, M. L., Lapotre, M. G. A., et al. (2017). Chemistry, mineralogy, and grain properties at Namib and high dunes, Bagnold dune field, Gale crater, Mars: A synthesis of Curiosity rover observations. *Journal of Geophysical Research: Planets*, *122*(12), 2510–2543. <https://doi.org/10.1002/2017JE005267>
- Fayon, L., Knapmeyer-Endrun, B., Lognonné, P., Bierwirth, M., Kramer, A., Delage, P., et al. (2018). A numerical model of the SEIS leveling system transfer matrix and resonances: Application to SEIS rotational seismology and dynamic ground interaction. *Space Science Reviews*, *214*(8), 119. <https://doi.org/10.1007/s11214-018-0555-9>
- Ferguson, R. L., Kirk, R. L., Cushing, G., Galuzska, D. M., Golombek, M. P., Hare, T. M., et al. (2017). Analysis of local slopes at the InSight landing site on Mars. *Space Science Reviews*, *211*(1–4), 109–133. <https://doi.org/10.1007/s11214-016-0292-x>
- Folkner, W. M., Dehant, V., Le Maistre, S., Yseboodt, M., Rivoldini, A., Van Hoolst, T., et al. (2018). The rotation and interior structure experiment on the InSight mission to Mars. *Space Science Reviews*, *214*(5), 100. <https://doi.org/10.1007/s11214-018-0530-5>
- Garvin, J. B., Sakimoto, S. E. H., & Frawley, J. J. (2003). Craters on Mars: Global geometric properties from gridded MOLA topography. In *6th International Conference on Mars*. Lunar and Planetary Institute. Abstract #3277.
- Golombek, M., Bloom, C., Wigton, N., & Warner, N. (2014). Constraints on the age of Corinto crater from mapping secondaries in Elysium Planitia on Mars. In *45th Lunar and Planetary Science*. Lunar and Planetary Institute. Abstract #1470.
- Golombek, M., Charalambous, C., Pike, W. T., & Sullivan, R. (2020). The origin of sand and dust on Mars: Evidence from the InSight landing site (expanded abstract). In *51st Lunar and Planetary Science*. Lunar and Planetary Institute. Abstract #2744.
- Golombek, M., Grott, M., Kargl, G., Andrade, J., Marshall, J., Warner, N., et al. (2018). Geology and physical properties investigations by the InSight Lander. *Space Science Review*, *214*, 84. <https://doi.org/10.1007/s11214-018-0512-7>
- Golombek, M., Kass, D., Williams, N., Warner, N., Daubar, I., Piqueux, S., et al. (2020). Assessment of InSight landing site predictions. *Journal of Geophysical Research: Planets*, *125*. <https://doi.org/10.1029/2020JE006502>
- Golombek, M., Kipp, D., Warner, N., Daubar, I. J., Ferguson, R., Kirk, R. L., et al. (2017). Selection of the InSight landing site. *Space Science Review*, *211*, 5–95. <https://doi.org/10.1007/s11214-016-0321-9>
- Golombek, M., Williams, N., Warner, N. H., Parker, T., Williams, M. G., Daubar, I., et al. (2020). Location and setting of the Mars InSight lander, instruments, and landing site. *Earth and Space Science*, *7*, e2020EA001248. <https://doi.org/10.1029/2020EA001248>
- Golombek, M. P., Crumpler, L. S., Grant, J. A., Greeley, R., Cabrol, N. A., Parker, T. J., et al. (2006). Geology of the Gusev cratered plains from the Spirit rover traverse. *Journal of Geophysical Research*, *111*, E02S07. <https://doi.org/10.1029/2005JE002503>
- Golombek, M. P., Grant, J. A., Parker, T. J., Kass, D. M., Crisp, J. A., Squyres, S. W., et al. (2003). Selection of the Mars exploration rover landing sites. *Journal of Geophysical Research*, *108*(E12), 8072. <https://doi.org/10.1029/2003JE002074>
- Golombek, M. P., Haldemann, A. F. C., Forsberg-Taylor, N. K., DiMaggio, E. N., Schroeder, R. D., Jakosky, B. M., et al. (2003). Rock size-frequency distributions on Mars and implications for MER landing safety and operations. *Journal of Geophysical Research*, *108*(E12), 8086. <https://doi.org/10.1029/2002JE002035>
- Golombek, M. P., Haldemann, A. F. C., Simpson, R. A., Ferguson, R. L., Putzig, N. E., Arvidson, R. E., et al. (2008). In J. F. Bell III (Ed.), *The Martian surface: Composition, mineralogy and physical properties* (pp. 468–497). Cambridge University Press.
- Golombek, M. P., & Phillips, R. J. (2010). In T. R. Watters, & R. A. Schultz (Eds.), *Planetary tectonics* (pp. 183–232). Cambridge University Press.
- Golombek, M. P., Trussell, A., Williams, N., Charalambous, C., Abarca, H., Warner, N. H., et al. (2021). Rock size-frequency distributions of the InSight landing site, Mars. *Earth and Space Science*. <https://doi.org/10.1002/essoar.10507665.1>
- Golombek, M. P., Warner, N. H., Grant, J. A., Hauber, E., Ansan, V., Weitz, C. M., et al. (2020). Geology of the InSight landing site on Mars. *Nature Communications*, *11*. <https://doi.org/10.1038/s41467-020-14679-1>
- Grant, J. A., Arvidson, R. E., Crumpler, L. S., Golombek, M. P., Hahn, B., Haldemann, A. F. C., et al. (2006). Crater gradation in Gusev crater and Meridiani Planum, Mars. *Journal of Geophysical Research*, *111*. <https://doi.org/10.1029/2005JE002465>

- Grant, J. A., Warner, N. H., Weitz, C. M., Golombek, M. P., Wilson, S. A., Baker, M., et al. (2020). Degradation of *Homestead hollow* at the InSight landing site based on the distribution and properties of local deposits. *Journal of Geophysical Research: Planets*, *125*. <https://doi.org/10.1029/2019JE006350>
- Grant, J. A., & Wilson, S. A. (2012). A possible synoptic source of water for alluvial fan formation in southern Margaritifer Terra, Mars. *Planetary and Space Science*, *72*, 44–52. <https://doi.org/10.1016/j.pss.2012.05.020>
- Grant, J. A., & Wilson, S. A. (2019). Evidence for late alluvial activity in Gale crater, Mars. *Geophysical Research Letters*, *46*, 7287–7294. <https://doi.org/10.1029/2019GL083444>
- Grant, J. A., Wilson, S. A., Golombek, M., Trussell, A., Warner, N. H., Williams, N., et al. (2022). Degradation at the InSight landing site, Homestead hollow, Mars: Constraints from rock heights and shapes. *Earth and Space Science*, *9*(2). <https://doi.org/10.1029/2021EA001953>
- Grant, J. A., Wilson, S. A., Mangold, M., Calef, F., III, & Grotzinger, J. (2014). The timing of alluvial activity in Gale crater, Mars. *Geophysical Research Letters*, *41*, 1142–1148. <https://doi.org/10.1002/2013GL058909>
- Greeley, R., & Iversen, J. D. (1987). Measurements of wind friction speeds over lava surfaces and assessment of sediment transport. *Geophysical Research Letters*, *14*(9), 925–928. <https://doi.org/10.1029/GL014i009p00925>
- Greeley, R., Leach, R., White, B., Iversen, J., & Pollack, J. (1980). Threshold windspeeds for sand on Mars: Wind tunnel simulations. *Geophysical Research Letters*, *7*(2), 121–124. <https://doi.org/10.1029/GL007i002p00121>
- Grieve, R. A. F., Robertson, P. B., & Dence, M. R. (1981). In P. H. Schultz & R. B. Merrill (Eds.), *Constraints on the formation of ring impact structures, based on terrestrial data*, in *Multi-Ring Basins* (pp. 37–57). Pergamon Press.
- Grott, M., Spohn, T., Knollenberg, J., Krause, C., Hudson, T. L., Piqueux, S., et al. (2021). Thermal conductivity of the martian soil at the InSight landing site from HP³ active heating experiments. *Journal of Geophysical Research: Planets*, *126*, e2021JE006861. <https://doi.org/10.1029/2021JE006861>
- Hamzah, M. B. A.-H., & Baghabra Al-Amoudi, O. S. (2018). A review on the angle of repose of granular materials. *Powder Technology*, *330*, 397–417. <https://doi.org/10.1016/j.powtec.2018.02.003>
- Hartmann, W. K. (1984). Does crater “saturation equilibrium” occur in the Solar System? *Icarus*, *60*(1), 56–74. [https://doi.org/10.1016/0019-1035\(84\)90138-6](https://doi.org/10.1016/0019-1035(84)90138-6)
- Hartmann, W. K., Anguita, J., de la Casa, M., Berman, D. C., & Ryan, E. V. (2001). Martian cratering 7: The role of impact gardening. *Icarus*, *149*, 37–53. <https://doi.org/10.1006/icar.2000.6532>
- Hartmann, W. K., & Neukum, G. (2001). Cratering chronology and the evolution of Mars. *Space Science Reviews*, *96*, 165–194. <https://doi.org/10.1023/A:1011945222010>
- Haskin, L. A., Wang, A., Jolliff, B. L., McSween, H. Y., Clark, B. C., Des Marais, D. J., et al. (2005). Water alteration of rocks and soils from the Spirit rover site, Gusev crater, Mars. *Nature*, *436*, 66–69. <https://doi.org/10.1038/nature03640>
- Herkenhoff, K. E., Golombek, M. P., Guinness, E. A., Johnson, J. B., Kusack, A., Richter, L., et al. (2008). In J. F. Bell III (Ed.), *The Martian surface: Composition, mineralogy and Physical Properties* (pp. 451–467). Cambridge University Press.
- Hermalyn, B., & Schultz, P. H. (2011). Time-resolved studies of hypervelocity vertical impacts into porous particulate targets: Effects of projectile density on early-time coupling and crater growth. *Icarus*, *216*(1), 269–279. <https://doi.org/10.1016/j.icarus.2011.09.008>
- Hobiger, M., Hallo, M., Schmelzbach, C., Stähler, S., Fäh, D., Giardini, D., et al. (2021). The shallow structure of Mars from inversion of high-frequency ambient noise Rayleigh wave ellipticity at the InSight landing site. *Nature Communications*, *12*. <https://doi.org/10.1038/s41467-021-26957-7>
- Holstein-Rathlou, C., Gunnlaugsson, H. P., Merrison, J. P., Bean, K. M., Cantor, B. A., Davis, J. A., et al. (2010). Winds at the Phoenix landing site. *Journal of Geophysical Research*, *115*, E00E18. <https://doi.org/10.1029/2009JE003411>
- Hudson, T. L., Deen, R., Marteau, E., Golombek, M., Hurst, K., Spohn, T., et al. (2020). InSight HP³ mole near-surface motion and subsurface implications (expanded abstract). In *51st Lunar and Planetary Science*. Lunar and Planetary Institute. Abstract #1217
- Hundal, C. B., Golombek, M. P., & Daubar, I. J. (2017). Chronology of fresh rayed craters in Elysium Planitia, Mars. In *48th Lunar and planetary science*. Lunar and Planetary Institute. Abstract #1726.
- Hurowitz, J. A., McLennan, N., Tosca, N. J., Arvidson, R. E., Michalski, J. R., Ming, D. W., et al. (2006). In situ and experimental evidence for acidic weathering of rocks and soils on Mars. *Journal of Geophysical Research*, *111*, E02S19. <https://doi.org/10.1029/2005JE002515>
- Ivanov, B. A. (2001). Mars/Moon cratering rate ratio estimates. *Space Science Reviews*, *96*, 87–104. <https://doi.org/10.1023/A:1011941121102>
- Iversen, J. D., Greeley, R., & Pollack, J. B. (1976). Windblown dust on Earth, Mars and Venus. *Journal of Atmospheric Science*, *33*(12), 2425–2429. [https://doi.org/10.1175/1520-0469\(1976\)033<2425:WDOEMA>2.0.CO;2](https://doi.org/10.1175/1520-0469(1976)033<2425:WDOEMA>2.0.CO;2)
- Jakosky, B. M., & Christensen, P. R. (1986). Global duricrust on Mars: Analysis of remote-sensing data. *Journal of Geophysical Research*, *91*(B3), 3547–3559. <https://doi.org/10.1029/JB091iB03p03547>
- Jiang, M., Xi, B., Arroyo, M., & Rodriguez-Dono, A. (2017). DEM simulation of soil-tool interaction under extraterrestrial environmental effects. *Journal of Terramechanics*, *71*, 1–13. <https://doi.org/10.1016/j.jterra.2017.01.002>
- Johnson, J. R., Bell, J., Bender, S., Blaney, D., Cloutis, E., DeFlores, L., et al. (2015). ChemCam passive reflectance spectroscopy of surface materials at the Curiosity landing site, Mars. *Icarus*, *249*, 74–92. <https://doi.org/10.1016/j.icarus.2014.02.028>
- Jones, K. L., Arvidson, R. E., Guinness, E. A., Bragg, S. L., Wall, S. D., Carlston, C. E., & Pidek, D. G. (1979). One Mars year: Viking lander imaging observations. *Science*, *204*(4395), 799–806. <https://doi.org/10.1126/science.204.4395.799>
- Kedar, S., Andrade, J., Banerdt, B., Delage, P., Golombek, M., Grott, M., et al. (2017). Analysis of regolith properties using seismic signals generated by InSight’s HP³ penetrator. *Space Science Reviews*, *211*, 315–337. <https://doi.org/10.1007/s11214-017-0391-3>
- Kenda, B., Drilleau, M., Garcia, R. F., Kawamura, T., Murdoch, N., Compaire, N., et al. (2020). Subsurface structure at the InSight landing site from compliance measurements by seismic and meteorological experiments. *Journal of Geophysical Research: Planets*, *125*, e2020JE006387. <https://doi.org/10.1029/2020JE006387>
- Kenda, B., Lognonné, P., Spiga, A., Kawamura, T., Kedar, S., Banerdt, W. B., et al. (2017). Modeling of ground deformation and shallow surface waves generated by Martian dust devils and perspectives for near-surface structure inversion. *Space Science Reviews*, *211*(1), 501–524. <https://doi.org/10.1007/s11214-017-0378-0>
- Kite, E. S., Sneed, D., Mayer, D. P., & Wilson, S. A. (2017). Persistent or repeated surface habitability on Mars during the late Hesperian—Amazonian. *Geophysical Research Letters*, *16*, 3991–3999. <https://doi.org/10.1002/2017GL072660>
- Knapmeyer-Endrun, B., Golombek, M. P., & Ohnberger, M. (2017). Rayleigh wave ellipticity modeling and inversion for shallow structure at the proposed InSight landing site in Elysium Planitia, Mars. *Space Science Reviews*, *211*, 339–382. <https://doi.org/10.1007/s11214-016-0300-1>
- Knapmeyer-Endrun, B., Murdoch, N., Kenda, B., Golombek, M. P., Knapmeyer, M., Witte, L., et al. (2018). Influence of body waves, instrumentation resonances, and prior assumptions on Rayleigh wave ellipticity inversion for shallow structure at the InSight landing site. *Space Science Reviews*, *214*, 94. <https://doi.org/10.1007/s11214-018-0529-y>

- Kumar, S. P., Prasanna Lakshmi, K. J., Krishna, N., Menon, R., Sruthi, U., Keerthi, V., et al. (2014). Impact fragmentation of Lunar Crater, India: Implications for impact cratering processes in basalt. *Journal of Geophysical Research: Planets*, *119*, 2029–2059. <https://doi.org/10.1002/2013JE004543>
- Lognonné, P., Banerdt, W. B., Pike, W. T., Giardini, D., Christensen, U., Garcia, R. F., et al. (2020). Constraints on the shallow elastic and anelastic structure of Mars from InSight seismic data. *Nature Geoscience*, *13*, 213–220. <https://doi.org/10.1038/s41561-020-0536-y>
- Lorenz, R. D. (2016). Lander rocket exhaust effects on Europa regolith nitrogen assays. *Planetary and Space Science*, *127*, 91–94. <https://doi.org/10.1016/j.pss.2016.04.008>
- Maki, J. N., Golombek, M., Deen, R., Abarca, H., Sorice, C., Goodsall, T., et al. (2018). The color cameras on the InSight lander. *Space Science Reviews*, *214*(6), 105. <https://doi.org/10.1007/s11214-018-0536-z>
- Malin, M. (2007). MRO Context Camera Experiment Data Record Level 0 V1.0, MRO-M-CTX-2-EDR-L0-V1.0, NASA Planetary Data System. <https://doi.org/10.17189/1520266>
- Malin, M. C., Bell, J. F., Cantor, B. A., Caplinger, M. A., Calvin, W. M., Clancy, R. T., et al. (2007). Context camera investigation on board the Mars reconnaissance orbiter. *Journal of Geophysical Research*, *112*, E05S04. <https://doi.org/10.1029/2006JE002808>
- Marteau, E., Golombek, M., Vrettos, C., Garvin, J. B., & Williams, N. R. (2021). Soil mechanical properties at the InSight landing site, Mars (expanded abstract). In *52nd Lunar and Planetary Science*. Lunar and Planetary Institute. Abstract #2067.
- McEwen, A. S. (2005). MRO Mars high resolution image science experiment. EDR V1.0. [Data set]. <https://doi.org/10.17189/1520179>
- McEwen, A. S., Eliason, E. M., Bergstrom, J. W., Bridges, N. T., Hansen, C. J., Delamere, W. A., et al. (2007). Mars reconnaissance orbiter's high resolution imaging science experiment (HiRISE). *Journal of Geophysical Research*, *112*, E05S02. <https://doi.org/10.1029/2005JE002605>
- McGlynn, I. O., Fedo, C. M., & McSween, H. Y., Jr. (2011). Origin of basaltic soils at Gusev crater, Mars, by aeolian modification of impact-generated sediment. *Journal of Geophysical Research*, *116*, E00F22. <https://doi.org/10.1029/2010JE003712>
- Mehta, M., Renno, N. O., Marshall, J., Grover, M. R., Sengupta, A., Rusche, N. A., et al. (2011). Explosive erosion during the Phoenix landing exposes subsurface water on Mars. *Icarus*, *211*(1), 172–194. <https://doi.org/10.1016/j.icarus.2010.10.003>
- Mehta, M., Sengupta, A., Rennó, N. O., Van Norman, J. W., Huseman, P. G., Gulick, D. S., & Pokora, M. (2013). Thruster plume surface interactions: Applications for spacecraft landings on planetary bodies. *AIAA Journal*, *51*(12), 2800–2818. <https://doi.org/10.2514/1.J052408>
- Mellon, M. T., Fergason, R. L., & Putzig, N. E. (2008). The thermal inertia of the surface of Mars. In J. F. Bell (Ed.), *The Martian surface: Composition, mineralogy, and physical properties* (pp. 399–327). Cambridge University Press.
- Melosh, H. J. (1989). *Impact craters: A geologic process* (pp. 76–85). Oxford University Press.
- Michael, G. G. (2013). Planetary surface dating from crater size-frequency distribution measurements: Multiple resurfacing episodes and differential isochron fitting. *Icarus*, *226*, 885–890. <https://doi.org/10.1016/j.icarus.2013.07.004>
- Moore, H. J., Bickler, D. B., Crisp, J. A., Eisen, H. J., Gensler, J. A., Haldemann, A. F. C., et al. (1999). Soil-like deposits observed by Sojourner, the Pathfinder rover. *Journal of Geophysical Research*, *104*(E4), 8729–8746. <https://doi.org/10.1029/1998JE900005>
- Moore, H. J., Hutton, R. E., Clow, G. D., & Spitzer, C. R. (1987). Physical properties of the surface materials of the Viking landing sites on Mars. *U. S. Geological Survey Professional Paper*, *1389*, 222.
- Morgan, P., Grott, M., Knapmeyer-Endrun, B., Golombek, M., Delage, P., Lognonné, P., et al. (2018). A pre-landing assessment of regolith properties at the InSight landing site. *Space Science Reviews*, *214*(6), 104. <https://doi.org/10.1007/s11214-018-0537-y>
- Mueller, K., & Golombek, M. P. (2004). Compressional structures on Mars. *Annual Review of Earth and Planetary Sciences*, *32*(1), 435–464. <https://doi.org/10.1146/annurev.earth.32.101802.120553>
- Mueller, N., Knollenberg, J., Grott, M., Kopp, E., Walter, I., Krause, C., et al. (2020). Calibration of the HP3 radiometer on InSight. *Earth and Space Science*, *7*(5), e2020EA001086. <https://doi.org/10.1029/2020EA001086>
- Mueller, N., Piqueux, S., Lemmon, M., Maki, J., Lorenz, R. D., Grott, M., et al. (2021). Near surface properties of martian regolith derived from InSight HP³-RAD temperature observations during Phobos transits. *Geophysical Research Letters*, *48*, e2021GL093542. <https://doi.org/10.1029/2021GL093542>
- Murdoch, N., Spiga, A., Lorenz, R., Garcia, R. F., Perrin, C., Widmer-Schmidrig, R., et al. (2021). Constraining Martian regolith and vortex parameters from combined seismic and meteorological measurements. *Journal of Geophysical Research: Planets*, *126*, e2020JE006410. <https://doi.org/10.1029/2020JE006410>
- Mutch, T. A., Arvidson, R. E., Binder, A. B., Guinness, E. A., & Morris, E. C. (1977). The geology of the Viking lander 2 site. *Journal of Geophysical Research*, *82*(28), 4452–4467. <https://doi.org/10.1029/JS082i028p04452>
- Ondera, K. (2022). *Subsurface structure of the moon and mars deduced from 3D seismic wave propagation simulation and analysis of apollo and insight seismic data*. (PhD dissertation). Université de Paris. thesis.
- Pan, L., Quantin-Nataf, Q., Tauzin, B., Michaut, C., Golombek, M. P., Lognonne, P., et al. (2020). Crust stratigraphy and heterogeneities of the first kilometers at the dichotomy boundary in Western Elysium Planitia and implications for InSight lander. *Icarus*, *338*, 113511. <https://doi.org/10.1016/j.icarus.2019.113511>
- Pike, R. J. (1974). Depth/diameter relations of fresh lunar craters: Revision from spacecraft data. *Geophysical Research Letters*, *1*, 291–294. <https://doi.org/10.1029/GL001i007p00291>
- Piqueux, S., & Christensen, P. (2009a). A model of thermal conductivity for planetary soils 1: Theory for unconsolidated soils. *Journal of Geophysical Research*, *114*, E09005. <https://doi.org/10.1029/2008JE003308>
- Piqueux, S., & Christensen, P. (2009b). A model of thermal conductivity for planetary soils 2: Theory for cemented soils. *Journal of Geophysical Research*, *114*, E09006. <https://doi.org/10.1029/2008JE003309>
- Piqueux, S., Müller, N., Grott, M., Siegler, M., Millour, E., Forget, F., et al. (2021). Soil thermophysical properties near the InSight lander derived from 50 sols of radiometer measurements. *Journal of Geophysical Research: Planets*, *126*, e2021JE006859. <https://doi.org/10.1029/2021JE006859>
- Plemmons, D. H., Mehta, M., Clark, B. C., Kounaves, S. P., Peach, L. L., Jr., Renno, N. O., et al. (2008). Effects of the Phoenix Lander descent thruster plume on the Martian surface. *Journal of Geophysical Research*, *113*, E00A11. <https://doi.org/10.1029/2007JE003059>
- Putzig, N. E., & Mellon, M. T. (2007). Apparent thermal inertia and the surface heterogeneity of Mars. *Icarus*, *191*(1), 68–94. <https://doi.org/10.1016/j.icarus.2007.05.013>
- Quaide, W. L., & Oberbeck, V. R. (1968). Thickness determinations of the lunar surface layer from lunar impact craters. *Journal of Geophysical Research*, *73*, 5247–5270. <https://doi.org/10.1029/JB073i016p05247>
- Reiss, D., & Lorenz, R. D. (2016). Dust devil track survey at Elysium Planitia, Mars: Implications for the InSight landing sites. *Icarus*, *266*, 315–330. <https://doi.org/10.1016/j.icarus.2015.11.012>
- Rogers, A. D., Warner, N. H., Golombek, M. P., Head, J. W., III, & Cowart, J. C. (2018). Areal extensive surface bedrock exposures on Mars: Many are clastic rocks, not lavas. *Geophysical Research Letters*, *45*, 1767–1777. <https://doi.org/10.1002/2018GL077030>

- Schultz, P. H., & Anderson, R. R. (1996). *Asymmetry of the Manson Impact Structure: Evidence for Impact Angle and Direction* (Vol. 302, pp. 397–417). Special Paper Geological Society of America. <https://doi.org/10.1130/SPE302>
- Senft, L. E., & Stewart, S. T. (2007). Modeling impact cratering in layered surfaces. *Journal of Geophysical Research*, *112*, E11002. <https://doi.org/10.1029/2007JE002894>
- Shaw, A., Arvidson, R. E., Bonitz, R., Carsten, J., Keller, H. U., Lemmon, M. T., et al. (2009). Phoenix soil physical properties investigation. *Journal of Geophysical Research*, *114*, E00E05. <https://doi.org/10.1029/2009JE003455>
- Spohn, T., Grott, M., Smrekar, S. E., Knollenberg, J., Hudson, T. L., Krause, C., et al. (2018). The heat flow and physical properties package (HP³) for the InSight mission. *Space Science Review*, *214*, 96. <https://doi.org/10.1007/s11214-018-0531-4>
- Stoffler, D., Gault, D. E., Wedekind, J., & Polkowski, G. (1975). Experimental hypervelocity impact into quartz sand: Distribution and shock metamorphism of ejecta. *Journal of Geophysical Research*, *80*, 4062–4077. <https://doi.org/10.1029/JB080i029p04062>
- Sullivan, R., Arvidson, R., Bell, J. F., III, Gellert, R., Golombek, M., Greeley, R., et al. (2008). Wind-driven particle mobility on Mars: Insights from MER observations at “El Dorado” and surroundings at Gusev crater. *Journal of Geophysical Research*, *113*, E06S07. <https://doi.org/10.1029/2008JE003101>
- Sullivan, R., Banfield, D., Bell, J. F., III, Calvin, W., Fike, D., Golombek, M., et al. (2005). Aeolian processes at the Mars exploration rover Meridiani Planum landing site. *Nature*, *436*, 58–61. <https://doi.org/10.1038/nature03641>
- Sweeney, J., Warner, N. H., Ganti, V., Golombek, M. P., Lamb, M. P., Fergason, R., & Kirk, R. (2018). Degradation of 100-m-scale impact craters at the InSight landing site on Mars with implications for surface processes and erosion rates in the Hesperian and Amazonian. *Journal of Geophysical Research: Planets*, *123*, 2732–2759. <https://doi.org/10.1029/2018JE005618>
- Tanaka, K. L., Skinner, J. A., Jr., Dohm, J. M., Irwin, R. P., III, Kolb, E. J., Fortezzo, C. M., et al. (2014). *Geologic map of Mars* (Vol. 3292). U.S. Geological Survey Science Investigations Map. <https://doi.org/10.3133/sim3292>
- Thompson, T. W., Roberts, W. J., Hartmann, W. K., Shorthill, R. W., & Zisk, S. H. (1979). Blocky craters: Implications about the lunar megaregolith. *The Moon and the Planets*, *21*(3), 319–342. <https://doi.org/10.1007/bf00897360>
- Trebi-Ollennu, A., Kim, W., Ali, K., Khan, O., Sorice, C., Bailey, P., et al. (2018). InSight Mars lander robotics instrument deployment system. *Space Science Reviews*, *214*(93). <https://doi.org/10.1007/s11214-018-0520-7>
- Warner, N. (2022d). *DEM data from under the lander*. figshare. [Dataset]. <https://doi.org/10.6084/m9.figshare.18583799.v1>
- Warner, N. (2022a). *Etched terrain analysis*. figshare. [Dataset]. <https://doi.org/10.6084/m9.figshare.18551195.v1>
- Warner, N. (2022b). *Hephaestus DEM analysis and Crater stats*. figshare. [Dataset]. <https://doi.org/10.6084/m9.figshare.18551408.v1>
- Warner, N. (2022c). *Rocky Ejecta Craters analysis*. figshare. [Dataset]. <https://doi.org/10.6084/m9.figshare.18583442.v1>
- Warner, N. H., Golombek, M. P., Sweeney, J., Fergason, R., Kirk, R., & Schwartz, C. (2017). Near surface stratigraphy and regolith production in southwestern Elysium Planitia, Mars: Implications for Hesperian–Amazonian terrains and the InSight lander mission. *Space Science Review*, *211*, 147–190. <https://doi.org/10.1007/s11214-017-0352-x>
- Warner, N. H., Grant, J. A., Wilson, S. A., Golombek, M. P., DeMott, A., Charalambous, C., et al. (2020). An impact crater origin for the InSight landing site at Homestead Hollow, Mars: Implications for near surface stratigraphy, surface processes and erosion rates. *Journal of Geophysical Research: Planets*, *125*. <https://doi.org/10.1029/2019JE006333>
- Warner, N. H., Schuyler, A. J., Rogers, A. D., Golombek, M. P., Grant, J., Wilson, S., et al. (2020). Crater morphometry on the mafic floor unit at Jezero Crater, Mars: Comparisons to a known basaltic lava plain at the InSight landing site. *Geophysical Research Letters*, *47*(17). <https://doi.org/10.1029/2020GL089607>
- Weitz, C. M., Grant, J. A., Golombek, M. P., Warner, N. H., Hauber, E., Ansan, V., et al. (2020). Comparison of InSight Homestead hollow to hollows at the Spirit landing site. *Journal of Geophysical Research: Planets*, *125*. <https://doi.org/10.1029/2020JE006435>
- Weitz, C. M., Sullivan, R. J., Lapotre, M. G., Rowland, S. K., Grant, J. A., Baker, M., & Yingst, R. A. (2018). Sand grain sizes and shapes in eolian bedforms at Gale Crater, Mars. *Geophysical Research Letters*(18), 9471–9479. <https://doi.org/10.1029/2018GL078972>
- Wentworth, C. K. (1933). Fundamental limits to the sizes of elastic grains. *Science*, *77*(2009), 633–634. <https://doi.org/10.1126/science.77.2009.633>
- Wilson, S. A., Warner, N. H., Grant, J. A., Golombek, M. P., DeMott, A., Kopp, M., et al. (2019). Crater retention ages at the InSight landing site: Implications for the degradation history of Homestead hollow (expanded abstract). In *50th Abstract Lunar and Planetary Science*. Lunar and Planetary Institute. Abstract #2162.